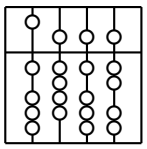

Institut für Informatik
der Technischen Universität München

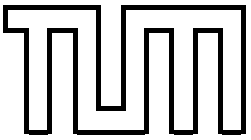

Fiducial-Less Compensation of Breathing Motion in Extracranial Radiosurgery

Dissertation

Kajetan Berlinger

Institut für Informatik
der Technischen Universität München

Fiducial-Less Compensation of Breathing Motion in Extracranial Radiosurgery

Kajetan Berlinger

Vollständiger Abdruck der von der Fakultät für Informatik der Technischen Universität München zur Erlangung des akademischen Grades eines

Doktors der Naturwissenschaften (Dr. rer. nat.)

genehmigten Dissertation.

Vorsitzender: Univ.-Prof. Nassir Navab, Ph.D.

Prüfer der Dissertation:

1. Univ.-Prof. Dr. Bernd Radig
2. Univ.-Prof. Dr. Achim Schweikard, Universität zu Lübeck

Die Dissertation wurde am 26.01.2006 bei der Technischen Universität München eingereicht und durch die Fakultät für Informatik am 28.06.2006 angenommen.

Abstract

Tumors located in the chest and abdomen are often treated by using percutaneous radiation therapy. When radiosurgical methods are applied to these tumors, it is necessary to take into account respiratory motion, which may cause the tumor to shift its position by 1 cm or more. Without compensation of this motion, it is unavoidable to enlarge the target volume by a safety margin. Thus, healthy tissue is also affected by radiation and therefore lower doses must be used to spare healthy tissue.

This thesis describes a new concept, enabling a prediction of the position of the tumor at a certain time without using fiducial markers. The implantation of these markers means an encumbering operation for the patient and the medical staff. By matching periodically taken X-ray images to a computed volumetric deformation model, the respiratory state and thus the position of the target can be determined. As this registration cannot be performed in real-time, infrared emitters are attached to the patient's chest and abdomen to report information on the current state of respiration. The information of the sensor is correlated to the target location computed by the comparison between the X-ray image and the model. Thus, a complete correlation model between external and internal motion is acquired, without using any implanted fiducials.

The main focus of this work lies on the process of creating the volumetric deformation model, which is based on corresponding anatomical landmarks selected in two volume scans, one taken during maximal inhalation one taken during maximal exhalation. A method for fully automatic detection of corresponding anatomical landmarks in volume scans taken at the two different respiratory states was developed. Furthermore, new techniques for labeling computed tomography images with respiratory states are introduced, enabling evaluation of the computed models.

The suggested method for computing volumetric deformation models was evaluated on six patient data sets, five concerning the lung and one the liver. Surface distance measurements of the particular segmented organ of the scan to be deformed and the reference scan, as well as visual inspections on corresponding image slices, yielded high accuracy. Moreover, the feasibility of determining the respiratory state by comparison of an X-ray image to the model was successfully demonstrated by using digitally reconstructed radiographs.

Zusammenfassung

Tumore, die sich im Bereich der Brust und des Abdomens befinden, werden häufig mittels der perkutanen Strahlentherapie behandelt. Bei strahlenchirurgischen Eingriffen bezüglich dieser Tumore ist es wichtig, die durch die Atmung entstehende Bewegung zu berücksichtigen, die zu einer Tumorverschieblichkeit von mehr als 1 cm führen kann. Ohne den Ausgleich dieser Bewegung ist es unvermeidbar, das Zielvolumen um eine Sicherheitszone zu vergrößern. Infolgedessen wird auch gesundes Gewebe bestrahlt und so müssen niedrigere Strahlendosen verwendet werden um dieses gesunde Gewebe zu verschonen.

Diese Arbeit beschreibt ein neues Konzept, das eine Vorhersage der Position des Tumors zu jedem beliebigen Zeitpunkt ermöglicht, ohne dabei implantierte künstliche Marker einzusetzen. Die Implantation dieser Marker bedeutet eine belastende Operation für den Patienten und das klinische Personal. Durch den Abgleich von periodisch aufgenommenen Röntgenbildern mit einem berechneten volumetrischen Deformationsmodell, kann der Atemzustand und damit die Zielposition bestimmt werden. Da diese Registrierung nicht in Echtzeit durchgeführt werden kann, werden Infrarot-Emitter an der Brust und am Bauch des Patienten angebracht, um Information über den momentanen Atemzustand zu erhalten. Die Information des Sensors wird zu der Position des Ziels korreliert, die durch den Vergleich zwischen Röntgenbild und Modell errechnet wurde. Folglich erhält man ein Korrelationsmodell zwischen externer und interner Bewegung ohne die Verwendung implantierter Marker.

Der Schwerpunkt dieser Arbeit liegt auf der Erstellung des volumetrischen Deformationsmodells, das auf korrespondierenden anatomischen Landmarken beruht, die in zwei Volumen-Scans selektiert wurden, wobei ein Scan bei maximal inhaliertem und einer bei maximal exhaliertem Atemzustand aufgenommen wurde. Es wurde eine Methode zur vollautomatischen Detektion korrespondierender anatomischer Landmarken in Volumen-Scans von unterschiedlichem Atemzustand entwickelt. Außerdem werden neue Techniken zur Gewinnung von Computertomographie-Bildern mit bekanntem Atemzustand vorgestellt, die eine Evaluierung der berechneten Modelle ermöglichen.

Die vorgeschlagenen Methoden zur Berechnung von volumetrischen Verformungsmodellen wurden anhand von sechs Patientendatensätzen evaluiert, wobei fünf davon die Lunge und einer die Leber betreffen. Sowohl Abstandsmessungen zwischen den Oberflächen der betreffenden segmentierten Organe des zu verformenden und des Referenz-Scans, als auch die optische Kontrolle von korrespondierenden Schichtbildern zeigten die hohe Genauigkeit des Modells. Darüberhinaus wurde die Machbarkeit der Bestimmung des Atemzustandes durch den

Abgleich eines Röntgenbildes mit dem Modell unter Verwendung von digital rekonstruierten Röntgenaufnahmen erfolgreich demonstriert.

Danksagung

Zu allererst möchte ich meinem Doktorvater Prof. Dr. Achim Schweikard dafür danken, dass er mir die Möglichkeit gab, meine Dissertation zu diesem wirklich sehr interessanten Thema zu verfassen. Mein besonderer Dank gilt auch Herrn Professor Dr. Bernd Radig, der mich nach dem Weggang von Prof. Schweikard meine Arbeit an seinem Lehrstuhl fortsetzen ließ.

Bei PD Dr. Otto Sauer von der Klinik für Strahlentherapie der Universität Würzburg möchte ich mich ganz herzlich für die erfolgreiche Zusammenarbeit innerhalb des Schwerpunktprogramms 1124 der Deutschen Forschungsgemeinschaft bedanken. Er war mir eine große Hilfe bei Veröffentlichungen und bei der Gewinnung von Testdaten. Die zahlreichen Diskussionen mit ihm inspirierten mich immer wieder aufs Neue, wobei auch der Spaß selten zu kurz kam.

Ebenso danken möchte ich Dr. Michael Roth, der als Leiter der Forschungsgruppe der Medizinischen Informatik stets ein offenes Ohr für mich hatte. Aus jedem Brainstorming resultierten neue Ideen, die mich in meinem Forschungsvorhaben unterstützten. Nach mittlererweile über zehn gemeinsamen Jahren an der Technischen Universität München, zuerst als Kommilitonen und später als Kollegen am Lehrstuhl IX, gilt natürlich meinem Freund Heiko Gottschling großer Dank. Ich habe stets von seinen exzellenten programmiertechnischen Fähigkeiten profitiert, aber auch sonst stand er mir immer mit Rat und Tat zur Seite. Freek Stulp war mir immer ein sehr guter Kumpel und brachte mir nebenbei die Kniffe des Publizierens bei. Seine sehr guten Englischkenntnisse schliffen so manches meiner Paper. Den Kollegen Ernst Bartels und Jörg Traub möchte ich für Ihre fachliche Unterstützung beim Entwurf meiner Arbeit danken. Generell sei an dieser Stelle ein großes Dankeschön an den gesamten Lehrstuhl IX ausgesprochen. Dank auch an meinen Freund Alexander Wagner für detailgetreue Illustrationen, die besonders auf der Miccai 2004 in St. Malo zum Tragen kamen.

Meiner gesamten Familie möchte ich für den stets sehr großen Zusammenhalt danken, der sich auch bei der Erstellung dieser Arbeit wieder gezeigt hat. Meine Schwester Konstanze, sowie mein Vater, gaben mir Hilfestellung bei medizinischen Aspekten dieser Arbeit. Mein Cousin Daniel und auch meine Tante Sabine verbesserten meine Arbeit in sprachlicher Hinsicht. Zu guter Letzt möchte ich mich herzlich bei meiner Freundin Anne Buten bedanken, die mich in schwierigen Phasen immer wieder aufgebaut und aufgemuntert hat und somit einen sehr großen Anteil am erfolgreichen Abschluss dieser Arbeit hat.

München, Januar 2006

Contents

1 Introduction

The thesis describes a novel approach to fiducial-less compensation of respiratory motion in extracranial radiosurgery. This compensation is achieved by actively tracking the tumor, whereby the beam follows the tumor. Because the tumor is targeted more precisely, healthy tissue is spared, allowing the tumor to be treated with higher doses.

1.1 Motivation

Tumors located in the chest and abdomen are often treated with percutaneous radiation therapy. The tumor is exposed to high-level X-ray radiation by a linear accelerator, aiming at destroying the DNA of the malignant cells and therefore their ability of cell division. The tumor is irradiated through the skin, thus the treatment is completely non-invasive.

(a) Inhalation (b) Exhalation (c) Difference

Figure 1.1: This Figure shows images of the same slice location, but different respiratory state, to emphasize the problem of respiratory motion. In c) the difference between these images is displayed.

To realize an effective treatment, the tumor has to be targeted precisely, which is difficult, because tumors may move due to respiration. In Figure 1.1 the occurring tissue motion is demonstrated by images of two computed tomography scans taken at different respiratory states but same slice location.

This work focuses on treating lung and liver tumors, whose movements are mainly caused by respiratory motion. Shirato et al. [Shirato 04] performed measurements for 21 lung tumors and 20 liver tumors, yielding maximal amplitudes in cranial-caudal direction of 24.6 mm for the lung, and 19.0 mm for the liver, respectively. Studies of Suramo et al. [Suramo 84] in 50 patients yielded mean movements of the liver in cranial-caudal direction of 25 mm under normal breathing, and 55 mm under deep breathing conditions.

So far, this motion has been taken into account by adding a safety margin to the target volume. Thereby, healthy tissue is also affected by radiation and therefore lower doses must be used to spare the healthy tissue. In Figure 1.2, this fact is illustrated.

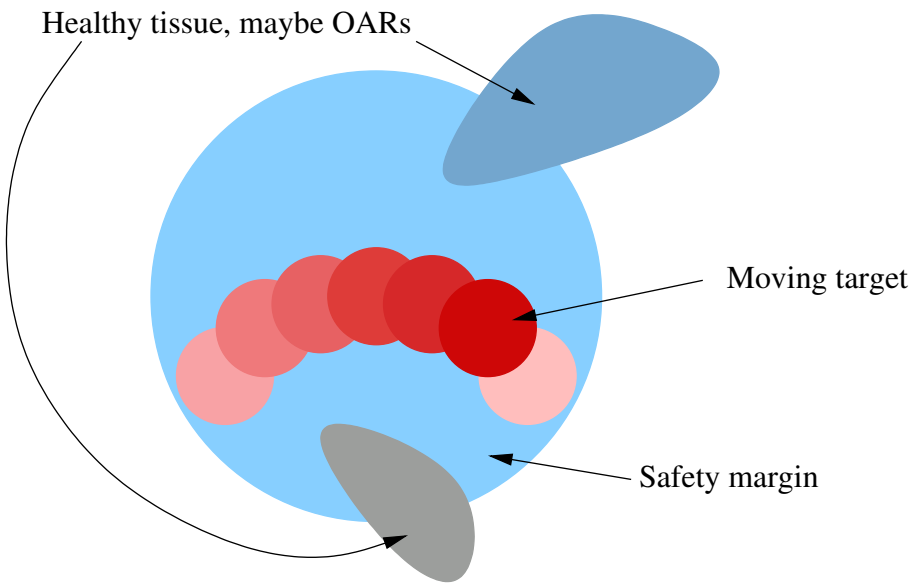

Figure 1.2: This graphic shows the red colored moving target and its surrounding safety margin. The main problem, when enlarging the irradiated volume, is that healthy tissue is also affected. Therefore, lower doses must be used to spare healthy tissue. If the organs are organs at risk (OARs), it will be very difficult to find a way to treat the tumor effectively using this method. Methods for tracking the tumor are needed to find a remedy.

Thus, systems for compensating respiratory motion during radiotherapy treatment are needed. First attempts to reduce respiratory motion made use of patient immobilization techniques, for

example an abdominal press [Wulf 05]. Other approaches are based on irradiating the target during breath-hold [Rosenzweig 00, Wong 99].

The closely related work, described in [Schweikard 00], proposes a method using implanted fiducials to track the tumor. This method has since reached the clinic, and has been integrated into the Cyberknife® Radiosurgical System (Accuray Inc., Sunnyvale, CA). A drawback of this approach is that the implantation of the gold markers entails an operation, which is encumbering for the patient, as well as the medical staff.

Following the line of this research, this thesis aims at creating a method enabling active tumor tracking *without* the use of implanted fiducials. In the next section an overview of the new system is given.

1.2 A Novel System for Active Tumor Tracking

The new system realizing active tracking of the tumor moving due to respiration is based on the computation of a 4D patient model of the affected region of the body. The volumetric deformation model is generated by applying morphing methods to two volume scans performed during inhaled and exhaled breath-hold. The model consists of a number of synthetic scans, each representing a particular respiratory state. Before treatment, X-ray images are taken periodically and are compared to every scan of the model. The best match yields the respiratory state and therefore the position of the tumor. As the target is not visible in the X-ray images, it was marked before in every scan of the model by an expert. Thus, correlation from respiratory state to tumor position is acquired.

Due to a registration time of about 10 seconds for one single 2D-3D registration step, only intermittent information about the target location can be obtained. At the time the comparison of all scans with the current live shot has completed, the target may already have moved. To solve this problem an external sensor is used to report information on the current state of respiration in real-time. This sensor is an infrared tracking system, with emitters attached to significant positions on the patient's chest and abdomen. The information of the sensor is correlated to the target location computed by the comparison between the live shot and the model. Thus, a correlation model between external and internal motion is acquired without any use of internal fiducials, allowing the position of the target to be inferred at any point in time.

(a) Cyberknife® Radiosurgical System

Figure 1.3: The Cyberknife® Radiosurgical System

To actually treat the moving tumor, active tracking is the method of choice. Active tracking means that either the therapeutic beam has to follow the tumor or the treatment table has to position the patient correctly. Figure 1.3 illustrates the Cyberknife® Radiosurgical System with a computer controlled robotic arm allowing 6 degrees of freedom, very well suited for active tracking of the tumor.

1.3 Contributions

The contributions of this thesis compared to state-of-the-art are:

1. **Active tracking of the tumor without using internal fiducials.** The idea of using a computed 4D patient model for inferring the respiratory state by matching radiographs to the model enables fiducial-less compensation of breathing motion in radiosurgery. A very precise treatment of the diseased region can be performed sparing healthy tissue and allowing for higher doses to treat the tumor.

2. **Creating a novel approach for computing volumetric deformation models.** The creation process of the 4D model is landmark-based. The new system provides fully automatic detection of corresponding anatomical landmarks in volume scans taken at different

respiratory states. The resulting control point pairs are used to create the volumetric deformation model for motion compensation in radiotherapy by thin-plate spline interpolation.

3. **Introducing new methods for labeling CT slices with respiratory states.** To evaluate the accuracy of the created 4D models, different methods for labeling CT slices with respiratory states were developed.

4. **Testing the feasibility of a 2D - 4D registration process.** The feasibility of inferring the respiratory state by matching 2D radiographs to computed volumetric deformation models was evaluated.

1.4 Thesis Overview

This thesis is structured as follows:

Chapter 2 introduces some fundamental concepts in medical image processing and radiotherapy, essential for understanding the new system of motion compensation described in this thesis.

Chapter 3 explains tissue motion due to respiration, and the problems this causes in radiation therapy. It is described how conventional systems deal with this problem. Furthermore, an overview of related research is given.

Chapter 4 presents the new system of fiducial-less compensation of breathing motion in extracranial radiosurgery. Its main components, the 4D patient model and the 2D-4D registration process for determining the respiratory state without using internal fiducials are described and evaluated in chapters 6 and 7.

Chapter 5 describes the new approaches of labeling computed tomography scans with respiratory states, needed for evaluating the accuracy of the volumetric deformation models. The methods are described in detail and are compared to existing ones.

Chapter 6 is the main part of this thesis. The focus lies on the creation process of 4D patient models, simulating the deformation of the diseased region due to respiration. A method is described, which enables fully automatic detection of corresponding anatomical landmarks in volume scans taken at different respiratory states. The introduced techniques are evaluated with patient data concerning lung and liver cancer and are compared to related approaches.

Chapter 7 contains a detailed description of the 2D - 4D registration process. Furthermore the method is evaluated on five patient data sets.

Chapter 8 summarizes the work presented in this thesis.

2 Basic Terms in Medical Technology

This chapter describes some fundamentals in the context of radiation therapy and medical image processing, which are essential to understand the main part of the thesis.

2.1 Fundamental Terms in Medicine

In Figure 2.1 fundamental anatomic directions and planes, which are used in this work are specified. See [Platzer 91] for more details.

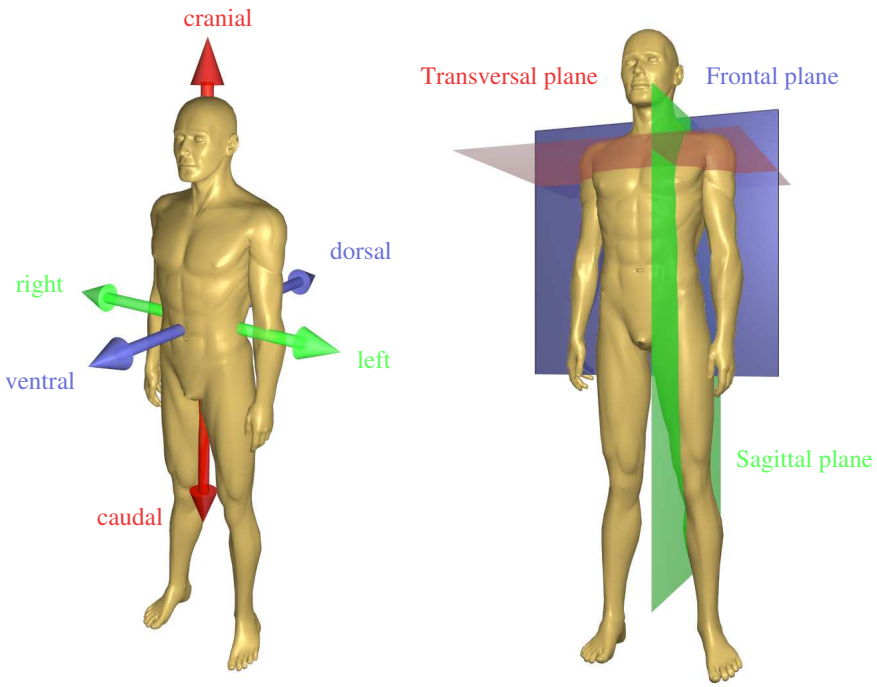

(a) Directions (b) Planes

Figure 2.1: In the left image terms for specifying directions in anatomy are displayed. The image on the right shows the anatomical planes relevant for this work.

2.2 Imaging Techniques

Computed tomography and magnetic resonance imaging both represent medical imaging methods for generating a three-dimensional image of the internals of an object. They are introduced in the next two sections.

2.2.1 Computed Tomography

Computed tomography (CT) is the computerized generation of a three dimensional image by interpreting several radiographs of an object taken from different directions. A volume scan consists of several transversal slices. The patient is positioned on a table, which moves through the gantry, whose apperature contains the imaging device (Figure 2.2).

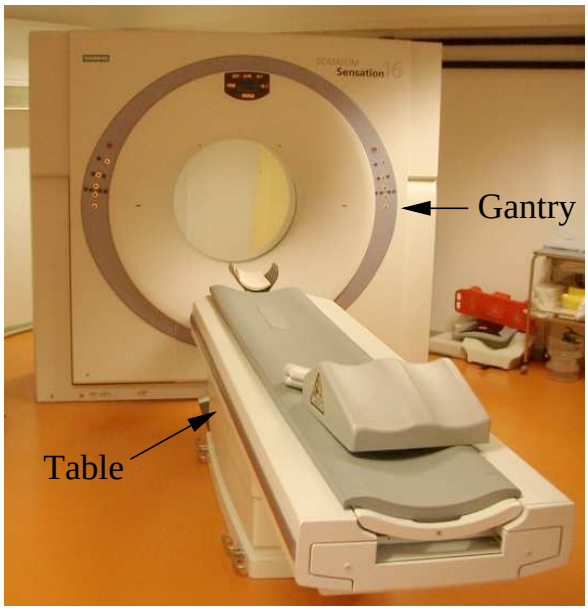

Figure 2.2: The CT scanner SOMATOM Sensation 16 (Siemens AG, Medical Solutions, Erlangen, Germany).

At each table position, the X-ray source and the opposing detectors rotate around the longitudinal axis of the patient's body to measure the attenuations of radiation, caused by the different tissue types the rays have passed. Thus, several transversal images, displaying the internal information of the specific region of the body, are obtained. The attenuation coefficients of the different tissue types are defined as Hounsfield[1] Units. The Hounsfield spectrum ranges from

[1] Sir Godfrey Newbold Hounsfield 1919-2004: English electrical engineering technician

-1000 to 3000, with -1000 representing the attenuation coefficient of air and 0 the attenuation coefficient of water. To emphasize geometrical structures of regions of interest, windowing techniques are applied to the obtained 12 bit images. A window is defined by center and width values. Density values above the defined window are displayed white, values below black. Thus, small density differences can be displayed with more contrast, enhancing image interpretation. For further information about computed tomography refer to [Sauer 98, Wegener 96].

Digitally Reconstructed Radiographs (DRRs)

Digitally reconstructed radiographs are synthetic X-ray images, which are generated from a CT volume scan. By the use of volume rendering techniques, e.g. ray casting, and the knowledge about the camera geometry of the fluoroscopic unit to be simulated, the images are computed. With respect to the domain of medical image registration, DRRs are used for example to enable 2D-3D matching techniques. By numerical optimization of a similarity measure between DRRs of the volume to be registered and the real X-ray, the best match is obtained [Roth 04].

2.2.2 Magnetic Resonance Imaging

Magnetic resonance imaging (MRI) uses the relaxation properties of excited hydrogen dipoles for image generation. Protons spin around their axes and therefore act as a magnet. By the use of a strong magnetic field some protons are adjusted parallel and a majority antiparallel, yielding a magnetization vector.

Figure 2.3: The MR scanner MAGNETOM Avanto (Siemens AG, Medical Solutions, Erlangen, Germany).

The object is exposed to a radiofrequency pulse perpendicular to this vector, causing resonance of the protons having the same frequency as the applied pulse. After this excitation the protons relax and return to their position aligned to the strong magnetic field. During this relaxation process, the protons emit radiofrequency pulses, which are measured by detector coils. The characteristics of this relaxation process strongly depends on various tissue parameters, enabling the calculation of the final image. Magnetic resonance imaging is well suited for soft tissue diagnosis and has the advantage that, in contrast to CT, the patient is not exposed to any ionizing radiation. In Figure 2.3 an example of a magnetic resonance imaging device is displayed. For more details refer to [Sauer 98].

2.3 Image Registration

This section gives a short overview of image registration, for more details see [Maintz 98, Pluim 03, Wein 03, Ibáñez 03]. To register two images means to determine the spatial transform that maps points on one image to corresponding points on the second image. An image registration procedure (Figure 2.4) in general consists of the following components: the two input images, a transformation, a similarity measure and an optimizer.

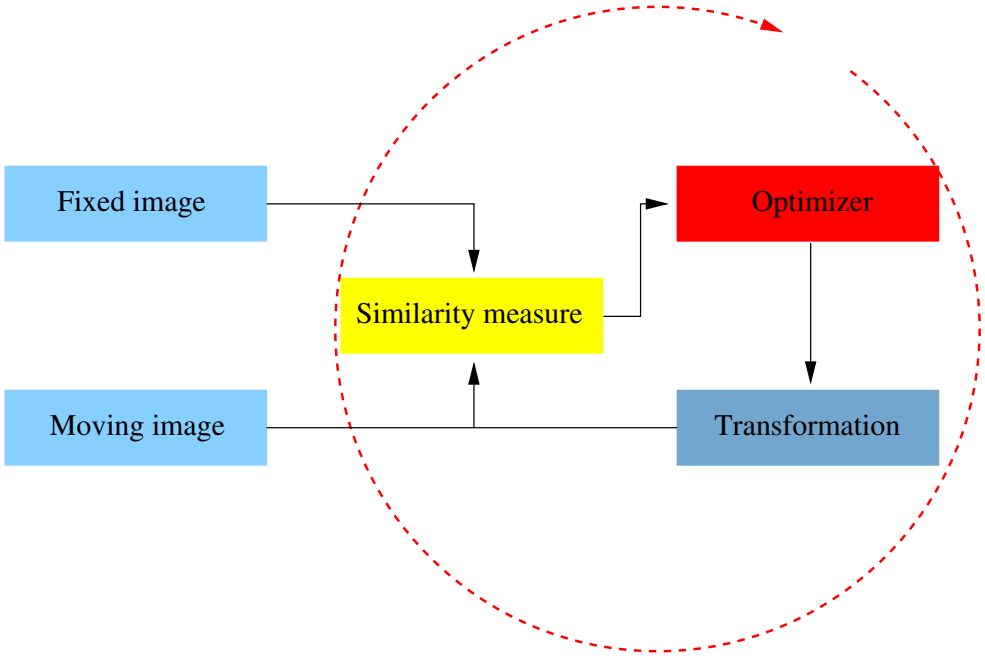

Figure 2.4: An overview of the interacting registration components.

The image to which the transformation is applied, is called the moving image. The other one is

the fixed image. In each iteration the optimizer receives the two images as input, computes their similarity and tries to determine the shortest path to the best match through parameter space. The dimension of the parameter space depends on the degrees of freedom of the underlying transformation.

Important criteria to classify a registration are:

Dimensionality: 2D-3D registration, e.g. for matching an X-ray image with a CT volume scan, or 3D-3D to register two volumes.

Nature of transformation: Is the transformation for example rigid or elastic? Rigid is equivalent to six degrees of freedom, the object can be rotated and translated, whereas elastic implies having a translational vector for every single pixel/voxel.

Domain of transformation: Does the registration affect the complete images (global) or only a certain region (local)?

Involved modalities: A monomodal registration would be for example matching two CT volume scans to each other, whereas matching a MR scan to a CT scan would be multimodal, as the imaging principle is different here.

In the next two sections, examples of an optimizer and two similarity measures, used in the context of this work, are presented.

2.3.1 Gradient Descent Optimizer

When using gradient descent as optimizer, the function evaluation is advanced in the direction of the gradient. By a constant called the ”learning rate” the step size is regulated. Furthermore, the sign of the learning rate determines whether a maximum or a minimum should be found. If the learning rate is negative a minimization is performed, otherwise a maximization results. For further information about optimization see [Press 92].

2.3.2 Similarity Measures

In the next sections two different similarity measures, frequently used in medical image registration, are introduced.

2.3.2.1 Correlation Coefficient

Correlation coefficient represents a similarity measure, which is well suited for monomodal but not for multimodal registration, because it is based on image intensities, as can be seen in the following formula:

$$CC = \frac{1}{\sigma_1 \sigma_2} \frac{1}{n} \sum_{x,y \in T} (I_1(x,y) - \bar{I_1})(I_2(x,y) - \bar{I_2}) \tag{2.1}$$

$\bar{I_1}$ and $\bar{I_2}$ represent the mean intensities, σ_1 and σ_2 the corresponding standard deviations and T the area of intersection of the two images.

2.3.2.2 Mutual Information

Mutual information originates from information theory. The basic idea is to use the distribution of the gray values for measurement and not the gray values themselves. Therefore, this similarity measure is well suited for multimodal registration.

$$MI = H(I_1) + H(I_2) - H(I_1, I_2) \tag{2.2}$$

$H(I_1)$ and $H(I_2)$ represent the Shannon entropy [Shannon 48] for each image:

$$H = -\sum_i p_i \log p_i \tag{2.3}$$

p_i means the probability of the occurrence of a specific intensity i. An image, which consists only of a small amount of different intensities will have a low entropy, whereas an image consisting of many uniformly distributed intensities will have a high entropy, and thus contains a lot of information.

$H(I_1, I_2)$ is the combined information, the joint entropy, of the two images:

$$H(I_1, I_2) = -\sum_{i,j} p_{i,j} \log p_{i,j} \tag{2.4}$$

$p_{i,j}$ is the probability that intensity i occurs in the first image at the same position as intensity j occurs in the second image. For further information about mutual information please refer to [Pluim 03].

2.4 Percutaneous Radiation Therapy Systems

When treating cancer by percutaneous radiation therapy, the tumor is exposed to high-energy X-ray radiation by a linear accelerator. This usually destroys the DNA of the malignant cells and thereby their ability of cell division. To avoid affecting healthy tissue, the treatment has to be planed in detail by the use of imaging systems (section 2.2), e.g. computed tomography and magnetic resonance imaging.

In Figure 2.5(a), a conventional linear accelerator, used for percutaneous radiation therapy, is visualized.

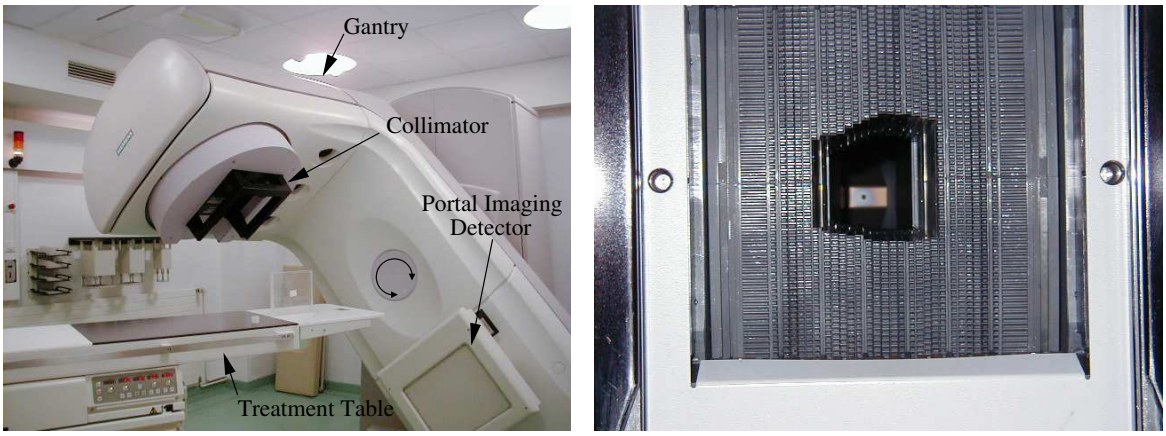

(a) Linear accelerator (b) Multi-leaf collimator

Figure 2.5: The left image shows the linear accelerator Primus (Siemens AG, Medical Solutions, Erlangen, Germany) with the portal imaging detector in hinged position. On the right a multi-leaf collimator is displayed. The leafs can be moved relative to each other to approximate the shape of the target.

By rotating the gantry, containing the beam source, around the axis marked in Figure 2.5(a), radiation can be applied to the tumor from several directions. The single beams are of low dose and sum up in their intersection, called the isocenter. Thus, surrounding tissue is effectively spared and the target receives the dose, needed to destroy its cells with high probability. By using a multi-leaf collimator, as displayed in 2.5(b), each beam can be adapted to the shape of the target, i.e. the tumor.

To ensure a correct adjustment of the patient on the treatment couch with respect to the planning data, the therapeutic X-ray beam is used for imaging. This technique is called mega-voltage

portal imaging (see Figure 2.5(a)), because of the high energetic therapeutic beam used to create the image. Some systems provide integrated kilo-voltage portal imaging, i.e. an additional X-ray source of lower energy is used to obtain images with much better contrast.

In Figure 2.6 the Cyberknife® Radiosurgical System (Accuray Inc., Sunnyvale, CA) is displayed. The stereotactic radiosurgery system is characterized by a computer controlled robotic arm allowing 6 degrees of freedom. This yields increased flexibility for positioning the beam source, resulting in more effective sparing of critical structures compared to conventional systems. The system has an integrated stereo X-ray imaging device[2], suited for an automatic positioning of the patient.

For further information on radiation therapy see [Richter 98, Hilbig 03].

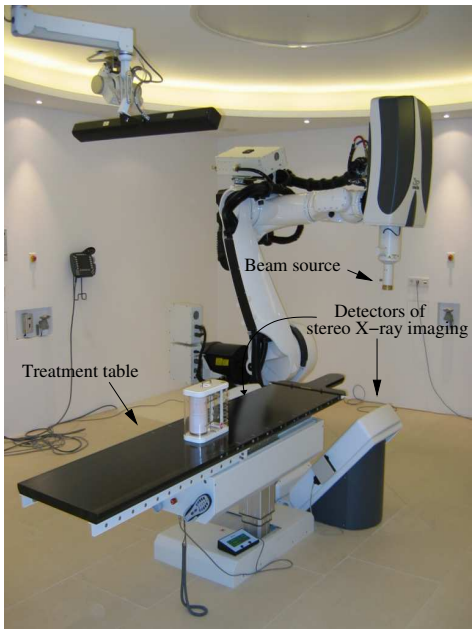

Figure 2.6: The Cyberknife® Radiosurgical System (Accuray Inc., Sunnyvale, CA).

2.5 Résumé

In this chapter some fundamental terms and methods in medical image processing and radiation therapy were introduced, necessary for the description of the novel system of tracking tumors moving due to respiration, which is presented in the following chapters.

[2] Two X-ray sources with nearly orthogonal visual axes.

3 Respiratory Motion in Radiotherapy

Percutaneous radiation therapy represents an important option in treating solid tumors. This technique is non-invasive as the radiation is performed through the skin. The more precisely the tumor can be targeted, the more effective the treatment. Healthy tissue is spared and higher doses can be used to treat the tumor. Thus, when applying radiosurgical methods to tumors located in the chest and abdomen, the movements of the target, the diseased organ and its neighboring organs have to be taken into account. These movements are caused by:

1. The patient's respiration,
2. the beating heart
3. and the peristaltic movement of visceral organs.

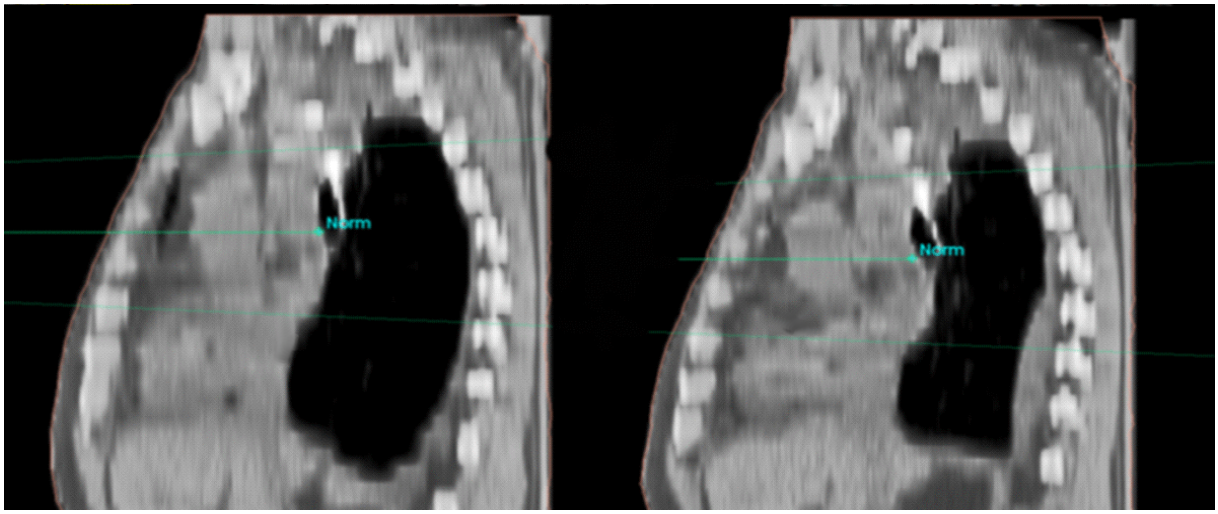

Figure 3.1: DRRs in the sagittal plane demonstrating the change in size and shape of the lung during respiration. The image on the left shows the inhaled and the image on the right the exhaled lung.

During inhalation, the ribcage rises through the contraction of the musculi intercostales externi. The ribcage extends in cranial-caudal, ventral-dorsal and left-right direction. Simultaneously,

the diaphragm contracts thus causing an extension of the lung. With respect to exhalation, the ribcage is lowered by the contraction of the musculi intercostales interni. The diaphragm relaxes and therefore moves cranially into the thorax. As the liver is connected to the diaphragm at the area nuda, it moves up and down along with respiratory motion. Figures 3.2 and 3.1 illustrate the movements due to breathing. For further information about respiration refer to [Platzer 91].

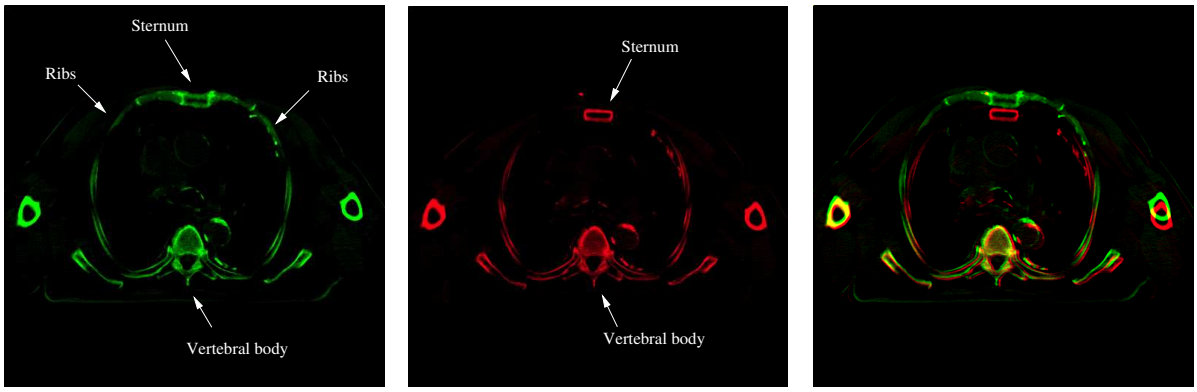

(a) Inhalation (b) Exhalation (c) Addition

Figure 3.2: Image a) and b) show CT images taken at the same slice location, but different respiratory state. The addition of the two images is displayed in c), demonstrating the extension of the ribcage. The vertebral body did not move, but the sternum moved cranial-ventrally.

This work focuses especially on treating lung and liver tumors, the movements of which are mainly caused by respiratory motion. Measurements by Shirato et al. [Shirato 04], performed for 21 lung tumors, yielded mean amplitudes in tidal breathing of 1.0 mm in left-right, 2.8 mm in cranial-caudal and 1.5 mm in anterior-posterior direction. For 20 liver tumors examined, the results were 4.0 mm in left-right, 9.0 mm in cranial-caudal and 5.0 mm in anterior-posterior direction. Maximal amplitudes in the cranial-caudal direction were 24.6 mm for the lung and 19.0 mm for the liver. In Figure 3.1 the deformation of the lung due to respiration is illustrated.

To ensure that the tumor, in spite of these movements, is constantly irradiated, a safety margin is added to the target volume in current practice. The size of this safety margin is determined by observing the motion of the tumor with an appropriate imaging device, for instance X-ray imaging. The big drawback of this method is that healthy tissue is also affected and therefore lower doses must be used to treat the tumor, as demonstrated in Figure 3.3.

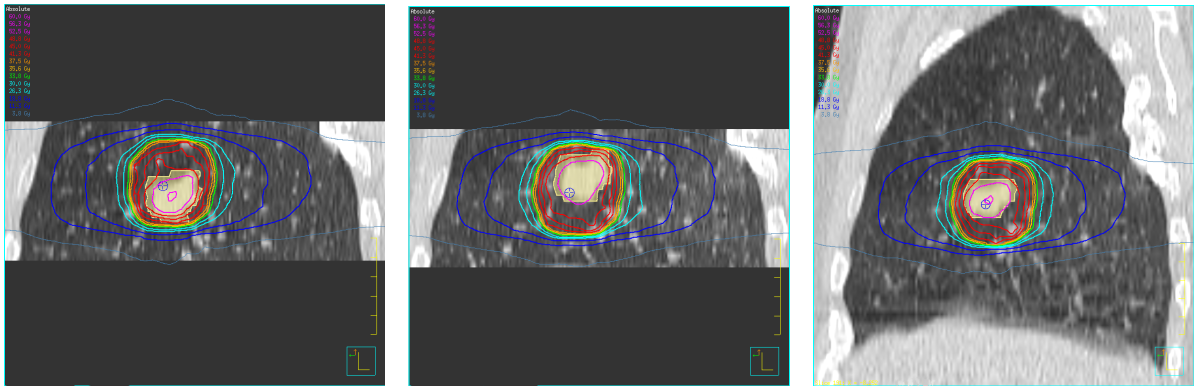

(a) Inhalation (b) Exhalation (c) Normal-breathing

Figure 3.3: These dose distributions of one particular treatment plan demonstrate the problem of moving tumors (pink means highest, blue lowest dose). The target volume had to be enlarged by a safety margin, to ensure that the tumor is irradiated at any point of time.

Thus, the need for a 4D dose distribution[1] arises, which considers the different movements of the target and its surrounding organs at risk due to respiration. A lot of progress has been made in gaining 4D image data (see chapter 5) avoiding blurred images, which are not suitable for the segmentation of regions of interest.

Figure 3.4: An abdominal press to minimize respiratory motion.

[1]The dose distribution represents the variation of applied radiation dose within different regions of the patient's body.

Furthermore, knowledge about the different kinds of motions occurring due to respiration has increased in recent years [Goitein 04] and therefore many approaches have been proposed to spare healthy tissue, to enable more specific radiation of the tumor. Simple solutions for limiting motions like patient immobilization, for instance using the BodyFIX® RT[2] system (Medical Intelligence, Schwabmünchen, Germany, see Figure 3.8) or using an abdominal press [Wulf 05] (see Figure 3.4), have been established. More complex systems are described in section 3.1.

3.1 Related Work

There are three different methods for solving the problem of treating tumors, moving due to respiration: irradiation during breath-hold, gating techniques and active tracking of the target. In the next sections, different approaches realizing these methods are described. They are commented at the end of the chapter in the résumé.

3.1.1 Irradiation During Breath-Hold

This most obvious method requires that the respiration of the patient is suspended during irradiation. The patient has to perform a breath-hold. Some methods to help the patient holding his breath are presented.

3.1.1.1 Deep Inspiration Breath-Hold [Rosenzweig 00]

The approach of Rosenzweig et al. addresses the problem of tumor motion through a combination of three-dimensional radiation therapy and the deep inspiration breath-hold (DIBH) technique. DIBH represents a technique for spirometer-controlled breathing, in which the patient has to hold his breath during treatment. Therefore, the patient has to be trained by verbal commands in order to achieve nearly 100% vital capacity during breath-hold. After initial free breathing, he has to perform a slow deep inspiration, followed by a slow deep expiration, then again a slow deep inspiration and finally the breath-hold. This method has two major advantages: respiratory motion is mostly reduced by the breath-hold and by the increase of the volume of the lung, healthy tissue is spared during irradiation. Tests with seven patients led to significantly higher doses received by the target without additional toxicity.

[2] BodyFIX® RT is a system that immobilizes the patient by vacuum technology enabling an accurate positioning and minimizing of the respiratory motion

3.1.1.2 Active Breathing Control [Wong 99]

Active Breathing Control is a forced breath-hold technique, which reduces breathing motion during radiation by controlling the airflow of the patient's respiration. This method is described in detail in section 5.2.2.1. The Active Breath Coordinator™ from Elekta (Stockholm, Sweden) is another tool for performing active breath-hold. The patient breathes through a mouthpiece, which is connected to the portable system. The lung volume is measured and displayed on a monitor. If the pre-specified breathing volume is reached, a valve blocks airflow for a predefined time span. The breath-hold can be repeated, yielding the same volumes each time. Irradiation is performed during breath-hold, allowing smaller safety margins for targets in the chest and abdomen due to a significant reduction of the tumor's movement. Patients familiarize themselves with the portable device in advance to guarantee a trouble-free treatment. The patient is informed about the remaining time of the breath-hold. By a thumb switch he can stop breath-hold anytime. Most patients tolerate durations of breath-hold of 10 to 30 seconds, thus enabling longer irradiation intervals and therefore faster treatments compared to using gating techniques.

3.1.2 Gating Techniques

An internal or external sensor is needed to get information about the current state of respiration. Gating means that the beam is switched off each time the target moves out of a predefined window of a particular sensor's data (Figure 3.5).

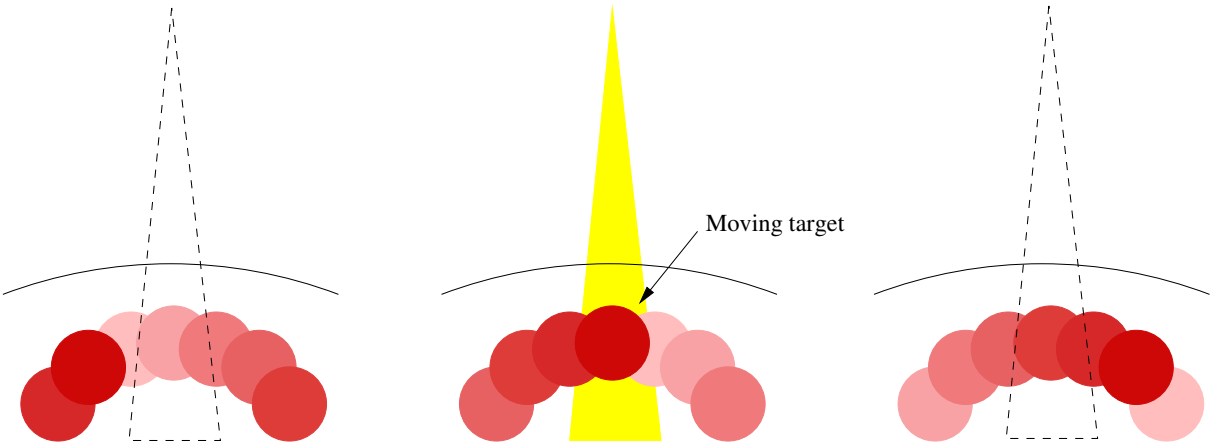

Figure 3.5: Every time the target moves out of the predefined window, the beam is turned off.

A first attempt within this work to realize motion compensation during radiotherapy, was based on gating. An infrared optical tracking system was used to follow emitters attached to the pa-

tient's chest. Whenever the respiratory curve exceeded a user-defined threshold, the therapy beam was switched on. In Figure 3.6 a screenshot of the application can be seen.

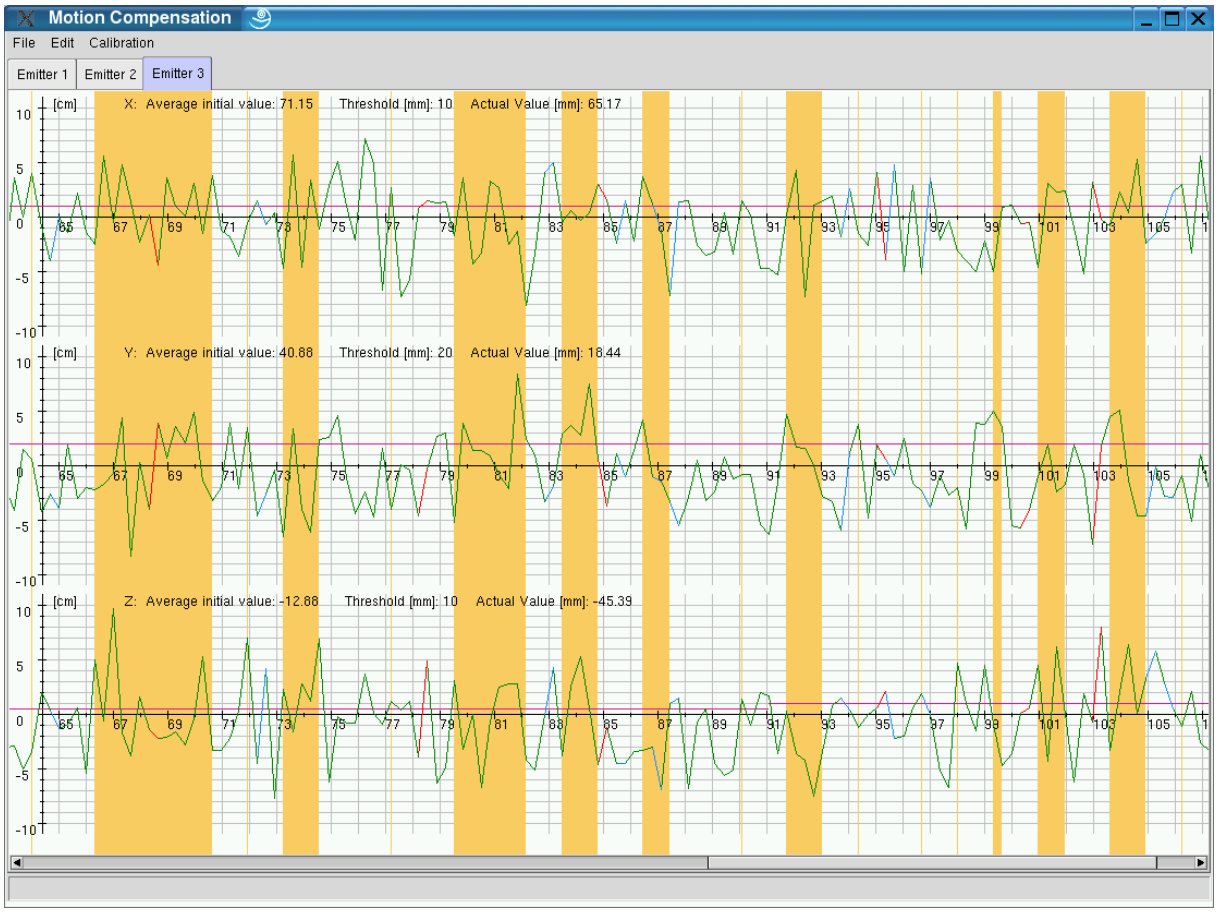

Figure 3.6: The application window shows the respiratory curves for each emitter. Thresholds for triggering the linear accelerator can be defined, visualized by the violet horizontal lines. A red curve symbolizes error in data, blue means that data was weak. The orange areas mean that the beam was activated. This graph shows test data only.

3.1.2.1 Gating by Using a CCD Camera [Johnson 98]

Johnson et al. use a B&W CCD camera as external sensor. The camera is mounted near the right lateral laser[3] and observes the moving chest of the patient. Prior to treatment one single spiral CT scan is taken during breath-hold. By using the camera's calibration parameters and volume rendering techniques, an image of the body surface of the patient's chest, with the same viewing perspective as that of the camera, is rendered based on the CT data. During treatment, the current position of the anterior chest wall in every single image of the live video is compared

[3]The wall-mounted lasers are needed to position the patient in the treatment room.

to that in the rendered image. Every time the deviation exceeds a predefined threshold, the beam of the linear accelerator is turned on. To accelerate the image processing rate, the region to be analyzed is limited by the user.

3.1.2.2 Gating by Using Capnograph and Pneumotachometer [Sontag 98]

Sontag et al. simultaneously analyze the amount of exhaled carbon dioxide, airflow, air pressure and lung volume for determining the current state of respiration. CO_2 is measured by using a capnograph[4]. The values of airflow, air pressure and lung volume are gained by a pneumotachometer. Readings are updated 100 times per second, thus allowing the radiation therapy system to be triggered at appropriate thresholds.

The obvious disadvantage of using gating techniques is the fact that overall treatment times increase because of the very small intervals of irradiation.

3.1.3 Active Tracking of the Target

Active tracking of the tumor means that the therapeutic beam is never switched off, and the radiosurgical system ensures that the tumor volume is always located inside the target volume, while the patient breathes freely, as illustrated in Figure 3.7.

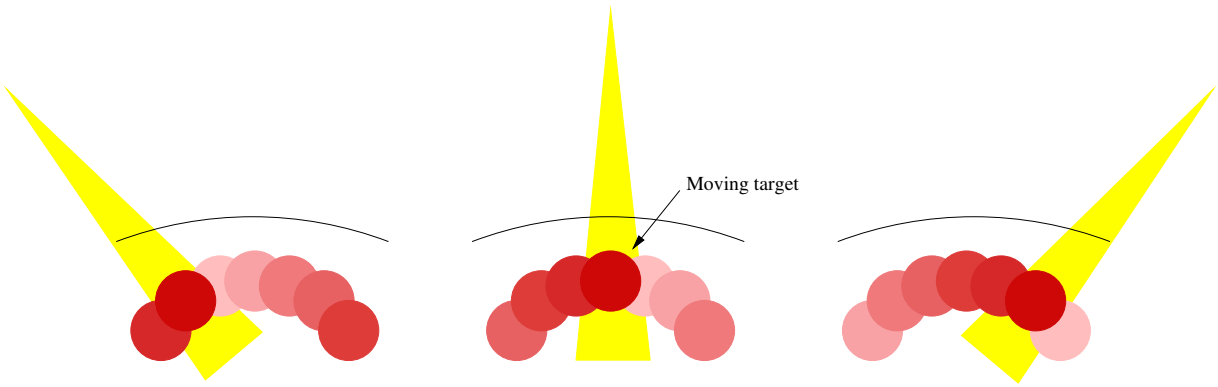

Figure 3.7: With active tracking, the beam either follows the target, as demonstrated in this drawing, or the treatment table moves (Figure 3.8) to correctly align the target with the therapeutic beam.

The position of the tumor has to be determined in real-time, and either the therapy beam has to

[4] A system that monitors the concentration of exhaled carbon dioxide. By using a tube the exhaled gases are brought to the analyzing device.

follow the tumor or the patient has to be repositioned dynamically. Examples of devices aligning the patient are the Cyberknife® (Figure 3.10) system, a stereotactic radiosurgery system with a computer controlled robotic arm allowing 6 degrees of freedom, and the HexaPOD™ treatment couch, a system that repositions the patient dynamically to actually track the target (Figure 3.8). Different approaches for real-time tracking of tumors are compared in the following sections.

Figure 3.8: The HexaPOD™ treatment couch (Medical Intelligence, Schwabmünchen, Germany), a fully robotic patient positioning platform to correct for all misalignments, with an integrated BodyFIX® to fixate the patient on the moving table and therefore avoid additional movements. Positive side effect of the fixation: it immobilizes the patient and therefore limits respiratory motion.

3.1.3.1 Implanted Fiducials and Stereo X-Ray Imaging [Schweikard 00]

This previous work by Schweikard et al. serves as the basis for this thesis. The basic idea is to generate a correlation model between external and internal motion. To detect the internal motion, prior to treatment gold markers are attached to the target region. The spatial position of these fiducials is recorded by stereo X-ray imaging[5], using automated image analysis techniques. The registration procedure of determining the precise marker locations takes 10 seconds, thus the breathing motion cannot be followed accurately. Therefore, optical tracking of emitters, attached to significant locations of the patient's chest and abdomen, is used and synchronized with the X-ray imaging (see Figure 3.9). Updated positions are obtained 60 times per second from the tracking system.

Thus, prior to treatment, a correlation model between internal and external motion is computed. During treatment the correlation model is used as follows:

[5]Two X-ray sources with nearly orthogonal visual axes.

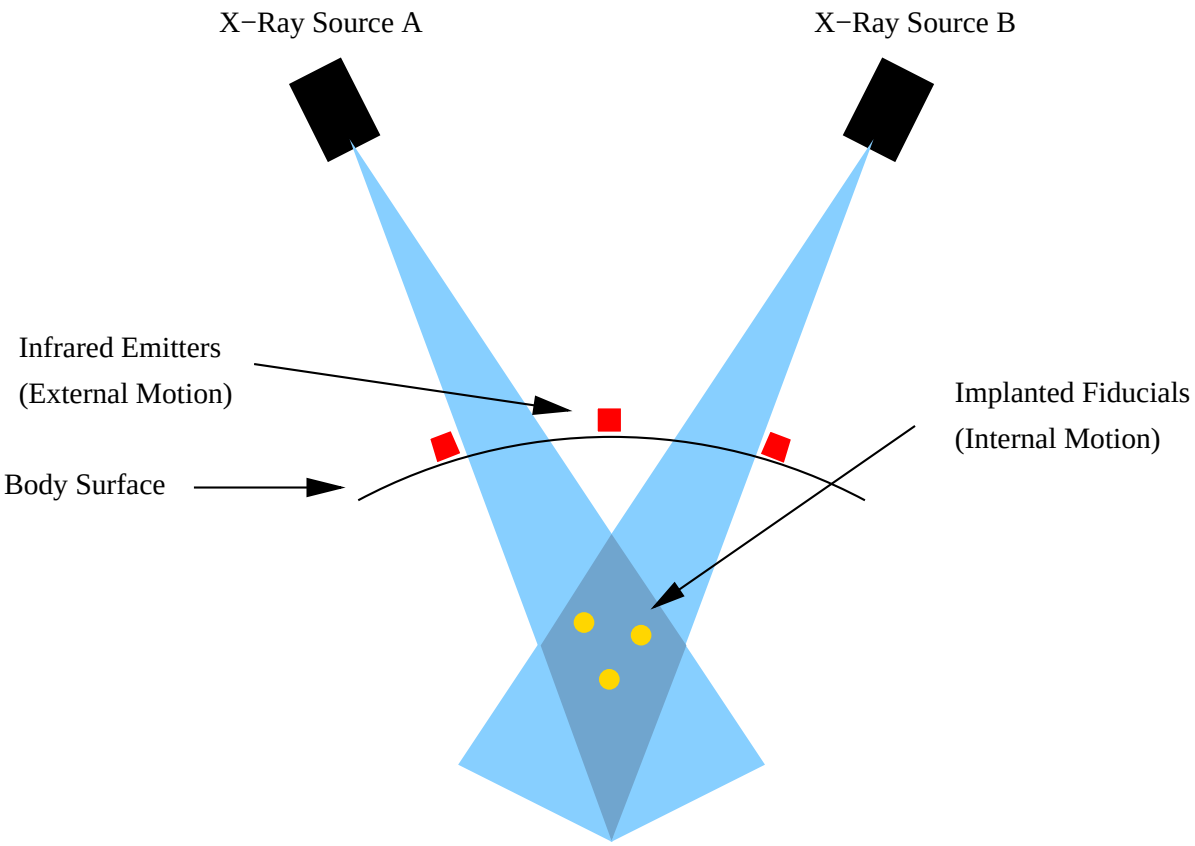

Figure 3.9: The positions of the internal gold markers are detected by stereo X-ray imaging and are correlated to the center of mass of the infrared emitters, which are attached to the chest/belly of the patient.

1. The current external sensor position is read.
2. The center of mass of the external markers is calculated.
3. The closest point on the curve for the external motion can be determined.
4. This point determines the corresponding points on the curves for the internal markers through linear interpolation.

There is also the possibility of updating the correlation model during treatment, by taking more pairs of X-ray images. Thus, systematic drift of the position of the patient and small changes in the respiratory curve can be compensated for.

This method has since reached the clinic, and has been integrated into the Cyberknife® Radiosurgical System (Accuray Inc., Sunnyvale, CA), a stereotactic radiosurgery system with a computer controlled robotic arm allowing 6 degrees of freedom. The Cyberknife® system (Figure 3.10) enables active tracking and thus there are no dead times when irradiating. The beam is permanently activated.

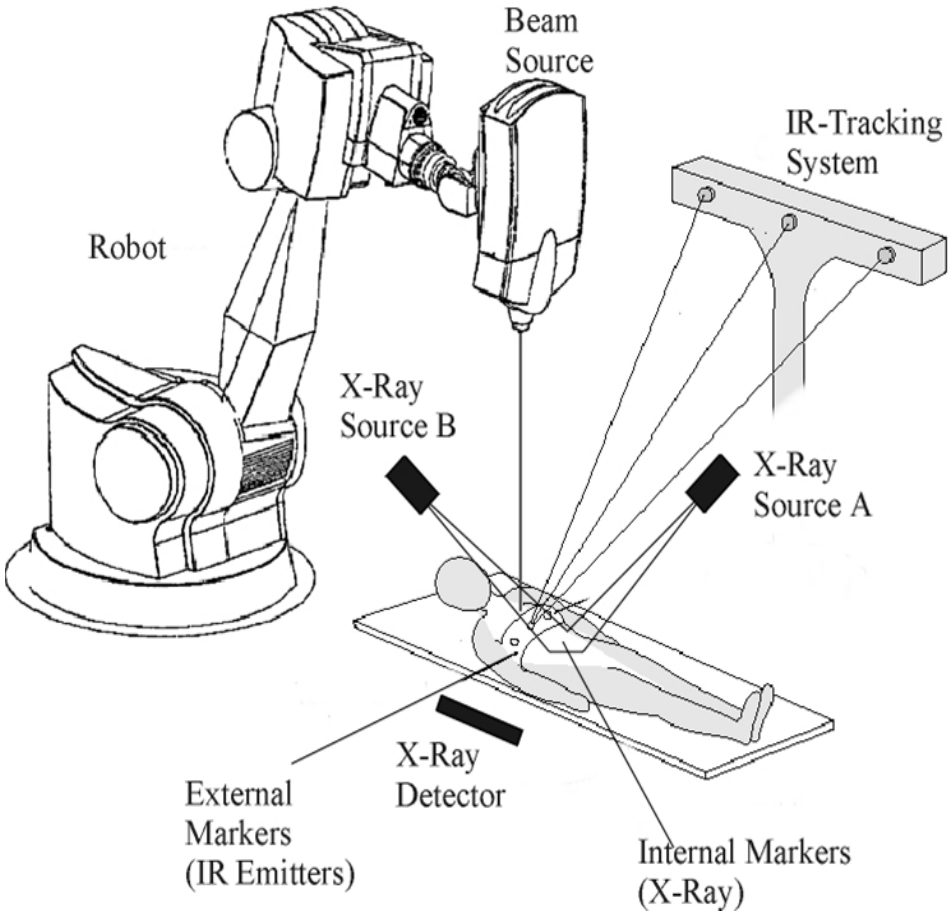

Figure 3.10: The setup of the Cyberknife® Radiosurgical System with stereo X-ray imaging to detect the gold markers implanted near the target, and the optical tracking system to watch the movements of the emitters attached to the patient's chest.

3.1.3.2 Ultrasound with Force Torque Sensor [Riesner 03]

This closely related approach is also based on generating a correlation between external and internal motion, but here ultrasound imaging is used to detect the internal motion of the target. The head of the ultrasound system is mounted on a force torque sensor, which in turn is mounted on a robotic arm. The force torque sensor is needed firstly for the telemedical positioning of the ultrasound device and secondly for acquiring information about the external motion, by measuring the different pressures on the ultrasound head, caused by respiration. The drawback of this approach lies in the nature of ultrasound imaging, its noisy imprecise images, in which the target is not easy to detect.

3.1.3.3 Megavoltage Portal Imaging [Baier 05a, Baier 05b, Meyer 05]

It's obvious to think of using megavoltage electronic portal imaging for tracking the tumor, because of the fact that most radiation therapy systems provide this imaging technique. However, the quality of the resulting images is very poor due to using the high energetic therapy beam for imaging. Thus, compared to conventional X-ray diagnostics, the absorption differences are very small, yielding images with low contrast and poor in detail. Another drawback is the larger focus spot of the linear accelerator resulting in increased geometrical blurring. For more details please refer to [Richter 98].

Nevertheless, a lot of research is done in the field of tracking tumors by using electronic portal imaging. Baier et al. achieved an acquisition rate of 15 images per second on a TV camera-based portal imaging system (Siemens Beamview Plus™). For tracking, a mask surrounding the target is manually positioned on a portal reference image. This mask is matched to each of the following images in order to obtain the trajectory of the moving object. They tested several similarity measures according to their suitability and robustness for this registration process.

3.1.3.4 Magnetic Trackers Near The Target [Cleary 02, Tang 04]

The work of Cleary et al. represents another approach for acquiring correlation models between external and internal movement. The external motion is also observed by optical tracking, but for detecting the internal organ movement they rely on magnetic trackers, implanted near the target region. The used Aurora®-System (NDI Europe, Radolfzell, Germany) provides very small sensors (0.9 mm in diameter, 8 mm in length) and thus can be embedded in thin needles and catheters. Therefore, the sensors can be placed near the target by a needle or even inside the affected organ by using a catheter. For evaluation, a liver respiratory motion simulator was constructed and some trials with swines were performed.

3.1.4 Résumé

This chapter describes the different approaches handling respiratory motion, when treating tumors in the area of abdomen and chest. They all belong to one of these categories:

- Patient immobilization
- Breath-hold techniques
- Gating techniques

- Active tracking of the target

In this résumé the approaches presented in 3.1 are summarized and commented.

First, there are simple solutions, which try to reduce the movement of the tumor due to breathing by patient immobilization. This immobilization can be achieved for example by using an abdominal press or the BodyFIX® RT system. These methods are easy to use and certainly mean progress in radiation therapy, but surely cannot be the final solution for compensating respiratory motion.

Breath-hold techniques like deep inspiration breath-hold (DIBH) and active breathing control (ABC) are also based on the idea of suspending respiratory motions during irradiation. Advantages of these methods are that by the breath-hold the respiratory motion is reduced and by the increase of the volume of the lung healthy tissue is spared. During breath-hold the lung of the patient is nearly at 100% vital capacity and therefore healthy parts of the lung are excluded from the radiation field. Surely these methods don't provide a lot of comfort to the patient, even if some clinical solutions like the Active Breathing Coordinator™ already tackle this problem. Another drawback is that some patients, especially lung cancer patients, are not able to tolerate the breath-hold maneuvers and thus cannot be treated with these methods.

These patients can be treated using gating techniques [Rosenzweig 00]. The patient can breath freely and the beam is switched off each time the target moves out of a predefined window, defined by an internal or external sensor. The approach using a cagnograph and a pneumotachometer as external sensors for gating may have advantages like the lack of calibration problems or avoiding imaging artifacts, but it also means lack of comfort for the patient. Using a CCD camera for following the motion of the chest and comparing the single images to an image rendered from a CT scan seems not very robust. Breath temperature sensor, strain gauge [Kubo 96] or optical tracking [Schweikard 00] have shown to be appropriate sensors for respiratory gating. A big disadvantage of gating is the increase of treatment time. The duration of a treatment normally rises by factor 2 to 3 when using gating [Sontag 98].

Surely, the shortest treatment times can be achieved by active tracking of the target region. The position of the tumor has to be determined in real-time. Either the therapy beam has to follow the tumor or the misalignments have to be corrected by dynamically repositioning the patient. This can be provided for example by the Cyberknife® (Figure 3.10) system or by the HexaPOD™ treatment couch (Figure 3.8).

Most of the approaches for active tracking try to build up a correlation model between external and internal motion. As external sensors they rely on techniques similar to these of gating, but here additional information from inside the patient's body is needed. Ultrasound imaging

(see section 3.1.3.2) is not suitable for detecting the position of a moving tumor because of its noisy, imprecise images. However, the idea of mounting the ultrasound device on a force torque sensor for acquiring information about the external motion, by measuring the different pressures on the ultrasound head, caused by respiration, is very good. Sternutation or coughing of the patient leads to tension of the abdominal wall, that can easily be detected by the force torque sensor. Thus, the beam can be switched off until the respiratory curve of the patient has stabilized again.

Megavoltage electronic portal imaging may be well suited for registration processes of patient set-up verification as Matsopoulos et al. showed [Matsopoulos 04], but not for getting information about the internal state of the tumor in real-time as Baier et. al try to realize (see section 3.1.3.3). One reason is the very poor image quality offering only low contrast and few details due to using the high energetic therapy beam for creating the image resulting in very small absorption differences. A further drawback is the increased geometrical blurring, caused by the larger focus spot of the linear accelerator.

Cleary et al. used magnetical trackers, inserted into the patient's body by a needle, to report information about the internal state. A possible problem of this approach could be that the inserted object, a needle or a catheter, will affect the freedom of movement of the magnetic tracker and thus won't give precise information about the current position of the target.

This problem vanishes, when implanting fiducials near the tumor and observing the movements by stereo X-ray imaging. The method of Schweikard et al. has since reached the clinic and has been integrated into the Cyberknife® Radiosurgical System.

The remaining drawback is the implantation of the fiducials near the tumor, what means an encumbering operation for the patient and the medical staff. Under CT control the gold markers are injected through a 18 gauge biopsy needle into the vicinity of the target area. In the next chapter a new system for tracking tumors *without* using implanted fiducials is described.

4 A Novel System for Tracking Tumors

This chapter introduces the novel system for fiducial-less compensation of respiratory motion in extracranial radiosurgery. It is is based on the closely related approach of Schweikard et al. [Schweikard 00], in which implanted fiducials, gold markers, were used, to track the tumor. This method has since reached the clinic, and has been integrated into the Cyberknife® Radiosurgical System. A big drawback of using fiducials is the mandatory implantation of the gold markers, which means an encumbering operation for the patient and the medical staff. To avoid the use of fiducials, the idea is to generate a synthetic 4D model of the diseased internal organ of the patient prior to treatment, to be able to determine the state of respiration by matching radiographs to the model. The creation process of this volumetric deformation model represents the main part of this thesis and is described in detail in chapter 6. This chapter gives an overview of the new method of tracking tumors, moving due to respiration, without using implanted fiducials.

4.1 Detecting the Position of the Tumor

First, a synthetic 4D model of the affected internal organ of the patient has to be computed. This is done by using different landmark-based image deformation methods (see chapter 6).

Prior to treatment, two CT volume scans are taken: one scan during inhaled breath-hold, one during exhaled breath-hold. In each scan, the target region is determined by an expert. These scans are used as input for the computation of the model. Immediately before treatment, X-ray images, in which the tumor is not visible, are taken periodically and are compared to the created 4D model. This means a 2D-4D registration procedure [Berlinger 04a] consisting of several 2D-3D registrations as can be seen in Figure 4.1. Details of the 2D-4D registration procedure are presented in chapter 7.

The best match determines the respiratory state and, because of the previously marked position of the target, the tumor position. Thus, a correlation between respiratory state and tumor position is acquired. Because the computing time of the intensity-based registration method [Roth 04]

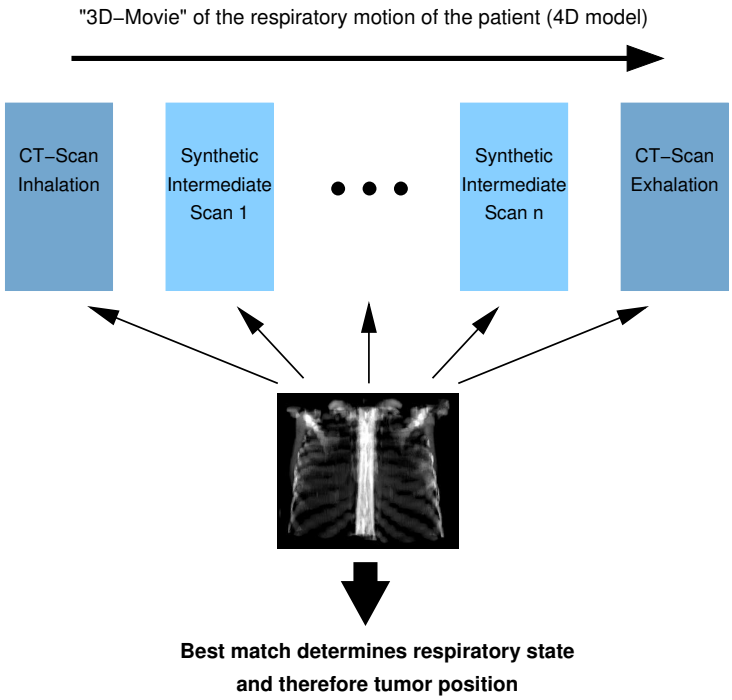

Figure 4.1: The 2D-4D registration step. The actual live X-ray image (actually two from the stereo imaging) is matched to the 4D model of the patient, consisting of a number of synthetic volume scans. The best result yields the respiratory state and therefore the target position (which has been marked before by an expert).

takes about 10 seconds for one single 2D-3D registration step, only intermittent information about the target location is available. At the time the comparison of all scans with the current live shot is completed, the target may already have moved.

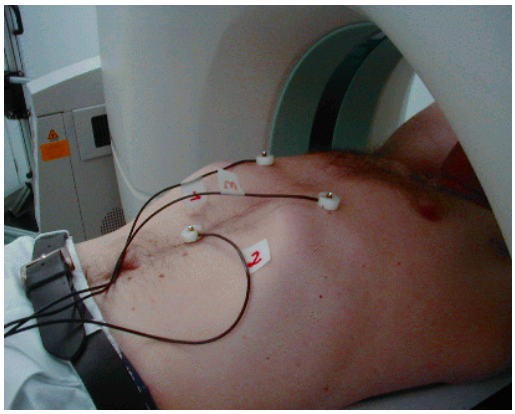

Figure 4.2: The emitters are attached to the patient's chest in order to get a respiratory curve.

To solve this problem an external sensor is used to report information on the current state of respiration in real-time. This sensor is an infrared tracking system, with emitters attached to

significant positions on the patient's chest and abdomen (see Figure 4.2).

Kubo and Hill [Kubo 96] compared various external sensors, like breath temperature sensor, strain gauge or spirometer, with respect to their applicability for respiratory gating. In this application the infrared tracking method is used, because of its high accuracy and speed as well as its stability under radiation exposure.

When a new live image is taken, the system simultaneously records the signal from the tracking system. Therefore, the point of time of every live shot within the respiratory curve of the patient is known and after the 2D-4D registration procedure the position of the target is determined as well. By repeating this synchronization, a complete correlation model between internal and external motion is obtained without any use of internal fiducials. This is illustrated in Figure 4.3.

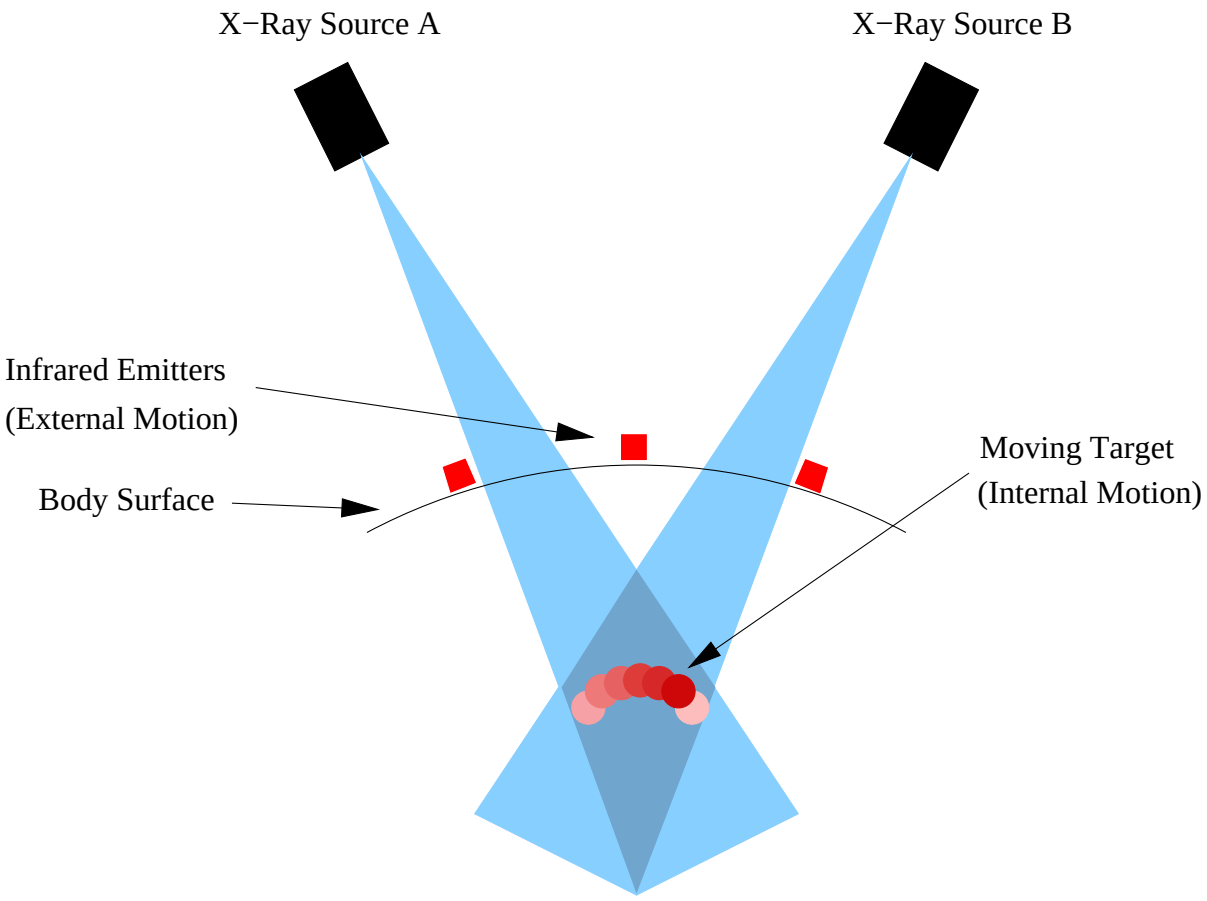

Figure 4.3: The position of the target is determined by stereo X-ray imaging and is correlated to the position of the external markers.

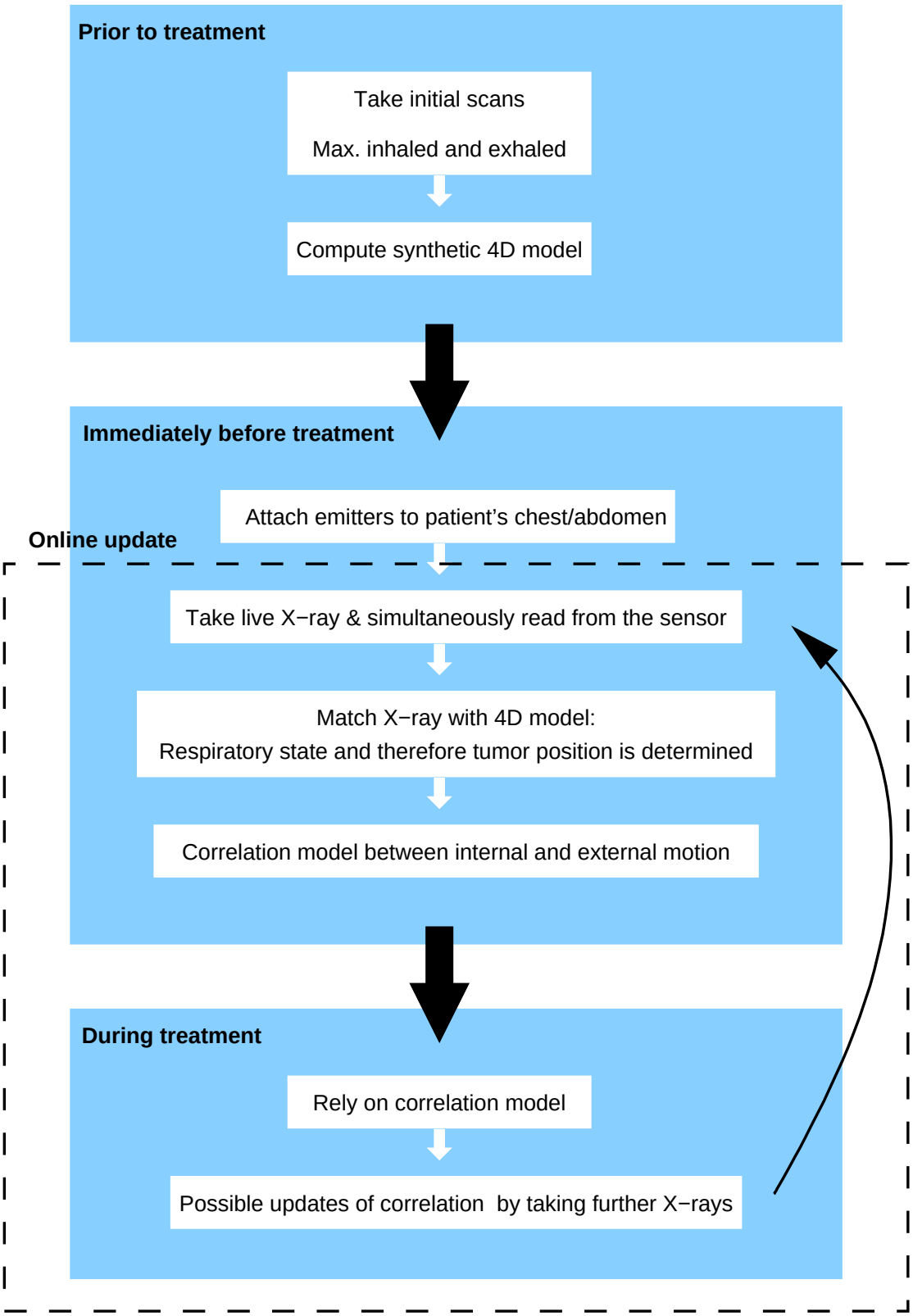

Figure 4.4: The application flow of the new system for *fiducial-less* motion compensation in radiosurgery.

The correlation model enables an accurate determination of the position of the tumor at any given time. During treatment, the system relies on the correlation model created before and therefore can infer the position of the target by the readings of the external sensor. However, the correlation model is continuously updated during treatment. Figure 4.4 gives an overview of the new system for *fiducial-less* motion compensation in radiosurgery.

To actually treat the moving tumor, active tracking is the method of choice. Active tracking means that either the therapeutic beam has to follow the tumor or the misalignments have to be corrected by dynamically repositioning the patient (see section 3.1.3). Different possibilities enabling active tracking of the tumor are discussed in the next section.

4.2 Tracking the Tumor

For actually tracking the tumor, three techniques were considered:

1. Active Tracking:

    a) by the Cyberknife® Radiosurgical System, a stereotactic radiosurgery system with a computer controlled robotic arm allowing 6 degrees of freedom (Figure 4.5(a)).

    b) by the HexaPOD™ treatment couch, a fully robotic patient positioning platform to correct for all misalignments (Figure 4.5(b)).

2. Synchronization by gating, i.e. the beam is switched off each time the target moves out of a predefined window (see section 3.1.2)

First, the focus was set on gating, because of its assumed easy technical feasibility. The linear accelerator just has to be connected to a personal computer by a relay card, but there are two decisive drawbacks: the treatment time will significantly increase and furthermore it has to be ensured that there is enough time for activating a stable therapeutic beam [Schweikard 04a]. Therefore, systems enabling active tracking of the tumor were preferred. Figure 4.5(a) shows the Cyberknife® Radiosurgical System, which obviously is very well suited for the purposes of the described novel method. One could also conceive of a conventional linear accelerator that integrates the HexaPOD™ treatment couch to enable active tracking of the target (see Figure 4.5(b)).

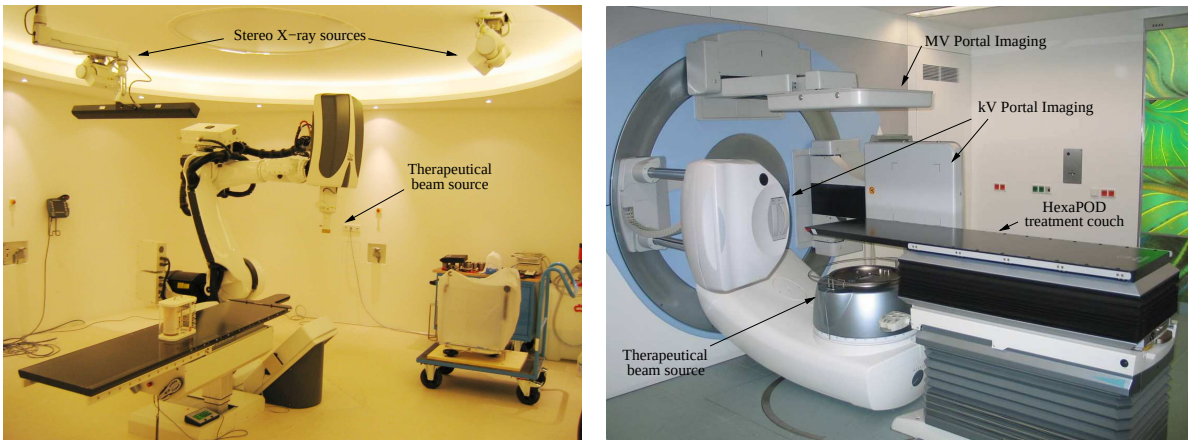

(a) Cyberknife®-Radiosurgical System (b) Linear accelerator with HexaPOD™ couch

Figure 4.5: On the left, the Cyberknife® Radiosurgical System is displayed. On the right the setup of a linear accelerator with an integrated HexaPOD™ treatment couch is shown.

However, it is important to consider that both gating and active tracking have latencies due to physical limitations of the particular technique. The correlation allows the computation of the target volume's position only, but the therapeutic beam has to reach the target volume, which is moving, early enough. Therefore, predictive tracking uses the periodicity of the particular anatomical signal, e.g. respiration or pulsation, in order to compensate for this latency.

4.3 Résumé

In this chapter the novel system for *fiducial-less* tracking of tumors moving due to respiration was introduced.

A 4D patient model of the specific region in the patient's body forms the basis of this method, enabling a prediction of the target position at a certain time. This model consists of a number of artificial scans, each representing one particular respiratory state. By matching periodically taken X-ray images to the deformation model, the breathing phase and therefore the position of the tumor can be determined. To permit the determination of the target position in real-time, infrared emitters are attached to the patient's chest and abdomen to report information on the current breathing phase. The readings of the sensor are correlated to the target locations obtained by comparing the X-ray images to the model. Thus, a correlation model between external and

internal motion is obtained without using any implanted fiducials.

In chapter 6 the process creating the volumetric deformation model is described in detail, which constitutes the main part of this thesis. Chapter 7 focuses on the 2D-4D registration procedure, needed for inferring the breathing phase. The next chapter explains some new methods for labeling CT images with respiratory states, well suited for evaluating the computed 4D patient models.

5 Data Acquisition

The creation of synthetic 4D models of internal organs poses the question of how the results are to be verified. Corresponding image data with known respiratory state is needed to be able to compare the artificial images to real images. Thus, the quality of the deformation performed, can be evaluated. The most obvious way is to take 4D real CT Scans with a fast multi slice scanner, but our clinical partner did not have this possibility. Therefore, some alternative new methods were created to get information about the internal organs at different respiratory states. They can be classified in two main categories: taking images (1) respiratory-gated while the patient is breathing freely or taking images (2) during breath-hold.

5.1 Respiratory Gating

Respiratory gating means that images are taken with a particular imaging device during free breathing. These images are afterwards registered to respiratory states, gained from an external or internal respiratory signal.

5.1.1 Labeling CT Images with Respiratory States Using Optical Tracking

The first approach pursued for this work was to take images of the patient breathing freely with a spiral CT scanner (Philips Tomoscan AV) and simultaneously follow the movement of the chest or abdomen, caused by respiration, by the use of an infrared tracking camera. An emitter attached to the patient's chest or abdomen reports information about the current breathing state. The challenge is to synchronize the readings of the tracking camera with the acquisition of the single slices. This is solved by the use of an additional emitter attached to the treatment table, which measures the longitudinal position of the patient relative to the CT gantry. The two emitters are related to each other by means of a time stamp. Thus, by comparison of the z-coordinates of the emitter mounted on the table with the slice locations of the images, the corresponding respiratory state is obtained.

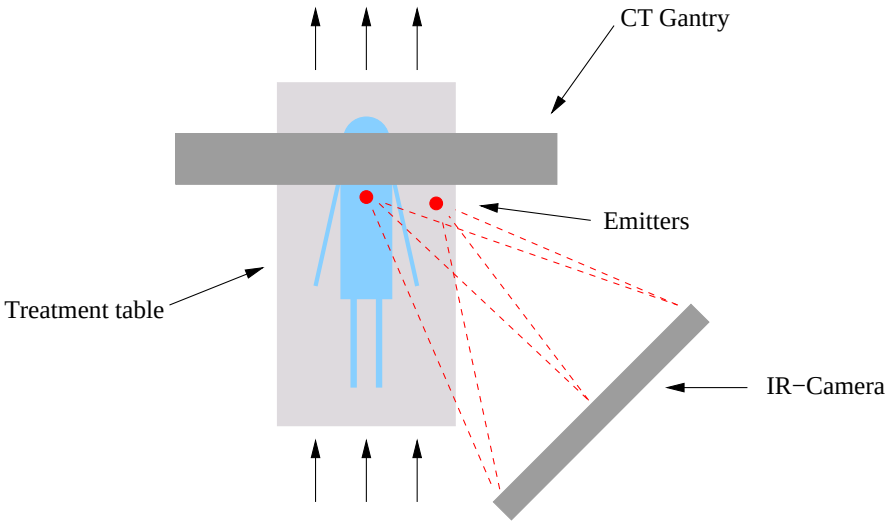

Figure 5.1: The setup of the system to get single CT slices of a patient with assigned breathing state by using optical tracking.

If the different slice locations are not unique, because several scans were performed, then the time stamps of the single image slices also have to be considered for this assignment. The method was tested with six patients. Additionally to the scan performed during free breathing, two scans, maximal inhaled and exhaled, were taken in order to be able to create the synthetic 4D model (Figure 5.3) and to compare the slices to the 4D model.

Calibrating the System

As the position data of the emitter mounted on the treatment table can only move in one direction, that is towards the gantry, calibration is done without the use of any external calibration tools. Instead first the covariance matrix of the samples of points is determined.

$$A_{Cov} = \begin{pmatrix} Cov(x) & Cov(x,y) & Cov(x,z) \\ Cov(x,y) & Cov(y) & Cov(y,z) \\ Cov(x,z) & Cov(y,z) & Cov(z) \end{pmatrix}$$

Next step is to compute the eigenvectors of the covariance matrix.

$$A_{Cov} \cdot \vec{x} = \lambda \cdot \vec{x}$$

Then the center of mass of all the samples and the maximal eigenvector are used to determine

the regression line.

$$X_{Reg} = \begin{pmatrix} \bar{x} \\ \bar{y} \\ \bar{z} \end{pmatrix} + \mu \cdot \max(\vec{x}) \qquad \mu \in \mathbb{R}$$

A_{Cov} the covariance matrix.

λ the eigenvalues.

$\vec{x}$ the eigenvectors.

μ the scaling factor of the line's direction vector.

X_{Reg} the regression line.

A transformation matrix is built, which maps the point (0, 0, 0), the z-axis and the x-axis to the center of mass of the samples, the maximal eigenvector and a vector perpendicular to the maximal eigenvector.

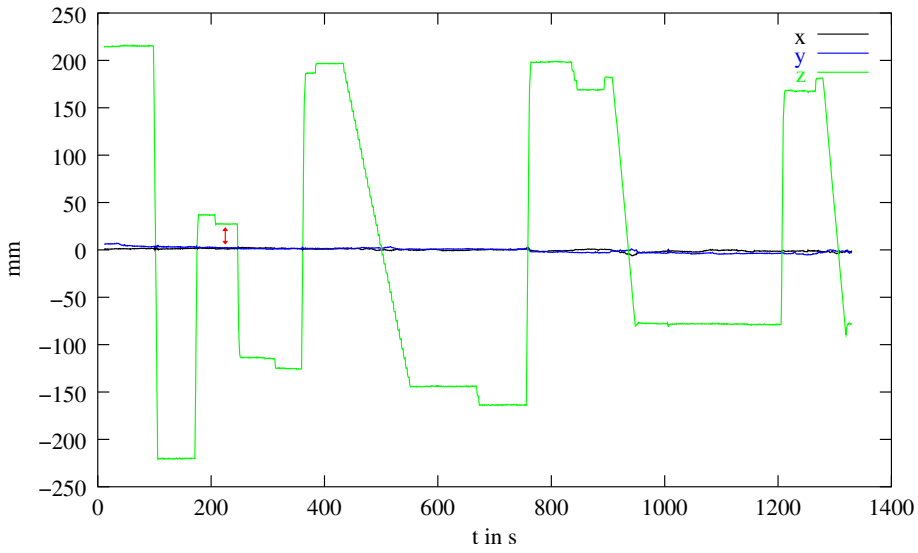

Figure 5.2: The coordinates of the emitter, placed on the treatment table, are displayed above. The red arrow is located at the point in time, at which the slice at location 0 is taken. Its length shows the misalignment of z after the described transformation. Translating the z coordinate of the emitter data to 0 yields a calibrated system.

After transforming all emitter data by this homogenous matrix there may be an error of sign, but this can be easily detected by comparison of the transformed emitter data (Figure 5.3) and the table movement of the imaging device. Thus, the direction is known in which the points

have to be transformed, but the distance relative to the gantry is still missing. Therfore a slice at position 0 is taken at the beginning of the procedure.

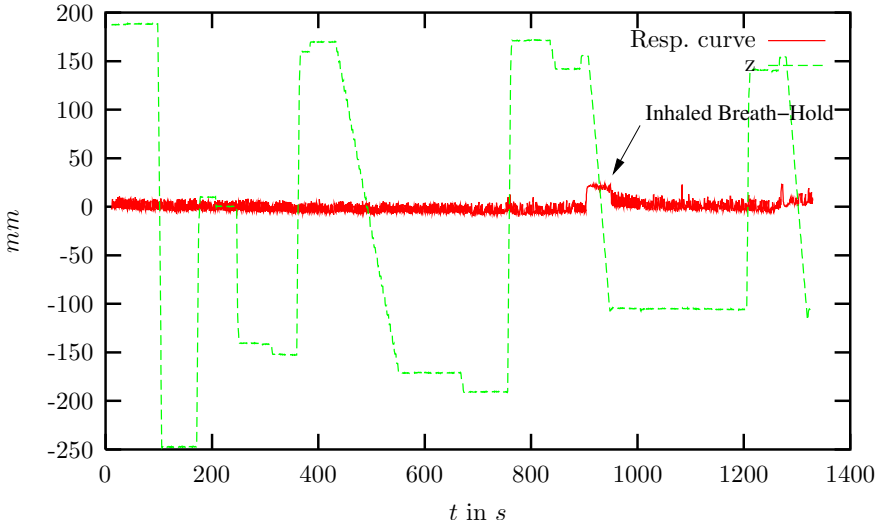

Figure 5.3: In this plot the data recorded from the two emitters is displayed. From the emitter attached to the patient's body the respiratory curve is obtained. The second emitter demonstrates the movement of the treatment table relative to the gantry. In this case three scans have been performed with the spiral scanner, i.e. from ca. 400 – 550 s, 900 – 950 s and finally from 1300 – 1350 s. It can be seen that during the second scan the patient held his breath at maximal inspiration.

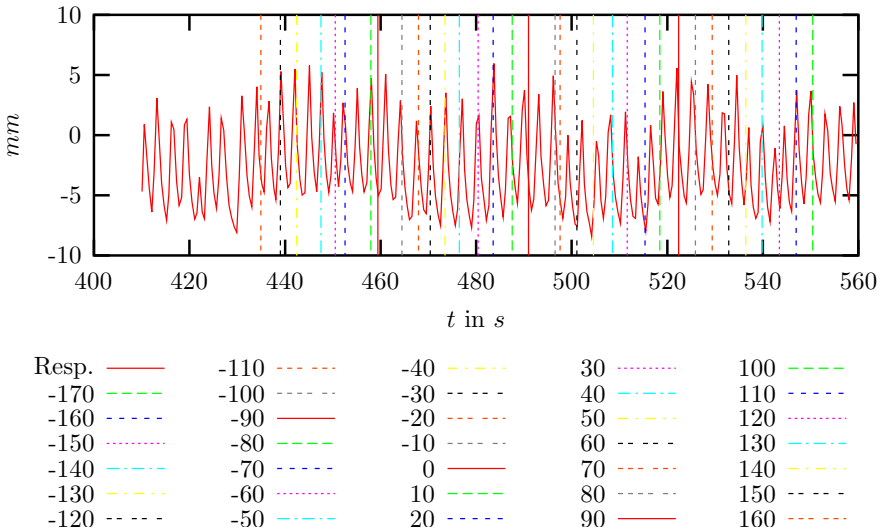

Figure 5.4: The final result, assigning respiratory states to every single slice. Each vertical line represents one particular slice.

Thus, calculating the difference between the acquisition time of this image and of the first slice of the subsequently performed scan and considering the corresponding plot, yields the needed translation of the z-coordinates, as described in Figure 5.2. A final result for assigning single slices to respiratory states can be seen in Figure 5.4.

5.1.2 Labeling CT Images with Respiratory States by Using a Needle

The second approach realizes the labeling of CT images with respiratory states by the setup displayed in Figure 5.5. A needle, connected to the patient's chest/abdomen follows respiratory motion. The needle goes through the gantry and is therefore visible in every single CT slice.

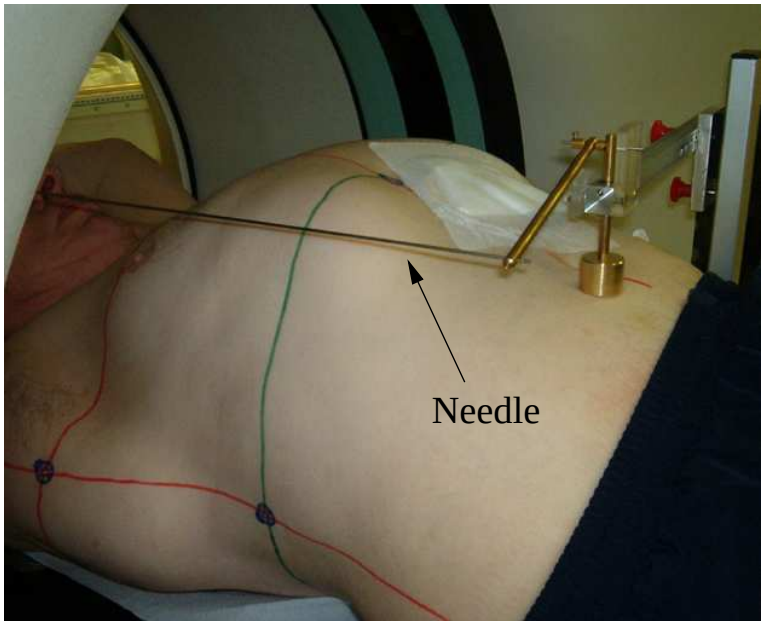

Figure 5.5: The respiratory motion of the patient makes the needle move up and down. The lift is intensified by an integrated leverage effect. A harmless side effect is the reversion of the direction of the moving needle (Figure 5.9).

Thus, the position of the needle in every CT slice gives information about the current state of respiration (see Figure 5.7). As can be seen in Figure 5.7, the needle causes some reflections in the CT image. Tests were made with a plastic needle and a steel needle in stationary and moving mode. This showed that the artifacts are mainly due to movement and not to the small amount of metal in the image (Figure 5.6). Therefore, the more rigid and better visible hollow steel needle was chosen for the tool. The center of mass of the needle data in every slice was taken as indicator for the current respiratory state.

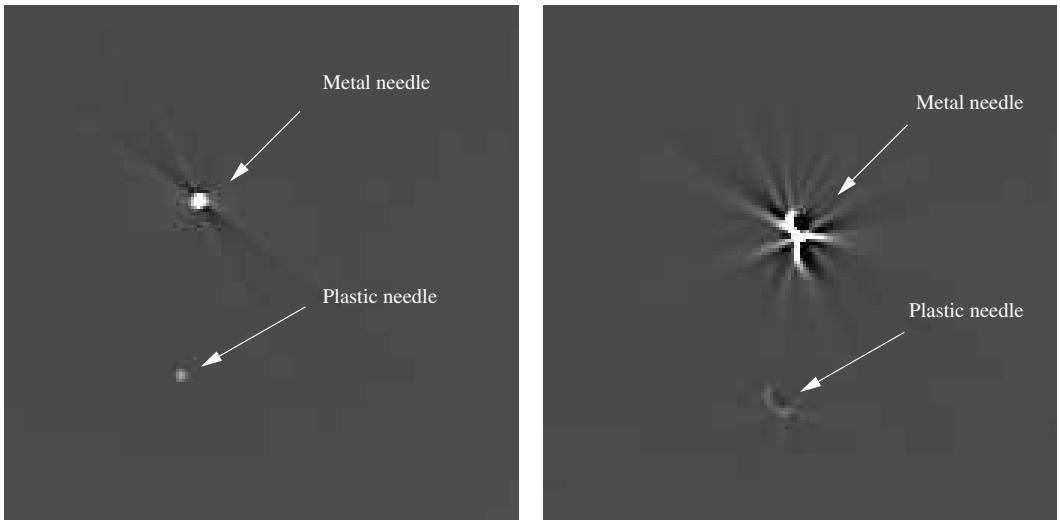

(a) Stationary mode (b) Moving mode

Figure 5.6: When in movement, both materials (metal as well as plastic) cause artifacts, whereas in stationary mode, the occurrence of artifacts is greatly reduced.

(a) Transversal view (b) Sagittal view

Figure 5.7: (a) The needle is visible in the upper left corner. The rectangle has to contain the needle in all slices of the free breathing CT series. The point within the rectangle represents the current center of mass. (b) Sagittal view of the free breathing volume scan at the position of the needle. The scattered line on top shows the moving needle, that is directly the respiratory curve.

A small software tool has been developed to assign respiratory states to the slices. First the image is transformed to a binary image by windowing the image with a center corresponding to the density values of the needle and a window width of 0. The user has to draw in a rectangle, which surrounds the needle in all slices (Figure 5.7(a)). After that the centers of mass in all images are calculated and are taken as location of the needle. Comparing the needle positions to each other yields a respiratory state for each slice.

Images with known respiratory state, well suited for evaluating the deformation results, were acquired using this method for nine patients. The density of the resulting model certainly depends on the number of scans performed for the specific patient.

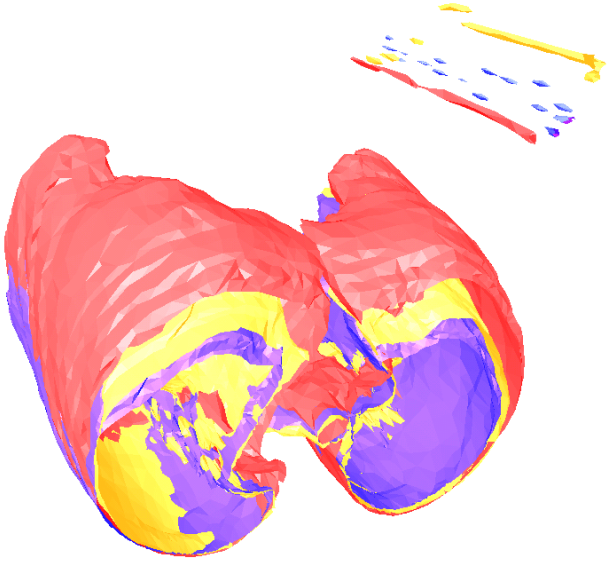

Figure 5.8: The lung was segmented in the acquired scans, taken during inhalation, exhalation and free breathing. The inhaled lung is displayed in red, the exhaled lung in yellow and the lung during free breathing is displayed in blue. In the upper right corner the corresponding needle can be seen. In case of exhalation, by following the needle information, it can be noticed that the patient couldn't hold his breath for the complete scanning time. An very important information with respect to the creation of the 4D patient model.

As in the breathing cycle the amount of time during which the lung is in relaxed, exhaled state is always greater than that during which the lung is in inhaled state, the models are often denser in the state of exhalation. In Figure 5.9 results of two data sets are visualized.

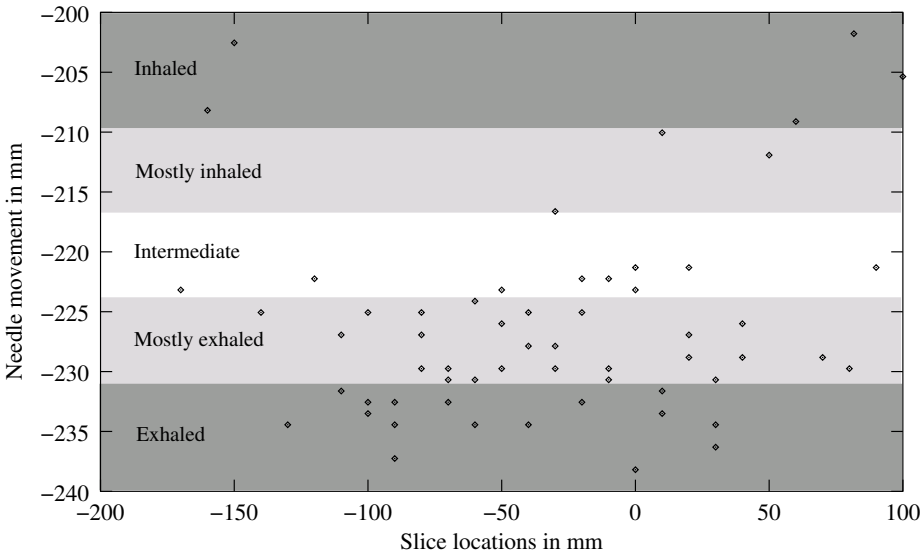

(a) Free breathing

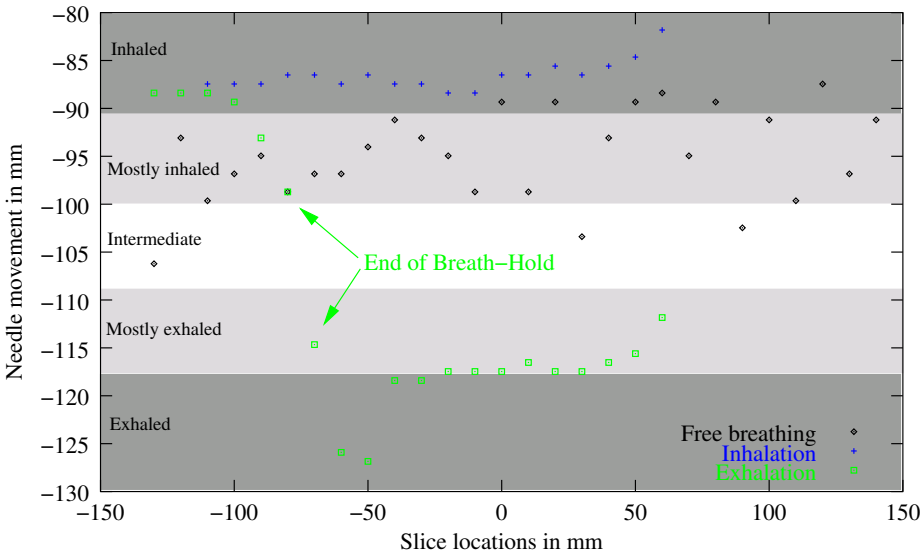

(b) Breath-hold and free breathing

Figure 5.9: (a) This graph displays the moving needle position in three scans of one patient performed during free breathing. The models are more dense in the states of exhalation, because the amount of time within the breathing cycle of a relaxed, exhaled lung is always more than that of an inhaled. (b) Two scans were performed during breath-hold (inhalation and exhalation) and one scan was performed free breathing. It is interesting to observe that, in case of exhalation, the patient could not hold his breath for all the time (time runs from right to left).

In this case, the thresholds for assigning different respiratory states were calculated by taking the difference between maximum and minimum needle position in anterior posterior direction and dividing it into four parts of equal size. Figure 5.8 shows the triangulated surfaces of a segmented lung taken during inhalation, exhalation and free breathing of one specific patient, in each case with the corresponding needle information.

The utilized needle tool was a prototype used to demonstrate the feasibility of the method. Improvements of the mechanics and the material of the needle are certainly possible.

5.1.3 Related Work

5.1.3.1 Labeling CT Images with Respiratory States by Using a Spirometer [Low 03]

Low et al. prefer a spirometer[1] for obtaining information about the current state of respiration during free breathing CT image acquisition. CT scans are taken free breathing and simultaneously volume information is recorded by the spirometer. Thus, images are acquired providing knowledge of the lung's current volume. These are sorted into user-defined volume intervals in order to get a 4D image.

5.1.3.2 4D-CT Imaging by Using Cine Scans [Pan 04]

At each table position a cine scan for data acquisition is performed. Taking several CT image slices successively at one specific table position is called a cine scan, often also referred to as "dynamic scan". The duration of one scan is greater than or equal to the average respiration cycle plus the time needed for image reconstruction. Thus, dynamic scans, showing the movement due to respiration at each table position, are obtained. Subsequently, the image data is registered into respiratory states by matching in each case the two neighboring dynamic scans in consecutive respiratory cycles, according to their anatomical correlation.

5.2 Breath-Hold Techniques

This technique requires that the respiration of the patient pauses during image acquisition. Thus, a complete 3D scan of one particular respiratory phase can easily be obtained. A distinction can be made between forced and voluntary breath-hold techniques.

[1] A spirometer is an instrument that measures the amount of air, which moves in and out of the lungs

5.2.1 Breath-Hold MRI Images

Volunteers were asked to hold their breath at different respiratory phases during acquisition of images of the liver with magnetic resonance imaging. Scans were performed at the following breathing states: maximal exhalation, maximal inhalation and at least at one intermediate state, located approximately in the middle of the respiratory cycle. Therefore, complete 3D scans of intermediate respiratory states were obtained, well suited for evaluating the computed synthetic 4D models (see chapter 6).

One might assume that this could lead to inaccurate results. However, in a study including 20 patients Onishi et al. [Onishi 03] explored how precisely patients can reproduce the breathing state, and therefore the tumor position, without the use of any respiratory monitoring devices. Self-breathing hold initiated by the patient's own estimation led to more accurate tumor positions than that initiated by verbal command of an expert. Mean maximum difference in tumor position was 2.2 mm along the cranial-caudal, 1.4 mm along the anterior-posterior and finally 1.3 mm along the right-left axis, representing a satisfactory accuracy.

5.2.2 Related Work

The next section describes the approach by Wong et al., which enables to take whole scans of one particular respiratory phase by exposing the patient to a forced breath-hold.

5.2.2.1 J. W. Wong et al. [Wong 99]

This approach makes use of Active Breathing Control (ABC), a forced breath-hold technique, to reduce breathing motion during image acquisition and radiation. The constructed apparatus consists of a ventilator with two separate flow monitors and two valves. Thus, inhalation and exhalation can be controlled and monitored independently. The patient is connected to the device by a mouth-piece. With the help of a software tool, one can set the direction of flow and the wanted lung volume for closing the valves, yielding immobilized respiratory motion of the patient. Therefore, images with any imaging device can be taken at any breathing phase. Active breath-hold using ABC was performed for 12 patients. The duration of active breath-hold, at state of nearly complete exhalation, varied from 15 to more than 40 seconds, depending on the patient.

5.3 Résumé

The new approaches presented for obtaining 4D patient image data, by correlating CT slices to the breathing status are both very simple to perform and work (sections 5.1.1 and 5.1.2). However, the method using the needle to follow respiratory motion obtained more acceptance in the clinic, because it is simple and inexpensive. It works with every CT scanner, as no signal has to be fed into the scanner. The respiratory status is "burned" into each image. No additional data are necessary, which would have to be attributed to both the breathing status and the image. Both methods are not only useful for creating evaluation data, but also to ensure that the patient actually held his breath during the initial data acquisition, needed for creating the 4D patient model (see Figure 5.9(b)).

The approach of Pan et al. (see section 5.1.3.2) has the drawback that only 4D models with small slice distances can be obtained, because of the need for correlations in anatomy when sorting the images to breathing states. Therefore, a high radiation dose is applied to the patient. Using a spirometer (section 5.1.3.1) for respiratory gating means a big loss in comfort for the patient. A general drawback of methods based on respiratory gating is that the resulting 4D models often are not uniformly distributed, because of the fact that the amount of time during which the lung is in relaxed, exhaled state is always greater than that during which the lung is in inhaled state. Thus, the models are often denser in the states of exhalation.

With breath-hold techniques whole scans can easily be taken at one single respiratory state, without any complicated assignment of images to respiratory phases. However, this raises an important question: do images taken during breath-hold represent a state, that really occurs during free breathing? This is an important premise for evaluating the 4D model. Blackall states the same doubt in her thesis [Blackall 02].

In general, methods for generating 4D image data of the patient, are not only important for evaluating deformation techniques. When segmenting internal organs for creating a radiotherapy treatment plan, a 3D image of the appropriate organ of one particular breathing state is required. If the whole 3D image is gained from one scan taken during free breathing, the occurrence of artifacts is unavoidable and thus an accurate segmentation of the organ cannot be performed. Therefore, a precise radiation cannot be guaranteed.

6 Volumetric Deformation Model

Within the application of tracking tumors without using fiducials, described in chapter 4, the creation process of the 4D model plays an important role. The model gives information about the deformation due to respiration and therefore enables the system to determine the position of the target and its surrounding critical organs at every single respiratory state. Matching live-images (radiographs) to the model, yields the current respiratory state and thus the location of the tumor. Two initial volume scans, taken during inhalation and exhalation represent the starting basis. Landmark-based morphing methods are evaluated according to their relevance for creating the model. Another key issue is the automatic determination of corresponding anatomical landmarks between the two initial scans, needed for initializing the deformation of the volume. An important aspect is that not only the deformation of the diseased organ is of interest with this approach, but the deformation of the complete region around the tumor. Especially the changing relative positions of bones to each other due to respiration, for example of sternum to specific vertebral bodies, is very important to the later 2D-4D registration process (see chapter 7), because of the fact that especially bony structures are visible in the X-ray images taken to determine the respiratory state. This chapter is structured as follows: in section 6.1 the used landmark-based deformation methods are introduced in detail. A novel method for fully automatic detection of corresponding anatomical landmarks in volume scans of different respiratory state is described in section 6.1.3. The evaluations performed on six patient data sets are presented in section 6.3. Finally a résumé is given, which summarizes the results and comments on the related work of section 6.2.

6.1 Landmark-Based Deformation Methods

Two landmark-based methods were considered for creating the volumetric deformation model, one based on barycentric coordinates and the other on thin-plate splines. Both methods need as input:

1. Two initial volume scans, taken during inhalation respectively exhalation (Figure 6.1).

They both have to be in the same coordinate system to create the model. If they are not, a global rigid registration based on hard tissue has to be performed.

2. The number of desired respiratory states, and therefore image stacks representing the 4D model. With respect to the deformation, this number is equivalent to the number of interpolation steps.

3. An arbitrary amount of pairs of corresponding control points (anatomical landmarks), characterizing the deformation caused by respiration.

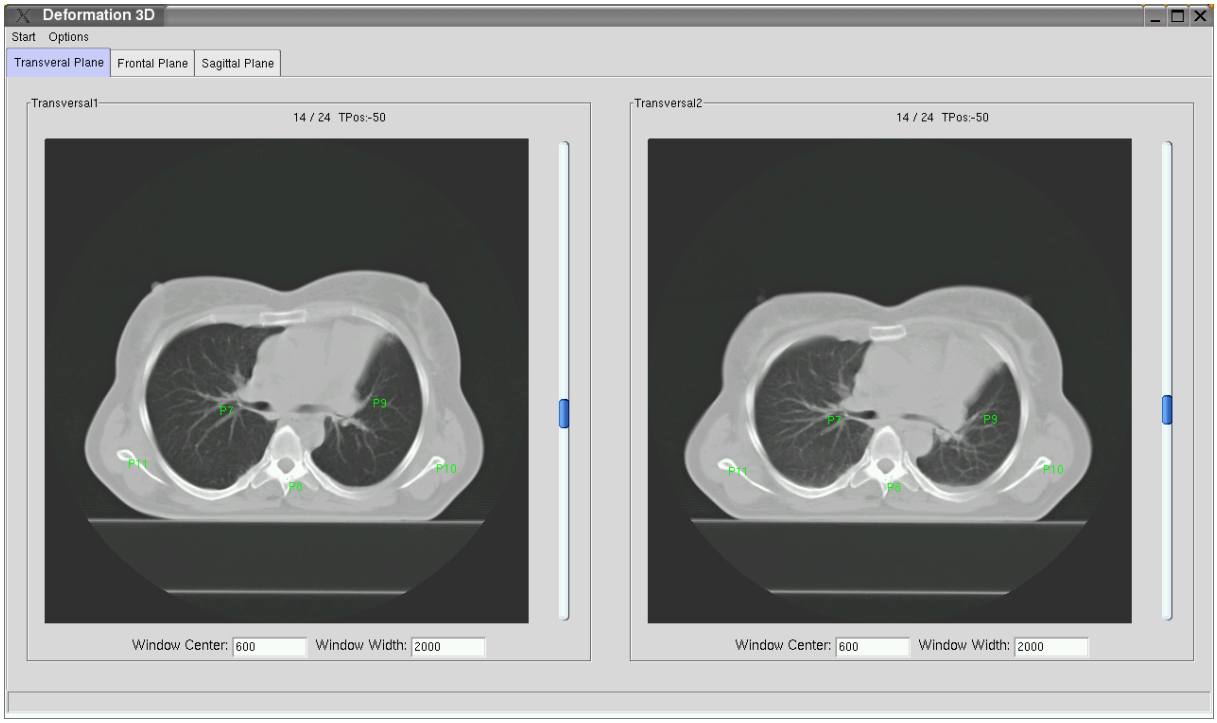

Figure 6.1: A screenshot of the application for creating 4D models of internal organs, developed within this work. On the left one can slide through the inhalation data set and on the right through the exhalation data. Selected corresponding anatomical landmarks can be seen, colored in green.

Very important to remark is, that with respect to both deformation methods, only the intensities of one volume are considered for computing the intensities of the particular synthetic scans of the volumetric deformation model. The information obtained by the reference volume are the positions of the corresponding anatomical landmarks.

In the following sections the two deformation methods and the new technique for fully automatic detection of corresponding anatomical landmarks are described in detail.

6.1.1 Deformation by Barycentric Coordinates

The barycentric coordinates [Weisstein 99] were introduced by Möbius[1] in 1827 and represent a frequently used tool with respect to morphing. In 3D space a barycentric coordinate represents a quadruple of weights concerning the location of a specific point P within a surrounding tetrahedron. The barycentric coordinates are proportional to the ratio of the directed distances from P to the side planes (triangles) and therefore also of the volumes of the tetrahedrons ABCP, ABDP, ACDP and BCDP (Figure 6.2) to each other. Normalizing the sum of these directed distances yields the barycentric coordinates.

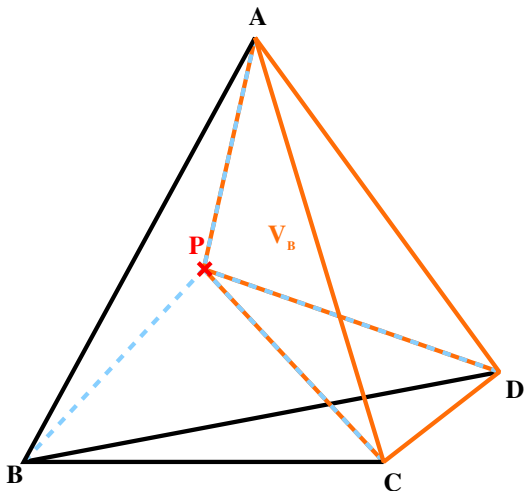

Figure 6.2: Point P, to be expressed in barycentric coordinates, is located inside the tetrahedron with vertices A, B, C and D. The relative size of the volume marked in orange, $V_B = ACDP$, with respect to the three remaining volumes, determines the influence of point B on point P.

Finally the weights are determined by solving the following linear system of equations.

$$P.x = w_1 A.x + w_2 B.x + w_3 C.x + w_4 D.x \quad (6.1)$$

$$P.y = w_1 A.y + w_2 B.y + w_3 C.y + w_4 D.y \quad (6.2)$$

$$P.z = w_1 A.z + w_2 B.z + w_3 C.z + w_4 D.z \quad (6.3)$$

$$1 = w_1 + w_2 + w_3 + w_4 \quad (6.4)$$

Before computing the barycentric coordinates, the volume first has to be tessellated into tetrahe-

[1] August Ferdinand Möbius (1790-1868): German mathematician and astronomer

drons with preselected control points as vertices. This is done by using Delaunay[2] tetrahedrization [O'Rourke 94], which is characterized by the fact that every circumsphere of a tetrahedron is empty, i.e. it contains no other points. The center of each circumsphere is a vertex of the corresponding Voronoi[3] diagram (Figure 6.3). A delaunay triangulation is the straight-line dual to its corresponding Voronoi diagram.

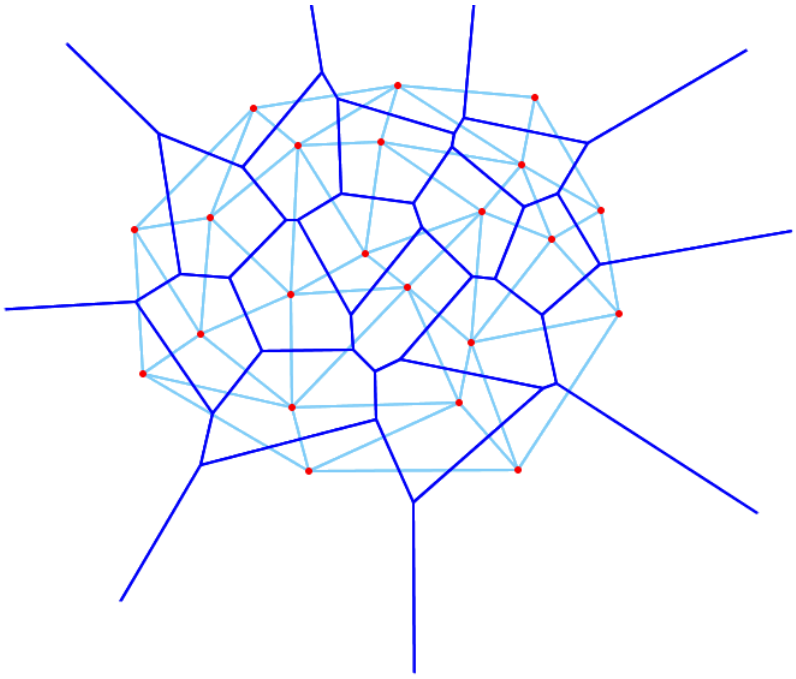

Figure 6.3: Example in the plane: Voronoi diagram (blue) with corresponding Delaunay triangulation (light blue) for a given set of points. A Voronoi diagram divides a plane containing points into convex polygons, whereas each polygon only contains the generating point. The nearest point of every location inside a certain polygon is the generating point.

Applying these techniques to the process of deforming volume scans due to respiration yields the following procedure: First the two volumes are tessellated into tetrahedrons by Delaunay tetrahedrization. The control points and the 8 vertices of the bounding box of the volume are used as vertices for this tetrahedrization. The previously detected corresponding anatomical landmarks serve as control points. During deformation, the vertex positions are linearly interpolated over time (same procedure as with thin-plate splines, see Figure 6.6). The number of interpolation steps certainly depends on the desired number of synthetic scans to model the vol-

[2]Charles-Eugene Delaunay (1816-1872): French mathematician and astronomer
[3]George Voronoi (1868-1908): Ukrainian mathematician

umetric deformation. In each interpolation step, the barycentric coordinates are calculated in relation to the enclosing tetrahedron, for all the points of the actual stack. Using these weights the change in position of every pixel value of the source image is determined. The information of the reference image is not considered for computing the intensities of the deformed images.

6.1.2 Deformation by Thin-Plate Splines

A thin-plate spline interpolates a surface that is constrained not to move at given control points. This surface represents a thin metal plate, which will be deformed into the most economic shape, in reference to its bending energy. Thin-plate splines were introduced by Duchon in 1976 [Duchon 76], but the first to consider them as a morphometric tool for biological data was Bookstein [Bookstein 89].

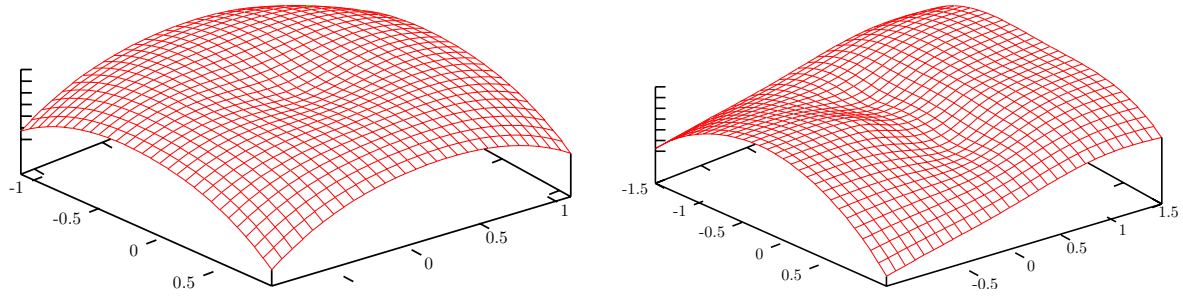

(a) U(r) (b) Linear combinations of U(r)

Figure 6.4: a) A force $\vec{F}$ affects the thin metal plate at point $(0,0)$, yielding a deformation expressed by the equation $U(r) = z(x,y) = r^2 ln(r^2)$, whereas r is the euclidian distance from the origin. The value of $z(x,y)$ determines the degree of deformation in point (x,y). b) Now the thin metal plate is tacked at four points $(0,\pm 0.5)$ and $(\pm 0.5,0)$. The resulting deformation is expressed by a linear combination of $U(r)$, that is $z(x,y) = U(\sqrt{[x^2+(y-0.5)^2]}) - U(\sqrt{[(x+0.5)^2+y^2]}) + U(\sqrt{[x^2+(y+0.5)^2]}) - U(\sqrt{[(x-0.5)^2+y^2]})$.

In this work these splines are used to model a biological homology, that is internal organs at different respiratory states, sampled by corresponding landmark data. The thin-plate spline function for calculating the transformation of voxels within the deformation process is:

$$f_{tps}(x,y,z) = a_1 + a_x x + a_y y + a_z z + \sum_{i=1}^{K} w_i U(|Z_i - (x,y,z)|) \tag{6.5}$$

The function consists of an affine part, which represents the behavior of f_{tps} at infinity, and a linear combination of radial basis functions $U(r)$. 'Radial', because only the euclidian distance and not the orientation between the current voxel and the particular control point is relevant for the function. In 2D space $U_{tps} = r^2 ln(|r|)$ is used as radial basis function, whereas in 3D space $U_{tps}(r) = |r|$ is used. r represents again the different euclidian distances between the point to be transformed and each of the landmarks of the original data.

f_{tps} minimizes the bending energy of the deformed thin metal plate, represented by this quantity:

$$\int\int\int_{R^3} [(\frac{\partial^2 f}{\partial x^2})^2 + (\frac{\partial^2 f}{\partial y^2})^2 + (\frac{\partial^2 f}{\partial z^2})^2 + 2(\frac{\partial^2 f}{\partial x \partial y})^2 + 2(\frac{\partial^2 f}{\partial x \partial z})^2 + 2(\frac{\partial^2 f}{\partial y \partial z})^2] \mathrm{d}x\mathrm{d}y\mathrm{d}z \tag{6.6}$$

The determination of the weights $w_1 ... w_n$ as well as of the coefficients a_1, $a_x x$, $a_y y$, $a_z z$ adapts the interpolation function to the given control points. Their values are computed by solving the following equation:

$$L^{-1} * \begin{pmatrix} v_1 \\ \vdots \\ v_n \\ 0 \\ 0 \\ 0 \\ 0 \end{pmatrix} = \begin{pmatrix} w_1 \\ \vdots \\ w_n \\ a_1 \\ a_x \\ a_y \\ a_z \end{pmatrix} \tag{6.7}$$

whereas v_1 ... v_n represent the landmarks corresponding to those of the original data. The matrix L is defined as follows:

$$L = \left(\begin{array}{c|c} P_n & Q \\ \hline Q^T & 0 \end{array} \right), \qquad (n+4) \times (n+4), \tag{6.8}$$

whereas,

$$P_k = \begin{pmatrix} 0 & U(r_{12}) & \dots & U(r_{1n}) \\ U(r_{21}) & 0 & \dots & U(r_{2n}) \\ \dots & \dots & \dots & \dots \\ U(r_{n1}) & U(r_{n2}) & \dots & 0 \end{pmatrix}, \qquad n \times n, \tag{6.9}$$

and

$$Q = \begin{pmatrix} 1 & x_1 & y_1 & z_1 \\ 1 & x_2 & y_2 & z_2 \\ \vdots & \vdots & \vdots & \\ 1 & x_n & y_n & z_n \end{pmatrix}, \qquad n \times 4. \tag{6.10}$$

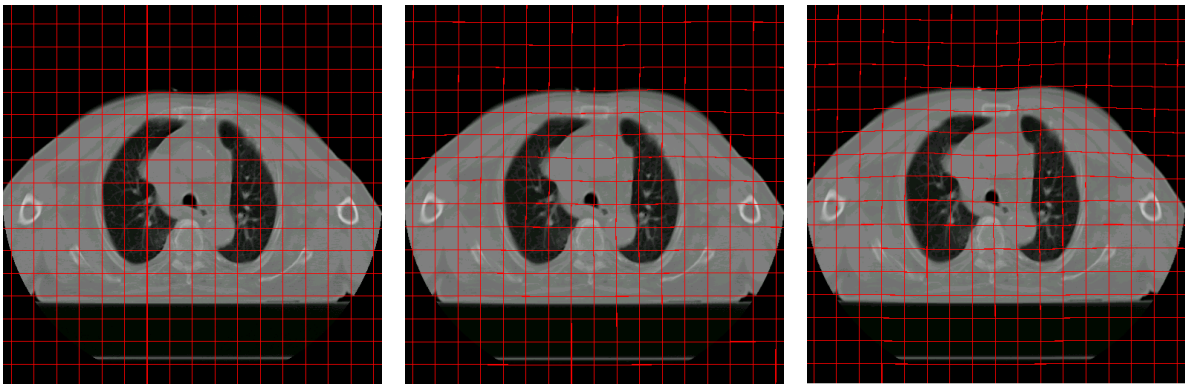

(a) Exhalation (b) Near exhalation (c) Intermediate 1

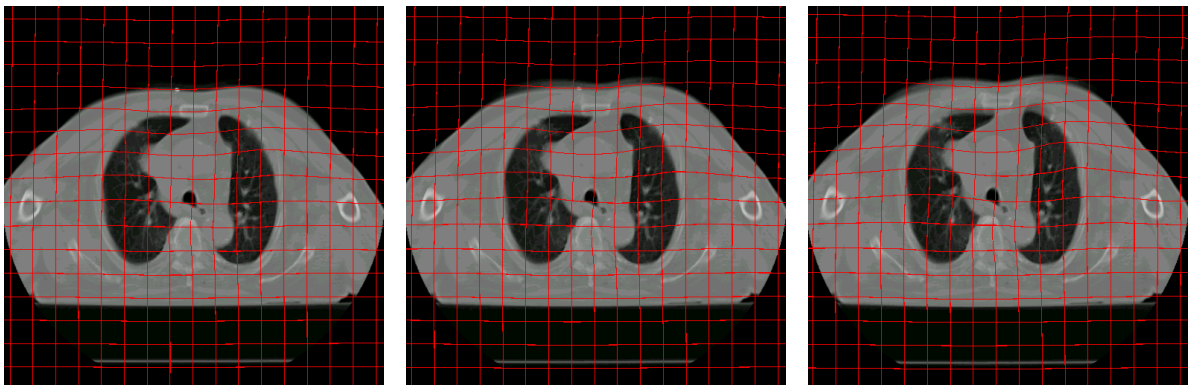

(d) Intermediate 2 (e) Near inhalation (f) Inhalation

Figure 6.5: A deformation performed using thin-plate splines on an MR scan of the liver. Each image was taken at the same slice location, but belongs to a different respiratory state within the created 4D model. The grid visualizes the deformation in anterior-posterior and left-right direction. The deformation in cranial-caudal direction can be followed by regarding the changing anatomical landmarks.

The novel method for creating volumetric deformation models uses the thin-plate splines as follows: the connecting lines of the corresponding control points are linearly interpolated over time

and in each interpolation step the coefficients of the thin-plate spline function are determined (see Figure 6.6). The number of interpolation steps depends on the number of desired synthetic target scans, and therefore respiratory states, forming the model. This method deforms the exhalation scan into the inhalation scan step by step, yielding the volumetric deformation model, needed to infer the respiratory state. In Figure 6.5 an example of a deformation performed using thin-plate splines is shown.

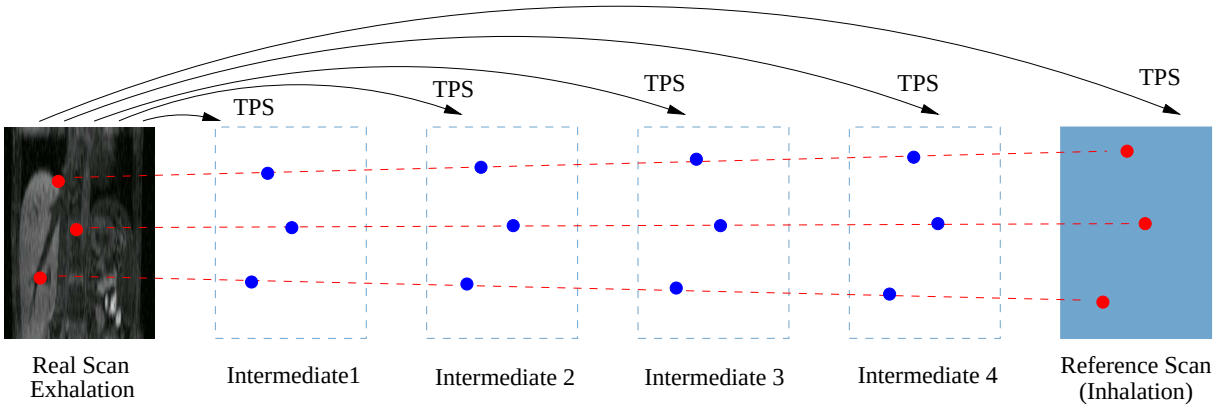

Figure 6.6: The connecting lines of the corresponding anatomical landmarks are linearly interpolated over time and in each interpolation step the thin-plate spline function is determined. Only the image information of the volume to be deformed is used for creating the model. The information gained by the reference volume are only the landmark correspondences.

6.1.3 Determination of Corresponding Anatomical Landmarks

Crucial for an accurate 4D patient model certainly is the selection of the corresponding anatomical landmarks, that is the control points for the deformation method applied to the source scan. The control points have to be uniformly distributed within the volumes and their combination has to be meaningful for characterizing the occurring respiratory motion. For example landmarks located in the spine are not meaningful for this characterization, but in combination with landmarks located in the sternum they certainly are. With respect to the number of control points Meyer et al. [Meyer 03] found 24 landmarks to be sufficient to model changes of the liver shape. Coselmon et al. [Coselmon 04] selected 30 landmarks to describe the occurring motion in one lobe of the lung.

The volumetric deformation model needed for determining the respiratory state shall not only model the deformations of one specific organ, but also of the surrounding tissues (also bony structures). Thus, more control points are required. The amount varies approximately between 80 and 120. In Figure 6.7 an example of one particular control point pair is given.

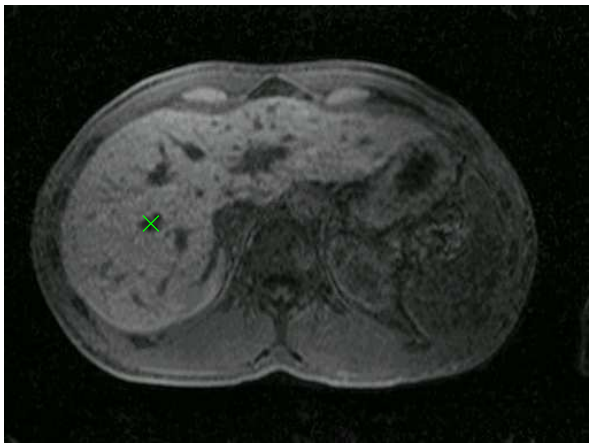

(a) Transversal slice inhaled

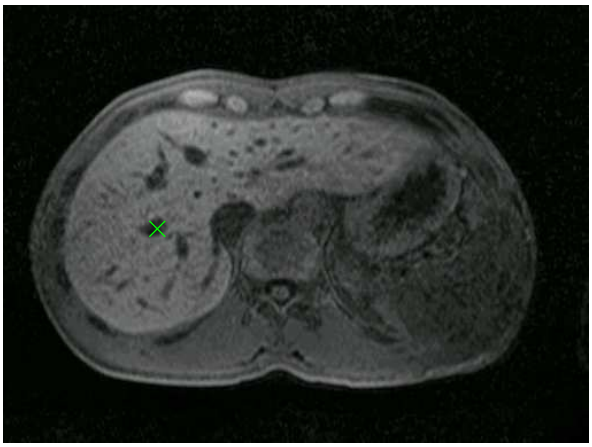

(b) Transversal slice exhaled

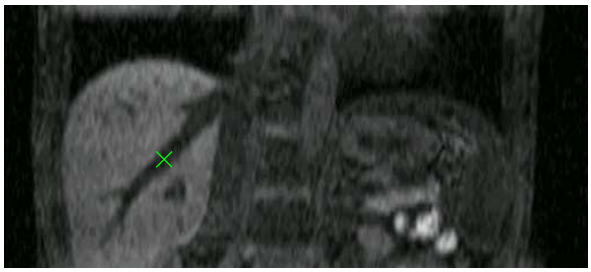

(c) Frontal slice inhaled

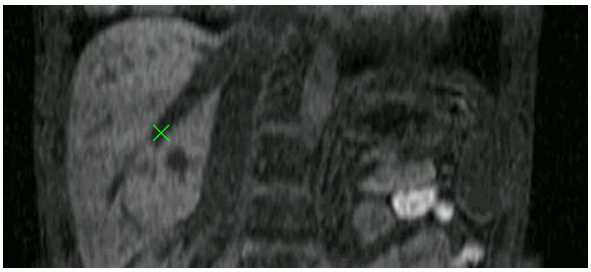

(d) Frontal slice exhaled

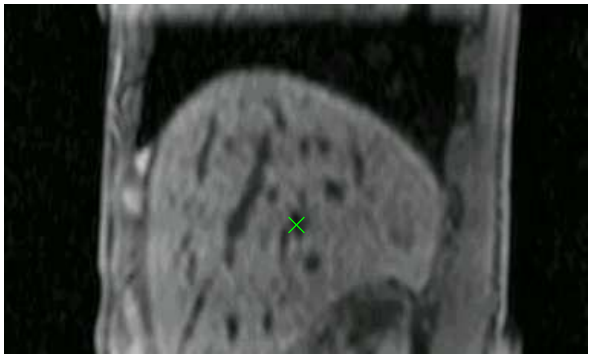

(e) Sagittal slice inhaled

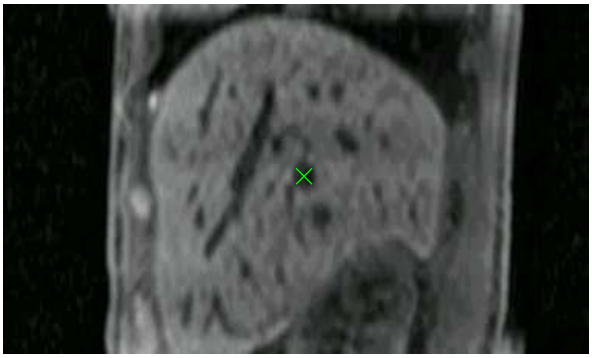

(f) Sagittal slice exhaled

Figure 6.7: In these images one particular control point pair, a vascular landmark located in the liver, is displayed in the transversal, the frontal and the sagittal plane. In the application frontend the user can verify in all these three planes the correctness of the automatic anatomical landmarking's result. The scans were taken by magnetic resonance imaging.

Corresponding anatomical landmarks of two CT scans of the same region but different respiratory state are needed as input to create the 4D model. Selecting all these control points manually is possible but very time consuming. Frangi et al. [Frangi 01] suggested a method for automatic landmarking, which uses non-rigid registration techniques to propagate landmarks manually detected in one respiratory state to the remaining ones. The semi-automatic landmark localization from Rohr et al. [Rohr 96] applies 3D differential operators to given regions of interest in order to detect landmarks by analyzing their geometrical structure. New methods for assisting the selection process of corresponding anatomical landmarks, created within this work, are presented in the next sections. First a method is introduced, which refines the user selected control point pairs. Then an extension of this technique enabling fully automatic detection of corresponding anatomical landmarks is described.

6.1.3.1 Refinement of Selected Corresponding Anatomical Landmarks

First enhancement in selecting the corresponding control points is the sharpening of the manually selected anatomic landmarks. The idea is to compensate for user selections of only roughly corresponding anatomical landmarks. The method matches the surrounding cube of a landmark to a slightly larger cube of the corresponding landmark of the other respiration state. This very fast local rigid registration is performed for every manually selected control point pair of the volumes. The size of the cube of the floating image is about 64 cm^3 and, compared to this, the size of the cube of the fixed image is enlarged by 30 % in each dimension. The size of the cubes are determined by the user and depend on the amount of deformation occurring due to respiration. The metric and optimizer used were correlation coefficient and gradient descent, respectively. In this case the implementation is provided by the National Library of Medicine Insight Segmentation and Registration Toolkit (ITK, Kitware Inc., New York, USA).

6.1.3.2 Fully Automatic Detection of Corresponding Anatomical Landmarks

In order to automatically detect corresponding anatomical landmarks, first the problem of how to get initial points in one volume, meaningful for the deformation performed, must be solved. The basic idea is that any subvolume with a high entropy will probably be a landmark of interest. To find those, the volume scan taken during exhalation is tessellated into cubes of same size, as demonstrated in Figure 6.8, typically 20 pixels x 20 pixels and the two neighboring slices in each direction, with respect to a pixel spacing of 0.9 mm x 0.9 mm x 10 mm. The size of these cubes is user defined and should be chosen depending on the nature of the landmarks to be detected. To detect landmarks in soft tissue for example smaller cubes should be used, because

of its very fine and deformable structures, like vessels, in contrast to the rigid character of bony structures.

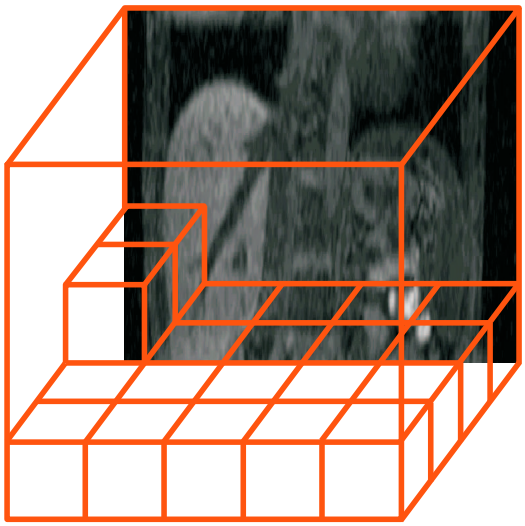

Figure 6.8: The volume is tessellated into cubes of same size. The entropy is computed for the image information of every cube, to find landmarks of interest.

Now the Shannon entropy of each cube is computed and the centers of mass of the cubes with the highest entropies are stored as control point candidates. The number of the control point candidates to be generated is user defined. The Shannon entropy H [Shannon 48] for an image is computed by the following equation, in which p_i represents the probability for the occurrence of a specific gray value.

$$H = -\sum_i p_i \log p_i \tag{6.11}$$

A volume, in this case a cube, consisting of many different intensities, which are mainly uniformly distributed, yields a high entropy value and therefore contains a lot of information. This property is very important for the later registration process of finding the exact position of the corresponding control point in the other CT volume.

To achieve an approximately uniform distribution of the control points within the volume, it is divided into 8 subvolumes of equal size. The resulting landmark search is performed in each of these regions separately.

Now there are several landmarks selected in the exhalation data set, but the corresponding anatomical landmarks in the inhalation data are still missing. Therefore, the two volume scans

of inhalation and exhalation are matched to each other by a global rigid registration procedure. The control points of the exhalation scan are also used for the inhalation scan, but are transformed by the registration pose and are taken as starting values for the subsequent local registration process.

Then the method for sharpening the control points, described in section 6.1.3.1 is applied to all the control point pairs. The surrounding cubes of the landmarks of the inhalation data are matched to larger surrounding cubes, with double width, height and depth, of the exhalation data (see Figure 6.9). This local rigid registration process is performed for every control point pair separately.

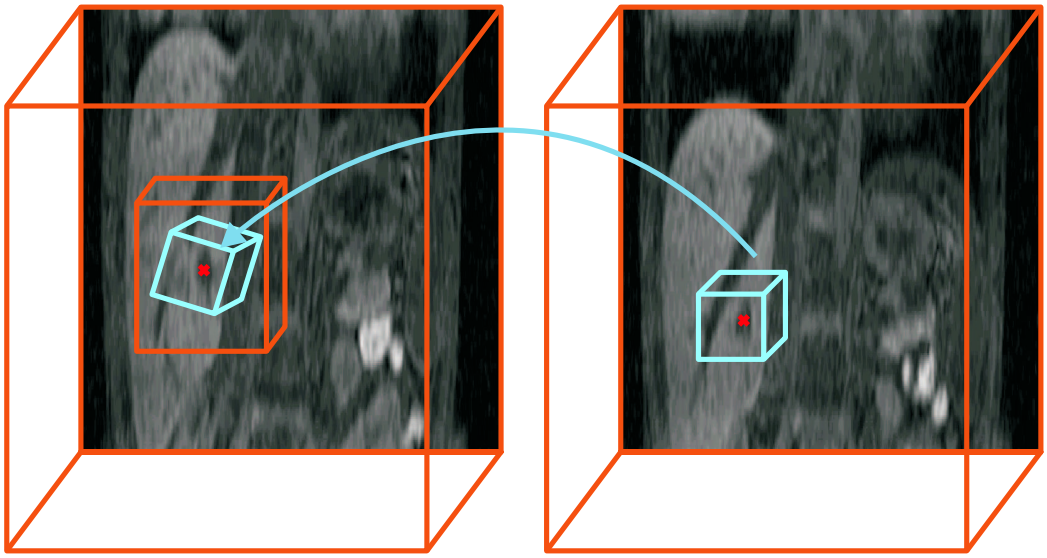

Figure 6.9: The surrounding cubes of the landmarks of the inhalation data are matched to larger surrounding cubes of the exhalation data. Thus, the position of the so far only roughly corresponding control point is refined.

Registration results, in which less than 20% of the voxels of the moving image were considered for computing the final metric value, are discarded. If the intersection of the moving and the fixed cube is too small, the resulting metric value certainly has no significance on registering these two. Sorting out these weak registration results enhances robustness, thus yielding very well matching final control point pairs.

These registration processes are performed in the 8 subvolumes to guarantee a uniform distribution. Without this distinction often most of the landmarks detected were located in the spine, whereas landmarks of the sternum, which are decisive for characterizing respiratory motion, were discarded. In each region, the fifteen points with the highest correlation coefficients are selected as final result, yielding a further enhancement in robustness.

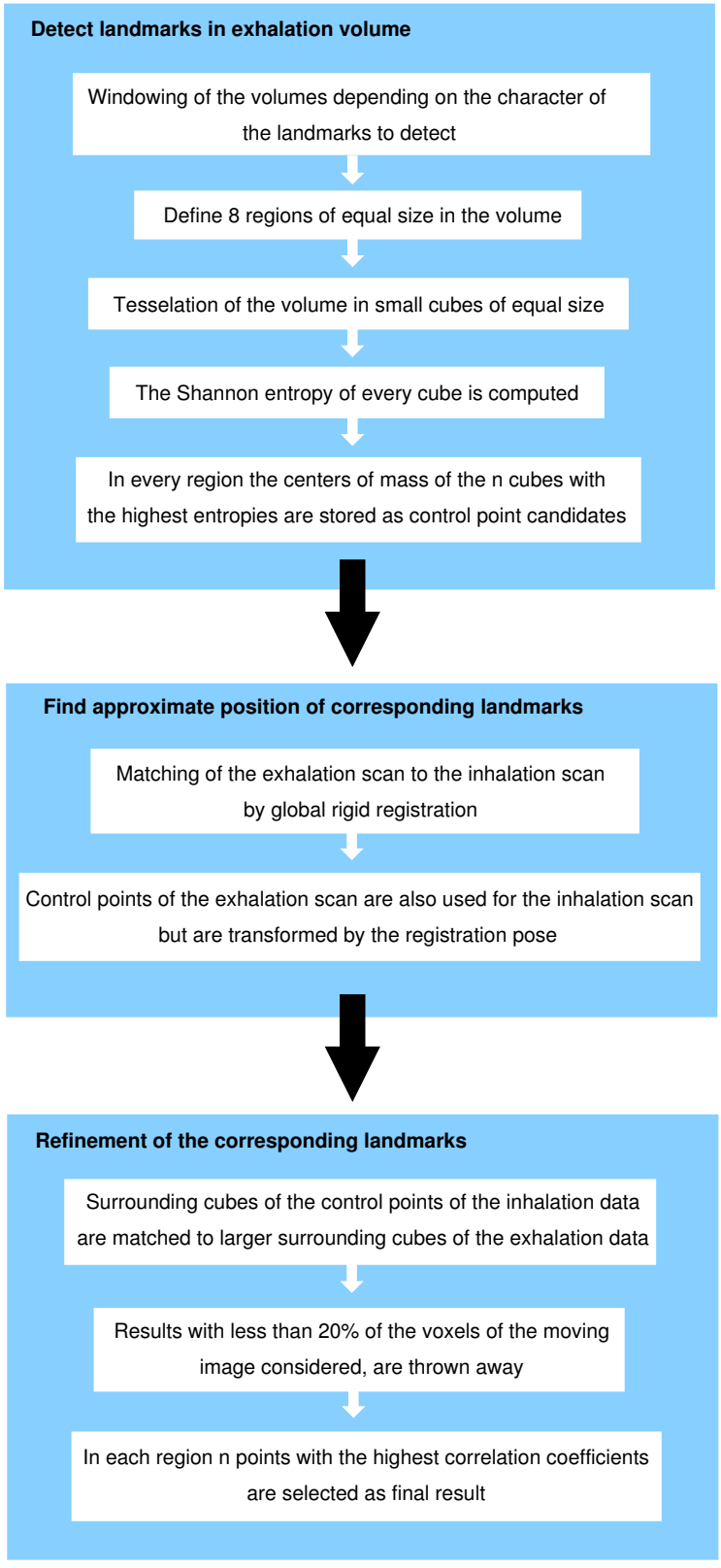

Figure 6.10: The automatic detection process of corresponding anatomical landmarks used for creating the 4D model by different interpolation techniques like thin-plate spline interpolation.

Depending on the desired character of the landmarks to be found by this method, Hounsfield windowing is performed on both volumes to emphasize their geometrical structure. For example, if bony structures are of interest, a typical center of the window would be 1200 and the corresponding width 600, whereas for soft tissue a window with center 200 and width 600 would be well suited. Figure 6.10 gives an overview of the process of fully automatically detecting corresponding anatomical landmarks.

6.2 Related Work

This section gives an overview of related methods for modeling deformation due to respiratory motion. They are discussed and compared to the novel method proposed for computing a 4D patient model in the résumé of this chapter.

6.2.1 Statistical Model [Blackall 02, Blackall 01]

A statistical model of respiratory motion and deformation of the liver was suggested by Blackall et al. A number of magnetic resonance scans of different breathing states were taken for 7 volunteers. The image, representing maximal exhalation, was chosen as the reference to which the images of the remaining respiratory phases were registered. The non-rigid registration algorithm of Rueckert et al. [Rueckert 98] was used to perform this matching.

Error in mm	Maximum Exhale	Shallow Exhale	Second Neutral	First Neutral	Shallow Inhale	Maximum Inhale
∅RMS	1.51	3.03	2.87	2.12	2.08	0.68
∅MAX	2.92	5.85	5.94	5.01	4.30	1.35

Table 6.1: The surfaces of the data, used to build the model, were compared to the surface nodes predicted by the model. This table contains the mean RMS (root mean square) and mean maximum errors [Blackall 02].

After visually inspecting the resulting non-rigid registrations, its free-form transformations were used to propagate landmarks, identified on the liver surface of the reference image, to the remaining images. Thus, corresponding surface landmarks were achieved, which were taken to form a Point Distribution Model (PDM). A PDM [Cootes 95] is built by statistically analyzing the change in shape of a number of training sets of the object to be modeled. Table 6.1 shows

the evaluation results achieved by comparison of the surfaces of the data used to build the model and the surface nodes predicted by the model.

6.2.2 Finite Element Analysis [Brock 02]

The approach of Brock et al. describes a method for creating a 4D model of the liver, by using finite element analysis, a numerical technique in engineering analysis. It was tested for one patient. Two CT scans, one at maximal exhalation, one at maximal inhalation, were taken using Active Breathing Control (see section 5.2.2.1). The liver was classified into six regions, used to determine an initial estimate of the deformation, occurring due to respiration. Linear, elastic and small deformations were considered within the mechanical model. As material properties, the elastic modulus and Poisson's ratio are required by the isotropic elastic model. The elastic modulus represents the force needed to elongate a specific material, defined by the ratio of stress to strain. Poisson's ratio describes the amount of possible compression, expressed by the ratio of lateral and axial strain. The surface data of the liver in state of exhalation, represented as a tetrahedral mesh, was imported into a finite element software tool. Each of the six regions of the liver was assigned specific material properties and an initial transformation, determined by the distance between inhalation and exhalation of the concerned region. The 4D model was obtained by computing several intermediate states, using the defined mechanical model.

6.2.3 Optimizing Positions of Corresponding Control Points [Coselmon 04]

Coselmon et al. also trust in thin-plate splines to create 4D models of the lung. For 11 patients they took one CT scan during normal inhalation and one during normal exhalation, both inspected by an expert to ensure the absence of artifacts caused by respiration. Tests were performed on the segmented right lobe of the lung. Thirty control points were placed manually in the exhalation data. For each of six slices in the transversal plane, uniformly distributed within the lung, five landmarks were selected. Each time, four points were placed on the contours of the lung and one in the interior. As initial starting point the landmarks of the exhalation data were also set to the inhalation data, but were shifted inferiorly and anteriorly subject to general breathing displacements. By use of the Nelder-Mead simplex algorithm the positions of the homologous points were optimized according to the match of the two data sets measured by mutual information. The arrangement of the corresponding points, which maximized mutual information, was chosen as the final one. They achieved alignment accuracies of 3.1 mm

in anterior-posterior, 3.6 mm in cranial-caudal and 1.7 mm in right-left direction. These values represent the standard deviations of the differences between predicted and real landmark positions at state of inhalation.

6.2.4 Demons Elastic Registration [Wang 05]

Wang et al. implemented an elastic registration algorithm, based on Thirion's Demons [Thirion 98], to enable targeted prostate cancer radiotherapy. The "Demons" algorithm iteratively minimizes the intensity difference of the two volumes, while the intensity gradient of the reference image determines the acting forces of deformation. To evaluate their method, three registration tests were performed. First they registered a pelvic CT scan to its mathematical deformed correspondent, yielding deviations of about 1 mm measured by comparison of the two displacement fields. Another test was to match CT scans of a deformable pelvic phantom, taken one time with an inflated balloon and one time with a deflated balloon to simulate different rectal states. A number of CT-opaque seeds were placed in the prostate to be able to compute the registration accuracy, which was about 1 mm. Finally two pelvic computed tomography scans of a patient were registered to each other. The correlation coefficient increased from 0.61 for the unregistered images to 0.944 for the registered images, with respect to a region of interest of 100 pixels x 110 pixels x 30 slices.

6.2.5 B-spline Interpolation [Rohlfing 01]

Rohlfing et al. used intensity-based free-form registration of gated MR images to model the deformation of the liver. They took MR scans of four test persons at end-inhalation, end-exhalation and at eight intermediate respiratory phases using respiratory gating. Image data was deformed by using B-spline interpolation between uniformly placed control points. By a linesearch algorithm and mutual information as similarity measure the best transformation parameters were determined. Registration results were evaluated by visual inspection using checkerboard fusion and isointensity contour overlays.

6.3 Results

The new methods, introduced in this thesis, to compute synthetic 4D models based on two input scans were tested on several CT and MR volume scans. Each time, both methods, using

thin-plate splines and the barycentric coordinates respectively, have been applied to the scans and the results were compared to each other. Except for patient 6, the MR scan of the liver, the deformations were always performed from exhalation to inhalation. It was decided to compute models consisting of 6 respiratory states, representing a frequently used classification. For evaluation the following tests were carried out:

1. The distances between the triangulated surfaces of the segmented target organ of the real and the synthetic inhalation scan were computed. The synthetic inhalation scan certainly is the scan of the volumetric deformation model representing state of inhalation.

2. Checkerboards were generated, showing the results of the elastic registration of exhalation and inhalation scan. Checkerboards demonstrate the accuracy of deformations/registrations performed by alternately displaying information of the two images in small squares of equal size.

3. The corresponding slices of the exhalation and the inhalation scan were compared to each other (unregistered) as well as the slices of the synthetic inhalation scan (last stack of the 4D model) and the real inhalation scan (registered). As the 4D patient model is computed by deforming the exhalation scan with respect to landmark correspondences to the inhalation scan, this process is often referred in the text as an elastic registration. These results were visualized in graphs, showing the increase in correlation coefficient for every slice.

4. In some cases additional information about intermediate respiratory states, acquired by the methods described in chapter 5, was available:

    a) Concerning a complete scan of one particular respiratory state, this scan was compared to the computed 4D model, using mutual information and correlation coefficient as similarity measures, to get the approximate state of respiration of this volume within the 4D model. The real respiratory state should certainly match that within the 4D model.

    b) If additional scans were taken during free breathing, the slices with known respiratory state were compared to the corresponding slices of all stacks of the 4D model. The best match is expected at the appropriate breathing phase.

In the next sections the evaluations of deformations performed on 5 computed tomography volumes of the lung and 1 magnetic resonance volume of the liver are presented.

6.3.1 Patient 1

For the first patient the different evaluation techniques are described in detail. For the remaining tests, only differences in evaluation procedure are commented at length. Every evaluation data is discussed in a final summary. The results are presented for every patient as follows:

1. The properties of the underlying image data are presented.
2. The method for landmark detection and its parameters are specified in detail.
3. Then different evaluations of the performed deformation follow.
    a) The surface distance measurements of the triangulated surfaces of the region of interest.
    b) Further evaluation on the complete information of the image by checkerboards and correlation coefficient measurements of corresponding slices.
4. Finally the results of the specific data set are summarized.

6.3.1.1 Input Data

The specifications of the data used to compute the 4D model are listed in this section.

Target organ	Lung
Modality	CT
Dimension (x, y, z)	512 x 512 x 25
Pixelspacing im mm (x, y, z)	0.938 x 0.938 x 10
Intermediate images	Images labeled with respiratory state by opt. tracking (5.1.1)

Table 6.2: Information about the image data of patient 1.

Target organ: The region of interest, the affected organ.

Modality: The underlying imaging technique.

Dimension: The dimension of the image given in voxels.

Pixelspacing: The size of a voxel in mm.

Intermediate images: Are intermediate images available for this patient? What sort of images (breath-hold or free breathing)?

6.3.1.2 Detection of Corresponding Anatomical Landmarks

In this section the different parameters for landmark detection are specified. Also listed are the numbers of detected control point pairs and the number of control points, which had to be removed or added manually. These decisions were made by visual inspection, as demonstrated in Figure 6.7.

	Boney structure	Soft tissue
Hounsfield window config. (center/width)	1200/600	200/600
Landmarking method	Full automatic detection (see section 6.1.3.2)	
Cube size landmark detection (x, y, z)	20 x 20 x 5	10 x 10 x 5
Number of regions	8	
Number of candidates	400	
Cube size moving image (x, y, z)	54 x 54 x 5	
Cube size fixed image (x, y, z)	108 x 108 x 10	118 x 118 x 12
Considered voxels required	20%	15%
Number of detected control point pairs	80	29
Number of points manually removed	0	1
Number of points manually added	0	0

Table 6.3: The parameters for the landmarks detection of patient 1.

Hounsfield window config. (center/width): The window configurations applied to the Hounsfield data of the images. The used scale ranges from 0 to 4095.

Landmarking method: The method applied to detect corresponding anatomical landmarks (see 6.1.3).

Cube size landmark detection: Defines the size of the cubes for detecting landmark candidates. The entropy of every cube is computed and the n centers of mass of the cubes with the highest entropies are selected as candidates.

Number of regions: The volume can be divided in 8 regions of equal size to reach an uniformal distribution of the control point candidates and the final control point pairs as well.

Number of candidates: The number of control point candidates to be generated.

Cube size moving image: The size of the moving cube used for refining the so far only roughly corresponding control point pairs (see Figure 6.9).

Cube size fixed image: The size of the fixed cube used for refining the so far only roughly corresponding control point pairs.

Considered voxels required: The minimal percentage of voxels, considered for computing the final similarity measure, required for acceptance as final control point pair.

Number of detected control point pairs: The number of final control point pairs remaining after refinement.

Number of points manually removed: The number of corresponding control points, which had to be removed manually after visual inspection.

Number of points manually added: The number of corresponding control points, which had to be added manually, because not enough points were automatically detected in a specific region.

6.3.1.3 Surface Distance Measurements

To evaluate the accuracy of the predicted deformation the region of interest undergoes during respiration, the lung was segmented in the exhalation scan, the inhalation scan, and the synthetic inhalation scan. After that, triangulated surfaces, consisting of about 18000 faces, were created to be able to compute the surface distances, from lung exhaled to lung inhaled (unregistered) and from the lung inhaled (of the 4D model, i.e. synthetic) to lung inhaled (registered). The terms 'unregistered' and 'registered' are used, because the 4D patient model is computed by deforming the exhalation scan with respect to landmark correspondences to the inhalation scan. Therefore, this process can be regarded as an elastic registration. For segmentation and surface creation the isosurface of the image data was computed with a threshold value of -180. Remaining information not belonging to lung and trachea was removed manually. Vessels inside the lung were not removed, and thus yielded the occurring outliers, when calculating the distance measurements. The surface distances were computed by determining for each vertex of a triangle the closest point on the other triangle. In Figure 6.11 the result of the deformation by using thin-plate splines is visualized by the segmented lung colored from red to green, depending on the underlying surface distance. Figure 6.12 shows a more detailed view, which allows outliers to be localized. Table 6.4 contains the surface distance measurements for the unregistered case and the deformations by using the barycentric coordinates based and the thin-plate spline based method. The segmentations and distance measurements were performed using the AMIRA (Mercury Computer Systems, Chelmsford, USA) software package.

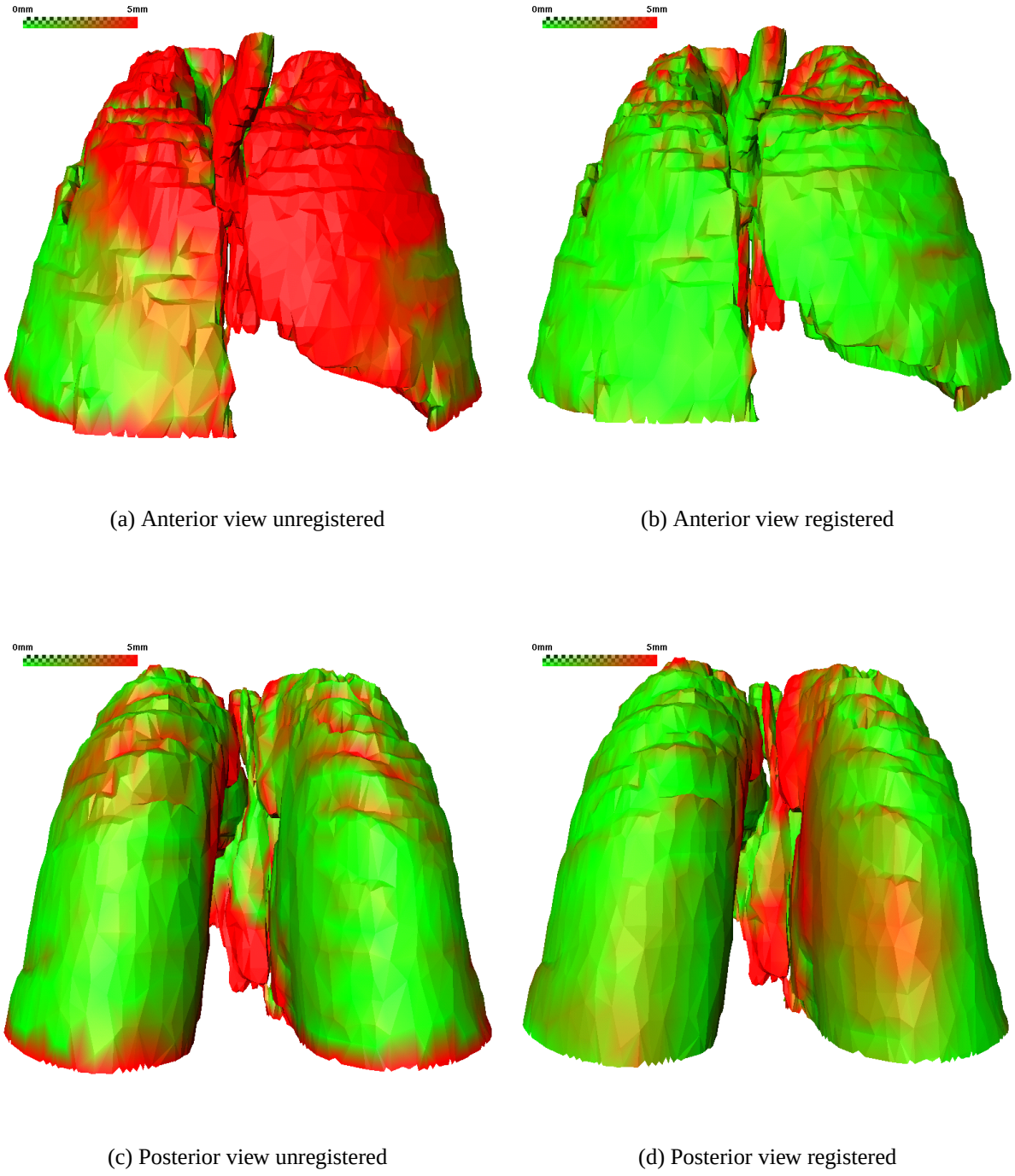

(a) Anterior view unregistered

(b) Anterior view registered

(c) Posterior view unregistered

(d) Posterior view registered

Figure 6.11: The segmented lung, colored from red to green, depending on the underlying surface distance. Red means a distance of 5 mm or more, green means no deviation. Beside this very good result obtained using thin-plate splines, it is interesting to see that the lung deforms mainly in the anterior region due to respiration. As can be seen, the trachea was also included in the computation of the surface distance.

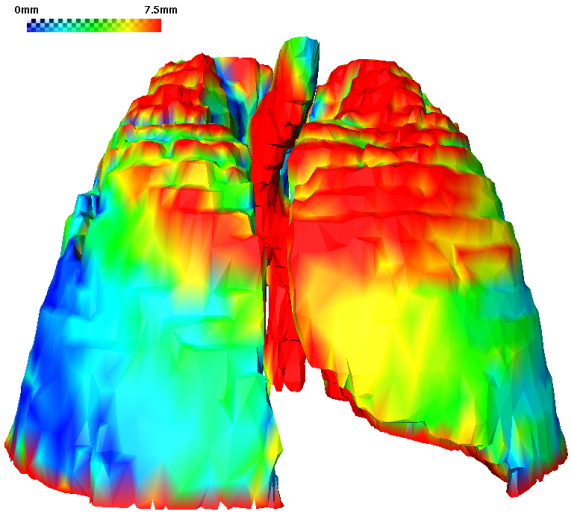

(a) Anterior view unregistered

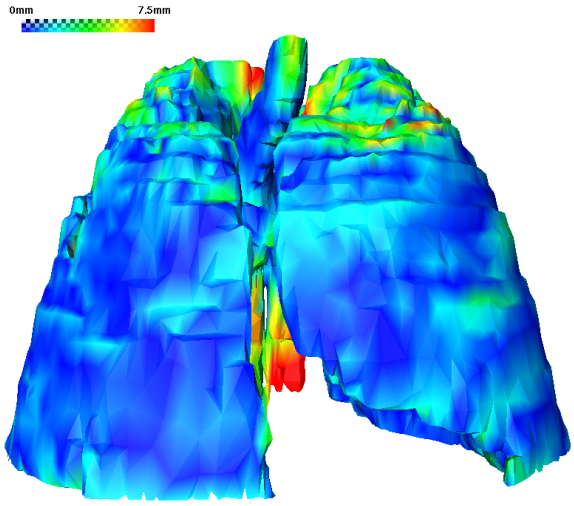

(b) Anterior view registered

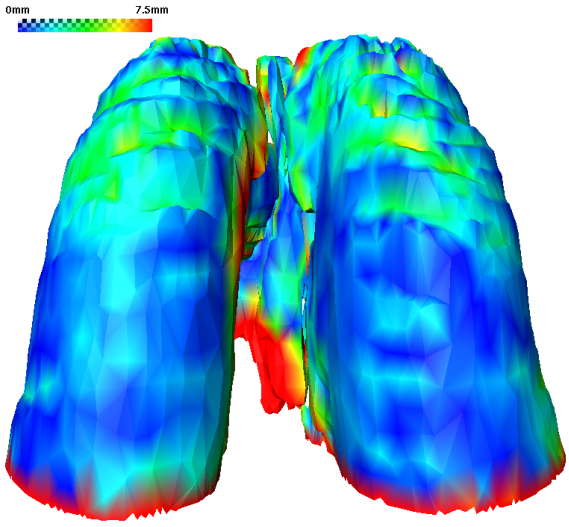

(c) Posterior view unregistered

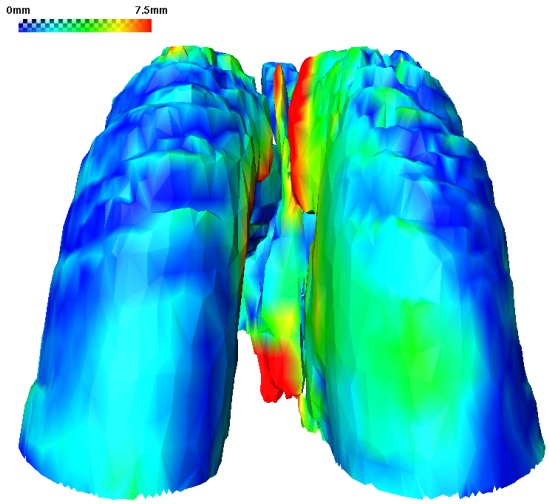

(d) Posterior view registered

Figure 6.12: A more detailed view to be able to localize occurring outliers. On the left the 'unregistered' lung is visualized in anterior and posterior view, demonstrating the deformation occurring due to respiration with respect to this patient. On the right the very good result of the deformation performed using thin-plate splines is presented.

[mm]	Mean dist.,	stand.dev.	rms	max	> 5 mm	> 7.5 mm	> 10 mm
Unregistered	4.922	4.076	6.390	24.472	40.733%	25.199%	12.732%
Registered bc	2.115	2.132	3.003	23.227	8.550%	2.868%	0.982%
Registered tps	1.877	1.931	2.693	21.518	5.914%	2.019%	0.772%

Table 6.4: The resulting surface distances. The figures from left to right represent the mean distance, the standard deviation, the root mean square and the maximum distance, followed by rates of outliers passing 5 mm, 7.5 mm and 10 mm of distance. 'BC' stands for barycentric coordinates and 'TPS' for thin-plate splines.

6.3.1.4 Evaluation on the Complete Image Information

Comparison with Reference Image

For evaluation in this section first a graph is presented, which demonstrates the increase in correlation coefficient for every single slice after the performed elastic registration (Figure 6.13).

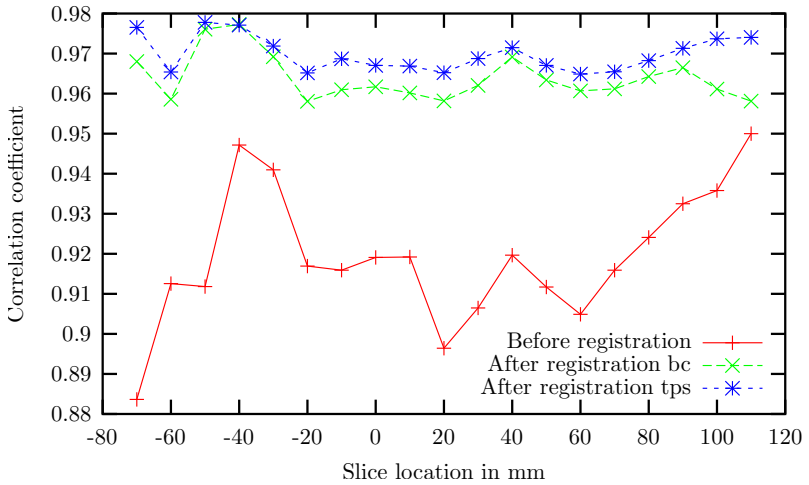

Figure 6.13: The corresponding slices of the exhalation and the inhalation scan are compared to each other (unregistered) as well as the slices of the synthetic inhalation scan and the real inhalation scan (registered). This graph visualizes the increase in correlation coefficient for every slice location.

The treatment table was masked out for calculating the correlation coefficients of the 12 bit image information of the corresponding slices. Furthermore the checkerboards of Figure 6.14 emphasize the very good registration result. Even the vessels match very accurately, as can be seen in the image windowed for soft tissue.

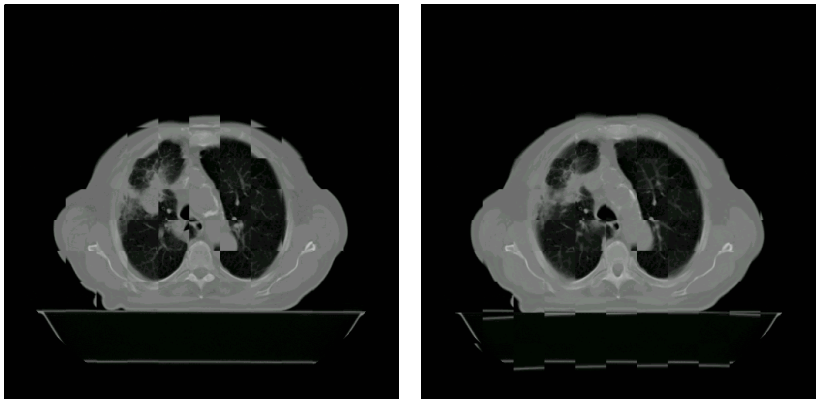

(a) Unregistered 2048/4096 (b) Registered 2048/4096

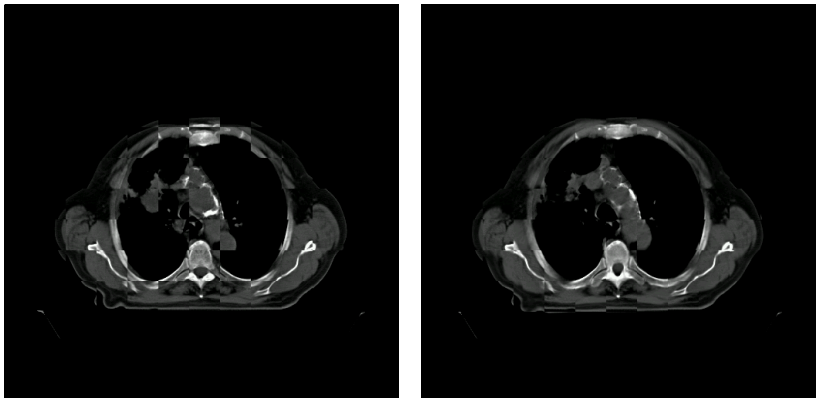

(c) Unregistered 1200/600 (d) Registered 1200/600

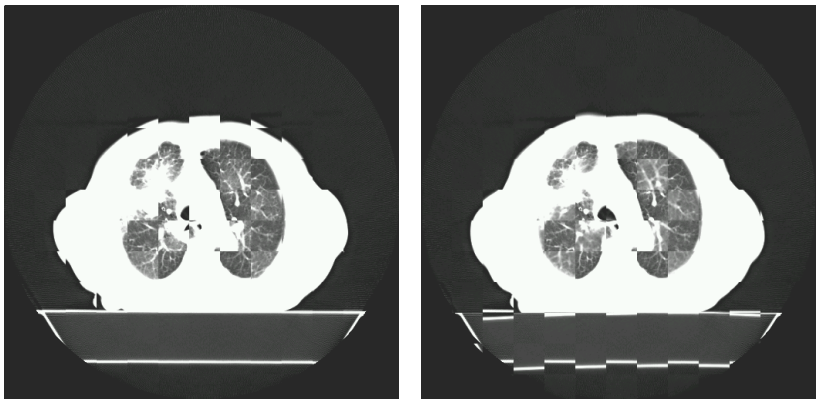

(e) Unregistered 200/600 (f) Registered 200/600

Figure 6.14: Checkerboards unregistered and registered for three different Hounsfield window specifications, complete information, hard tissue and soft tissue, demonstrate the registration result here. The examined slice is located at position 50 (see the graph in Figure 6.13), displaying the correlation coefficients for each slice location.

Comparison with Intermediate Images

In Figure 6.15 the result of the assignment of respiratory states to images taken during free breathing is visualized. In this case the images were labeled with respiratory states by the use of optical tracking, as described in section 5.1.1. The computed 4D model with which the acquired intermediate images were compared, consisted of 12 stacks, that is 12 respiratory states. The reason for calculating 12 instead of 6 stacks is the fact, that the respiratory curve never reaches the amplitude of a breath-hold during inhalation. Thus, more stacks are needed to enable comparison.

Checkerboards at different slice locations emphasize the high accuracy of the model, as can be seen in Figure 6.16. The method for assigning CT images to respiratory states by the use of optical tracking did not gain acceptance in daily clinical use, because of its too complicated setup. Furthermore, the calibration of the system (section 5.1.1) has to be improved to achieve a higher accuracy. However, with respect to this patient intermediate images could be acquired successfully by using this method.

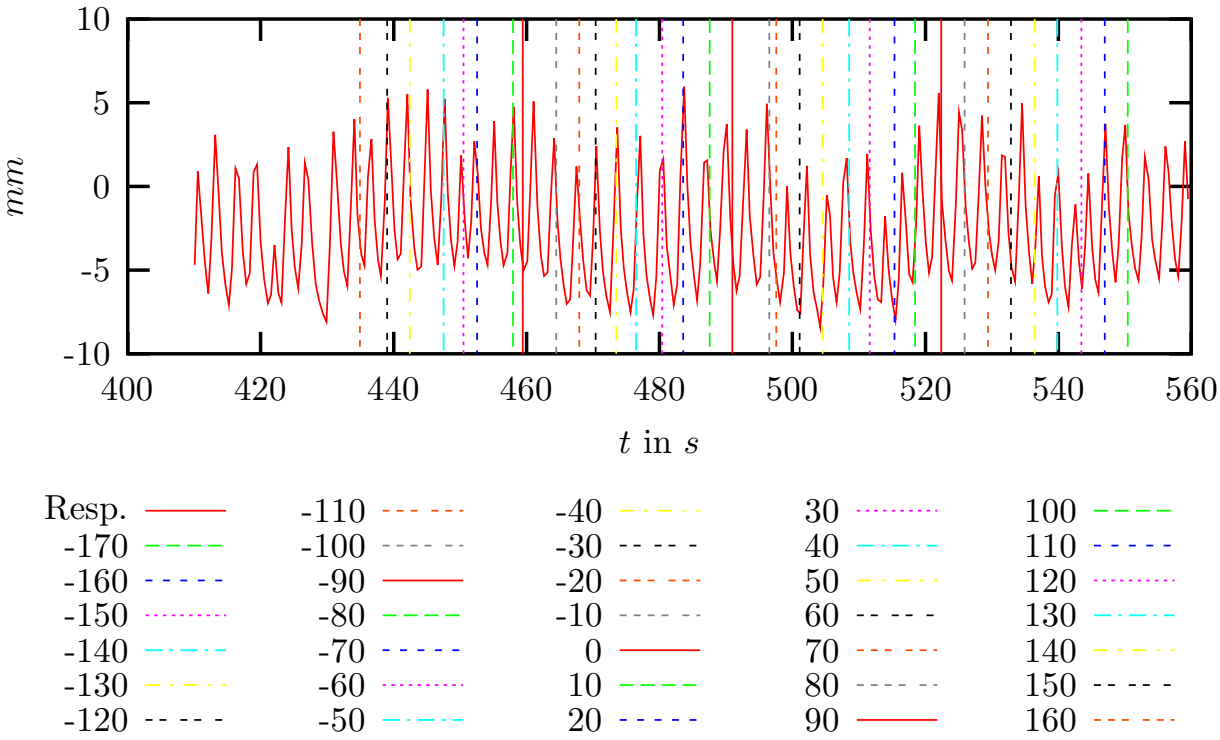

Figure 6.15: The final result, assigning respiratory states to every single slice. Each vertical line represents a particular slice. The red curve represents the respiratory curve, gained by observing infrared emitters attached to the patient's chest by a tracking camera. The intersection of a vertical line and the respiratory curve yields the corresponding breathing phase.

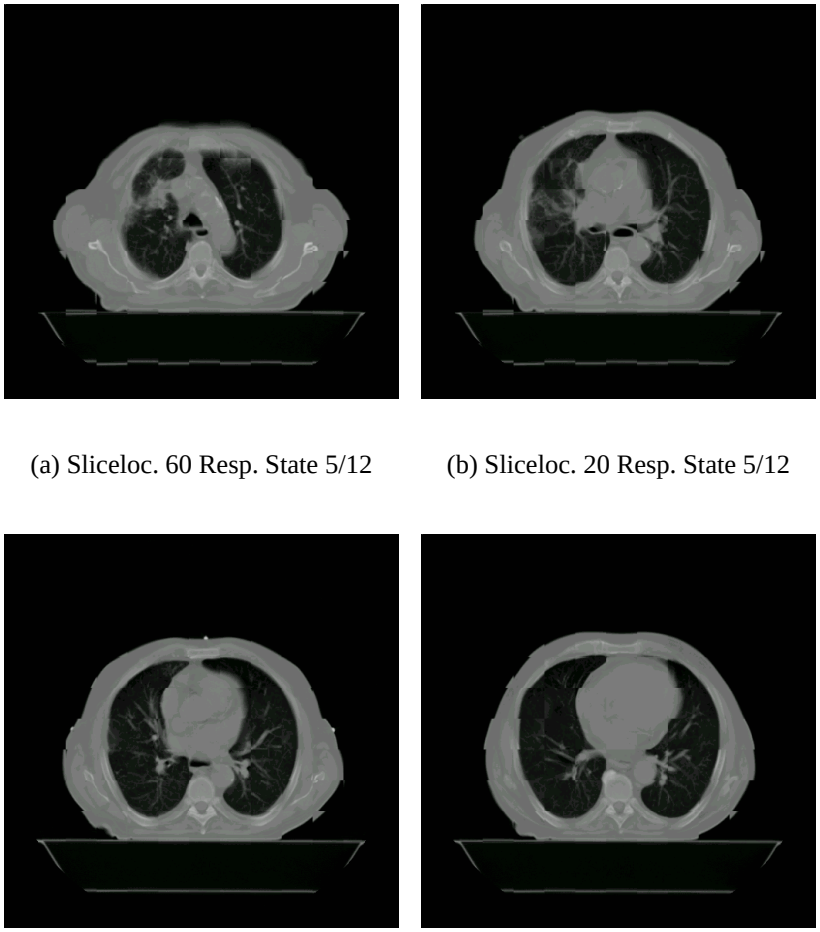

(a) Sliceloc. 60 Resp. State 5/12 (b) Sliceloc. 20 Resp. State 5/12

(c) Sliceloc. 0 Resp. State 1/12 (d) Sliceloc. -30 Resp. State 1/12

Figure 6.16: Some checkerboards taken at different slice locations demonstrating the accuracy of the model. Respiratory state 1 represents state of exhalation. The images show the best matches within the 4D model. Compare the obtained breathing phases to the graph in Figure 6.15.

6.3.1.5 Summary

The deformation of the image data, due to movements of respiration, worked very well using the new methods. Only one of the fully automatically detected corresponding anatomical landmarks, in case of soft tissue, had to be removed manually. Furthermore, no additional control points had to be added manually. The comparison of the segmented surfaces led to a mean distance of only 1.8 mm using thin-plate splines (Table 6.4) and even the very fine structures in soft tissue like vessels and bronchial tubes match very accurate, as can be seen in Figure 6.14.

6.3.2 Patient 2

Noteworthy about this volume data is, that the lung of the patient consists of only one lobe. A huge part of the left lobe has been surgically removed. Further information about this patient data is given in Table 6.5.

6.3.2.1 Input Data

Target organ	Lung
Modality	CT
Dimension (x, y, z)	512 x 512 x 30
Pixelspacing im mm (x, y, z)	0.938 x 0.938 x 10
Intermediate images	n. a.

Table 6.5: Information about the image data of patient 2.

6.3.2.2 Detection of Corresponding Anatomical Landmarks

	Boney structure	Soft tissue
Hounsfield window config. (center/width)	1200/600	200/600
Landmarking method	Full automatic detection (6.1.3.2)	
Cube size landmark detection (x, y, z)	20 x 20 x 5	10 x 10 x 5
Number of regions	8	
Number of candidates	400	323*
Cube size moving image (x, y, z)	54 x 54 x 5	
Cube size fixed image (x, y, z)	108 x 108 x 10	118 x 118 x 12
Considered voxels required	20%	15%
Number of detected control point pairs	95	34
Number of points manually removed	2	0
Number of points manually added	5$^{\diamond}$	0

Table 6.6: 77 candidates ($\star$) were removed before refinement, because the detected landmarks were located on the treatment table and therefore had to be sorted out. 5 additional hard tissue landmarks ($\diamond$) had to be manually selected. Possible reason is the slice distance of 10 mm. With smaller distances it would have been easier to detect the corresponding landmarks.

6.3.2.3 Surface Distance Measurements

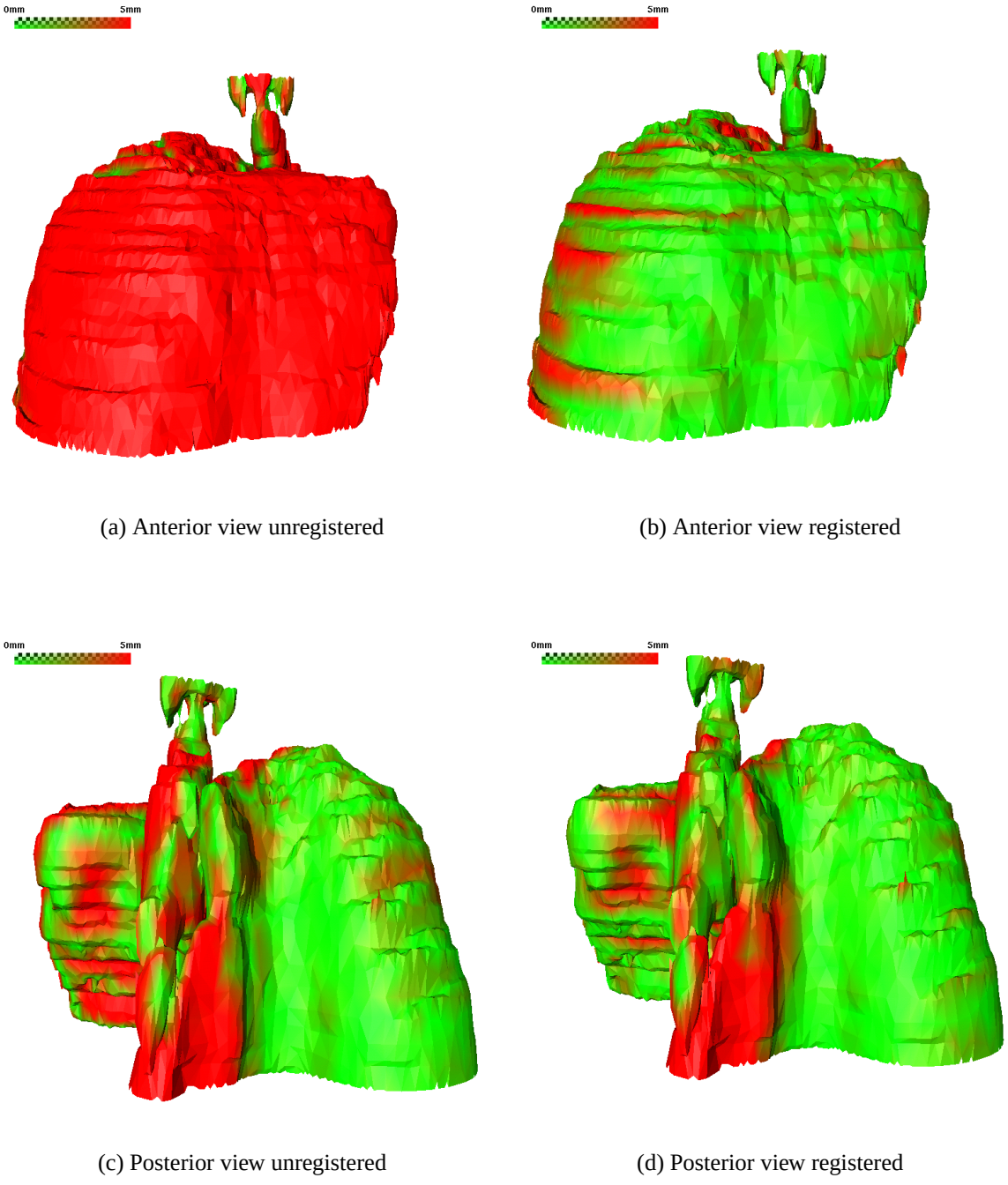

(a) Anterior view unregistered

(b) Anterior view registered

(c) Posterior view unregistered

(d) Posterior view registered

Figure 6.17: The lung 'unregistered' is shown on the left, demonstrating the deformation occurring due to respiration with respect to this patient. On the right the very good match after the deformation, performed using thin-plate splines, is presented.

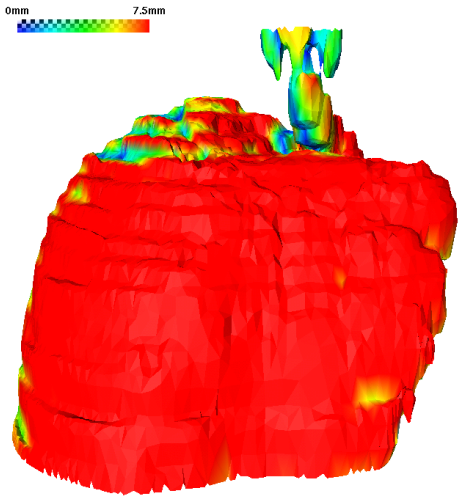

(a) Anterior view unregistered

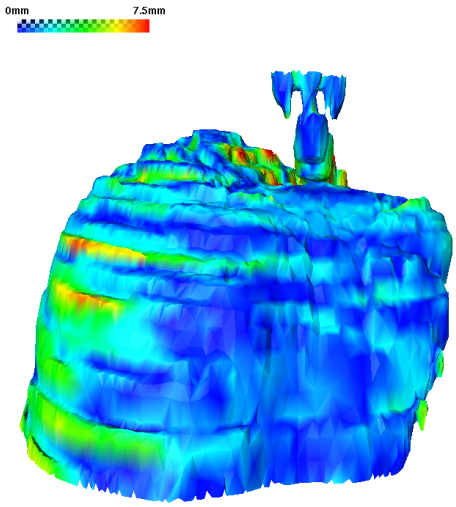

(b) Anterior view registered

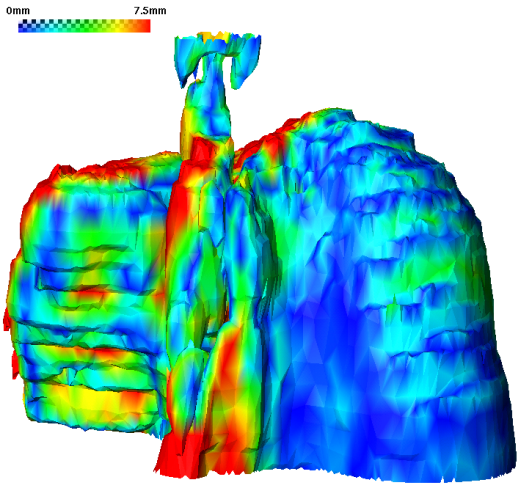

(c) Posterior view unregistered

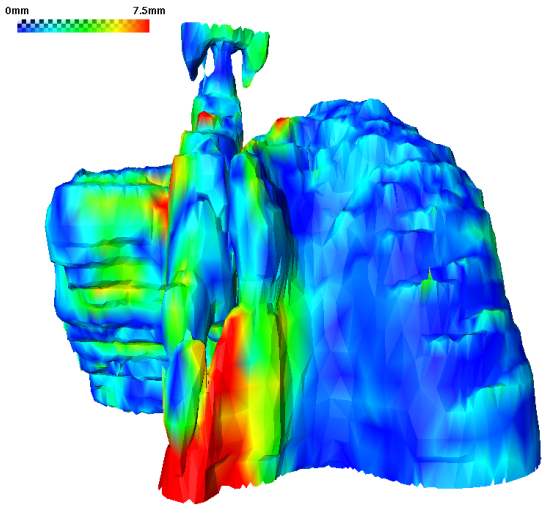

(d) Posterior view registered

Figure 6.18: The more detailed view of the deformation performed using thin-plate splines. These figures point out the outliers, which probably occur because of too few corresponding anatomical landmarks detected in the specific region. The lung of this patient consists only of one lobe. The larynx was also included in the computation of the surface distances.

[mm]	Mean dist.,	stand.dev.	rms	max	> 5 mm	> 7.5 mm	> 10 mm
Unregistered	5.503	4.019	6.814	23.202	49.784%	32.938%	16.436%
Registered bc	2.625	2.641	3.723	18.516	15.881%	5.604%	1.931%
Registered tps	2.120	2.240	3.084	20.749	9.588%	3.285%	1.110%

Table 6.7: With a mean deviation of 2.120 mm the best result was obtained by using thin-plate splines.

6.3.2.4 Evaluation on the Complete Image Information

The graph in Figure 6.19 demonstrates the increase in correlation coefficient with respect to the comparison of corresponding slices. In Figure 6.20 checkerboards illustrate the success of the deformation performed using thin-plate splines.

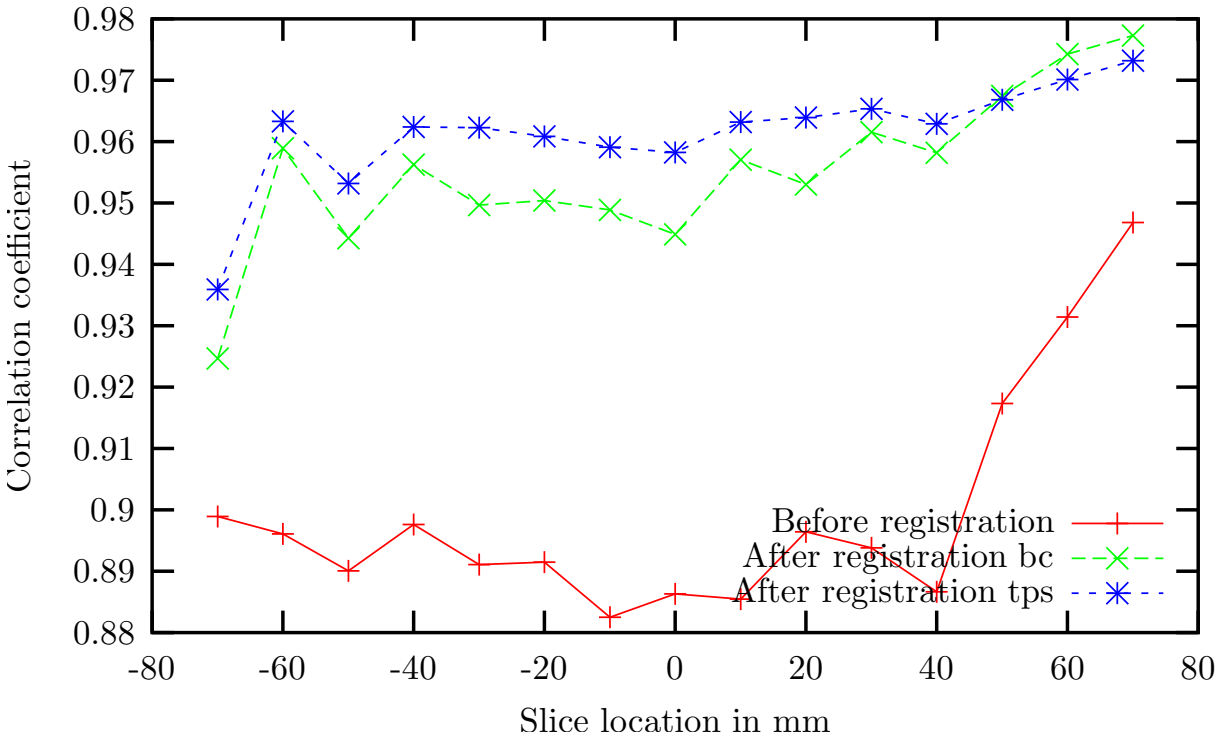

Figure 6.19: The corresponding slices of the exhalation and the inhalation scan are compared to each other (unregistered) as well as the slices of the synthetic inhalation scan (last slice of the 4D model) and the real inhalation scan (registered). This graph visualizes the increase in correlation coefficient for every slice location.

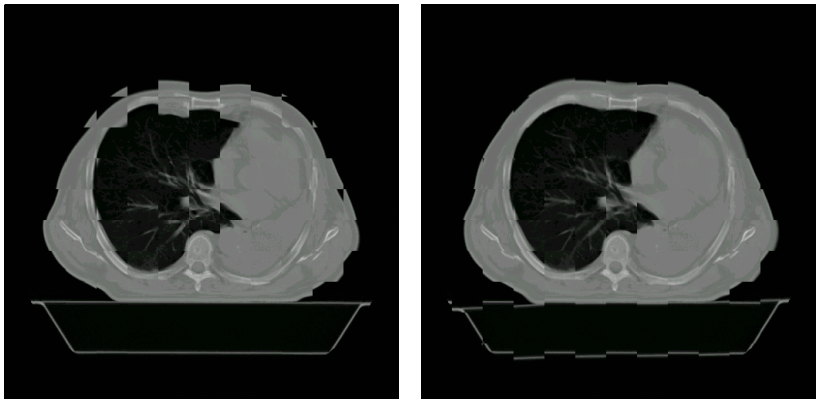

(a) Unregistered 2048/4096 (b) Registered 2048/4096

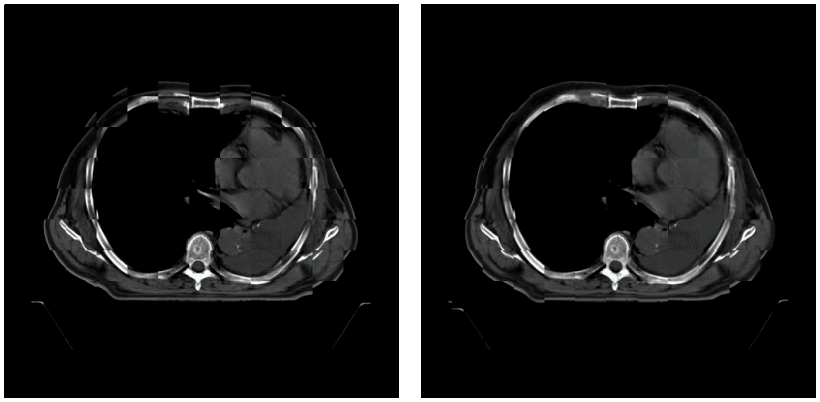

(c) Unregistered 1200/600 (d) Registered 1200/600

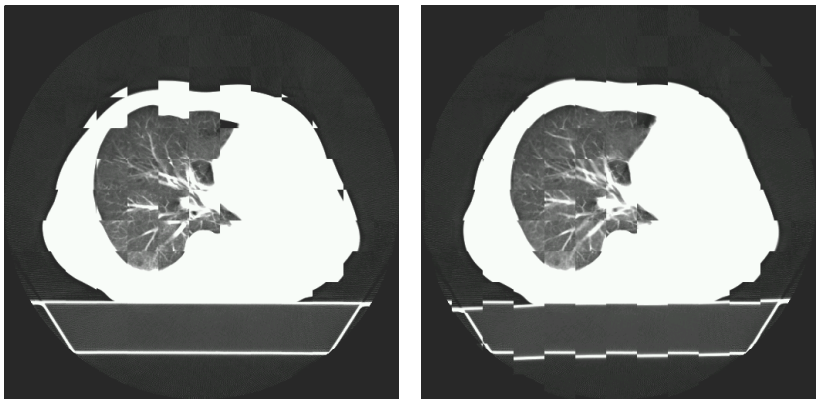

(e) Unregistered 200/600 (f) Registered 200/600

Figure 6.20: The checkerboards unregistered and registered for three different Hounsfield window specifications. The examined slice is located at position -40 (also refer to the graph shown in Figure 6.19).

6.3.2.5 Summary

As demonstrated in Figure 6.17 the lung of this patient consisted of only one lobe. Nevertheless, the extent of deformation caused by respiration with respect to the lung amounted to 5.5 mm. Some of the automatically determined control point candidates in soft tissue were located on the treatment table and therefore had to be removed before starting the refinement. With using thin-plate splines, the best result of the elastic registration could be achieved, as demonstrated in Figures 6.17, 6.18 and in Table 6.7. The mean surface distance could be significantly reduced from 5.5 to 2.1 mm. The graph in Figure 6.19 shows the large increase in similarity for each of the corresponding slices and the checkerboards of Figure 6.20 emphasize the very accurate registration result.

6.3.3 Patient 3

This data set also belongs to a lung cancer patient. Table 6.8 lists further information about the image data and in Table 6.9 the parameters used for the fully automatic corresponding landmark detection are specified.

6.3.3.1 Input Data

Target organ	Lung
Modality	CT
Dimension (x, y, z)	512 x 512 x 24
Pixelspacing im mm (x, y, z)	0.82 x 0.82 x 10
Intermediate images	n. a.

Table 6.8: Information about the image data of patient 2.

6.3.3.2 Detection of Corresponding Anatomical Landmarks

	Boney structure	Soft tissue
Hounsfield window config. (center/width)	1200/600	200/600
Landmarking method	Full automatic detection (6.1.3.2)	
Cube size landmark detection (x, y, z)	20 x 20 x 5	10 x 10 x 5
Number of regions	8	
Number of candidates	400	400
Cube size moving image (x, y, z)	54 x 54 x 5	
Cube size fixed image (x, y, z)	108 x 108 x 10	118 x 118 x 12
Considered voxels required	20%	15%
Number of detected control point pairs	56	22
Number of points manually removed	0	4
Number of points manually added	$5^{\diamond}$	4

Table 6.9: 5 additional hard tissue landmarks ($\diamond$) had to be manually selected. Probably the reason again is the too large slice distance of 10 mm, complicating the detection of corresponding landmarks.

6.3.3.3 Surface Distance Measurements

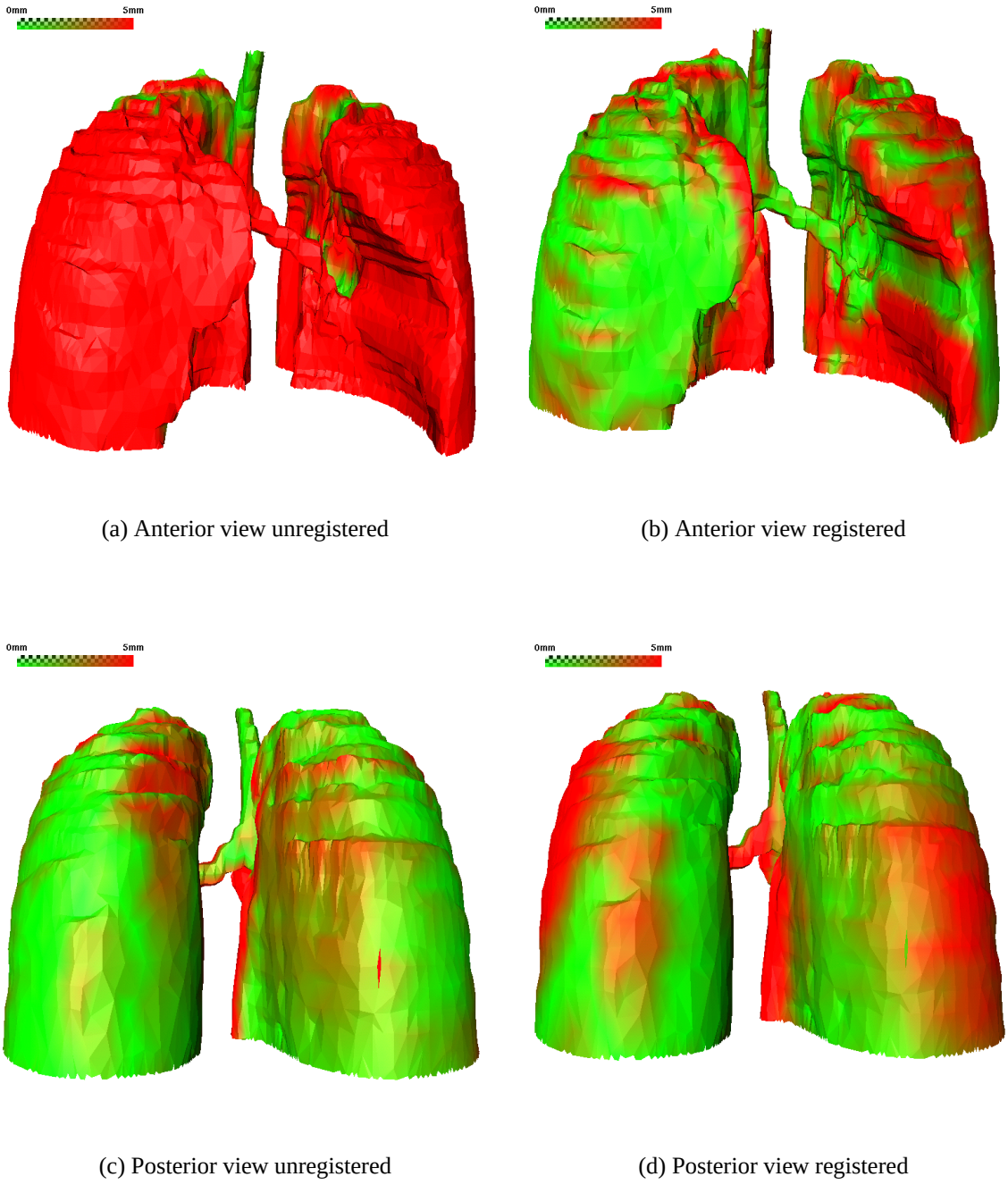

(a) Anterior view unregistered

(b) Anterior view registered

(c) Posterior view unregistered

(d) Posterior view registered

Figure 6.21: The lung 'unregistered' is shown on the left, demonstrating the occurring deformation due to respiration. In some regions not enough corresponding control point pairs were detected and thus still appear unregistered. A more detailed view emphasizing the great improvement is visualized in Figure 6.22.

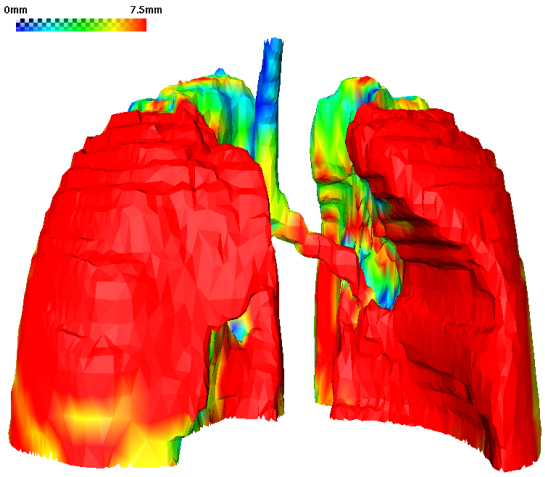

(a) Anterior view unregistered

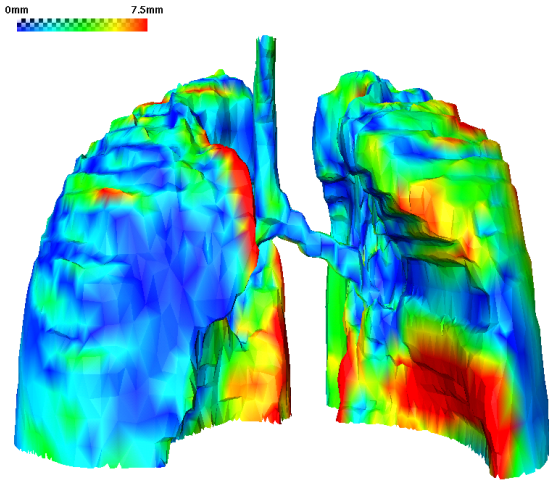

(b) Anterior view registered

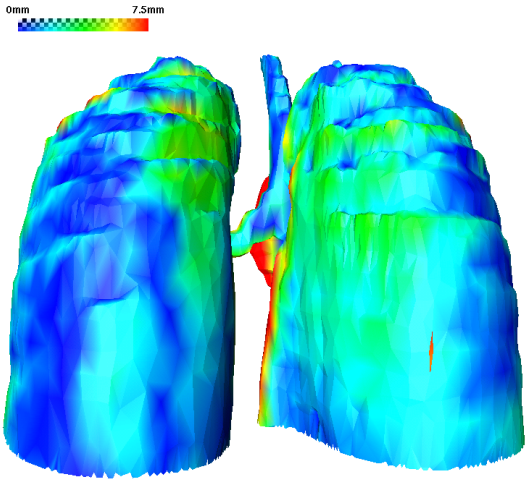

(c) Posterior view unregistered

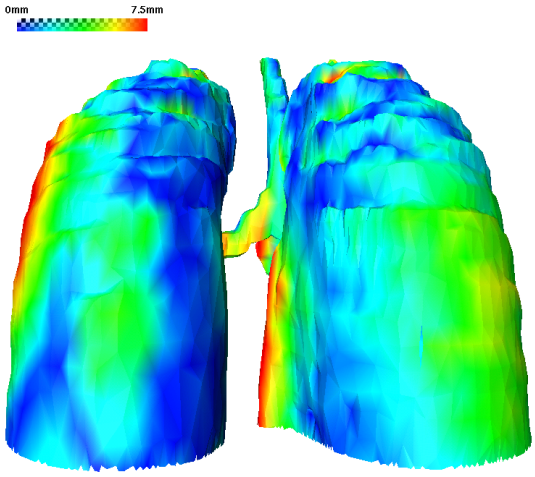

(d) Posterior view registered

Figure 6.22: This more detailed view demonstrates the high accuracy of the computed volumetric deformation model and shows the remaining outliers. The volumetric deformation model was computed using thin-plate splines.

[mm]	Mean dist.,	stand.dev.	rms	max	> 5 mm	> 7.5 mm	> 10 mm
Unregistered	6.261	5.224	8.154	25.708	47.873%	34.332%	26.097%
Registered bc	2.929	3.103	4.267	31.231	15.256%	6.726%	3.303%
Registered tps	2.894	2.621	3.904	26.591	16.351%	5.720%	2.023%

Table 6.10: Using thin-plate splines, the surface deviation could be reduced from 6.261 mm to 2.894 mm.

6.3.3.4 Evaluation on the Complete Image Information

The increase in correlation coefficient with respect to the comparison of corresponding slices is demonstrated in the graph displayed in Figure 6.23. Checkerboards in Figure 6.24 illustrate the success of the deformation performed using thin-plate splines for one specific slice location.

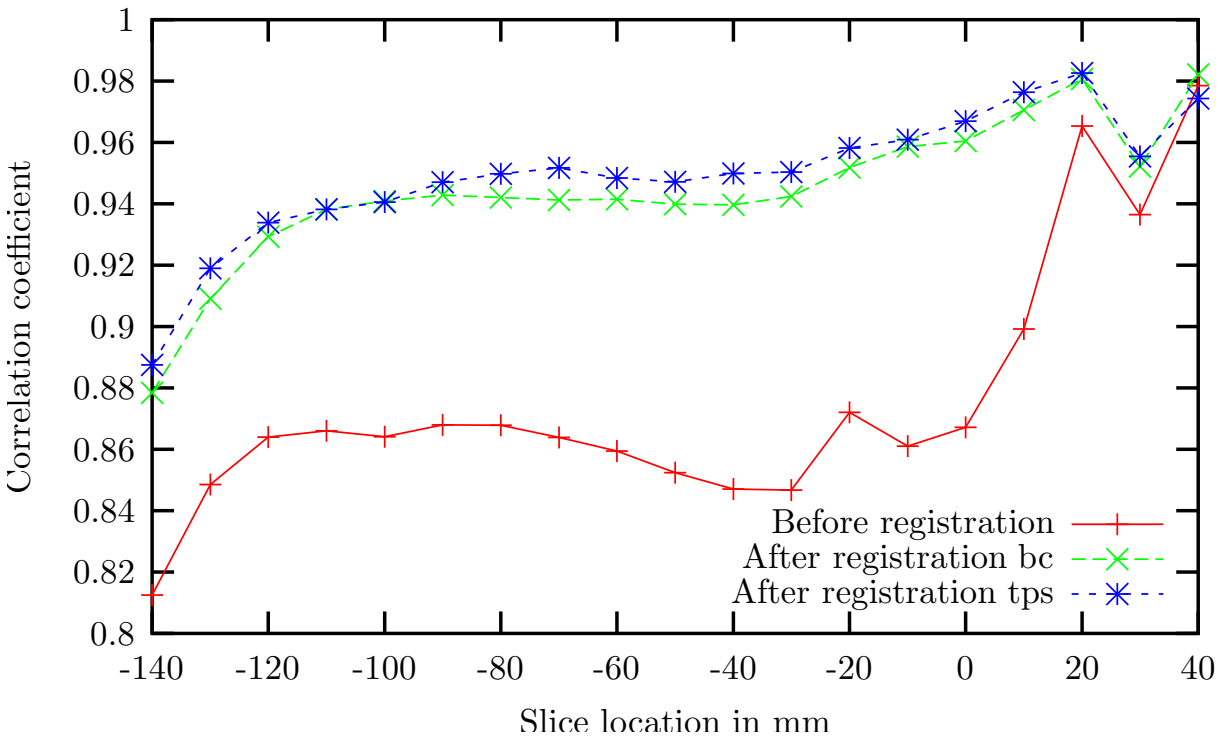

Figure 6.23: The visualization of the increase in correlation coefficient for every single slice. The images of slice locations 20, 30 and 40 are located cranial of the lung. Thus, these regions are less affected by respiratory motion.

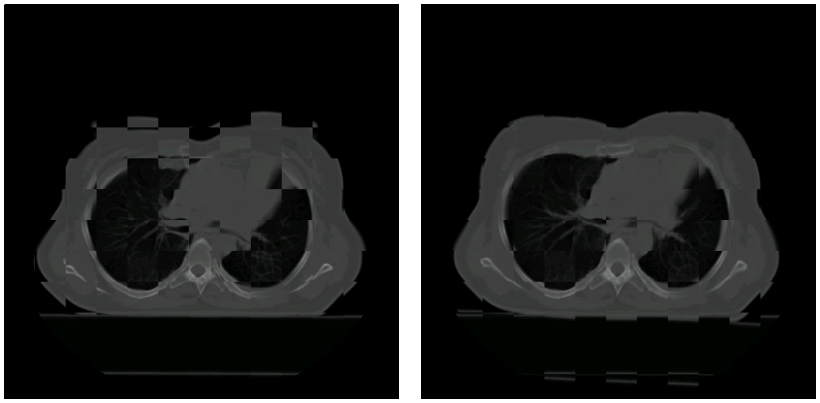

(a) Unregistered 2048/4096 (b) Registered 2048/4096

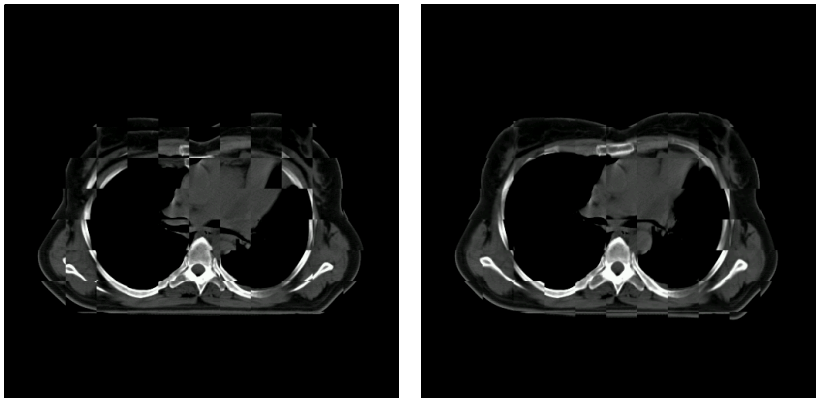

(c) Unregistered 1200/600 (d) Registered 1200/600

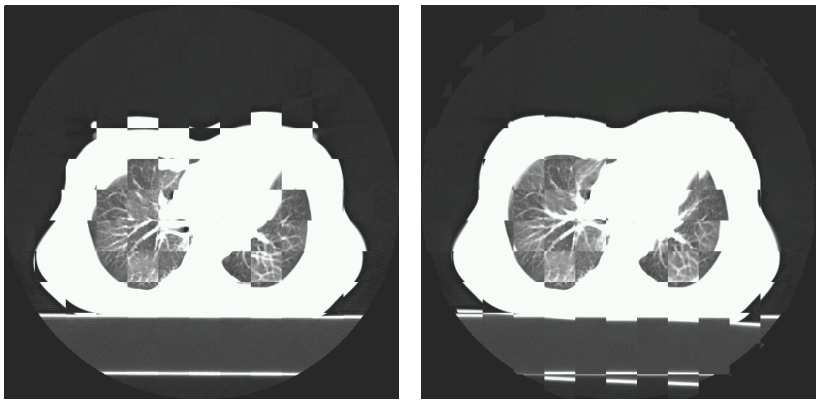

(e) Unregistered 200/600 (f) Registered 200/600

Figure 6.24: The examined slice is located at position -50. See the graph in Figure 6.23 , demonstrating the increase in correlation coefficient with respect to this slice location.

6.3.3.5 Summary

The already good registration result would be still better, if even more control point pairs had been detected. The reason for the lack of detected control points is probably the too large slice distance of 10 mm. If a corresponding landmark is not visible in one of the slices, the refinement of the candidates by local rigid registration will fail and the control point pair will be sorted out. Nevertheless, the comparison of the surfaces of the segmented lung of the real inhalation scan and the synthetic inhalation scan led to a good match with a mean distance of 2.894 mm compared to 6.261 mm mean distance before deformation (Table 6.10). In Figure 6.22 this fact is visualized. The checkerboards of Figure 6.24 also show the good match of the bronchioli, whereas the match of the contours of the left lobe of the lung could be more accurate.

6.3.4 Patient 4

A diseased lung is the target organ to be modeled in this test. For further information about the image data refer to Table 6.11. The parameters of the fully automatic detection of corresponding anatomical landmarks are listed in Table 6.12.

6.3.4.1 Input Data

Target organ	Lung
Modality	CT
Dimension (x, y, z)	512 x 512 x 32
Pixelspacing im mm (x, y, z)	0.82 x 0.82 x 10
Intermediate images	n. a.

Table 6.11: Information about the image data of patient 4.

6.3.4.2 Detection of Corresponding Anatomical Landmarks

	Boney structure	Soft tissue
Hounsfield window config. (center/width)	1200/600	200/600
Landmarking method	Full automatic detection (6.1.3.2)	
Cube size landmark detection (x, y, z)	20 x 20 x 5	10 x 10 x 5
Number of regions	8	
Number of candidates	400	400
Cube size moving image (x, y, z)	54 x 54 x 5	
Cube size fixed image (x, y, z)	108 x 108 x 10	118 x 118 x 12
Considered voxels required	20%	15%
Number of detected control point pairs	72	35
Number of points manually removed	2	1
Number of points manually added	3	0

Table 6.12: The parameters for the landmarks detection of patient 4.

6.3.4.3 Surface Distance Measurements

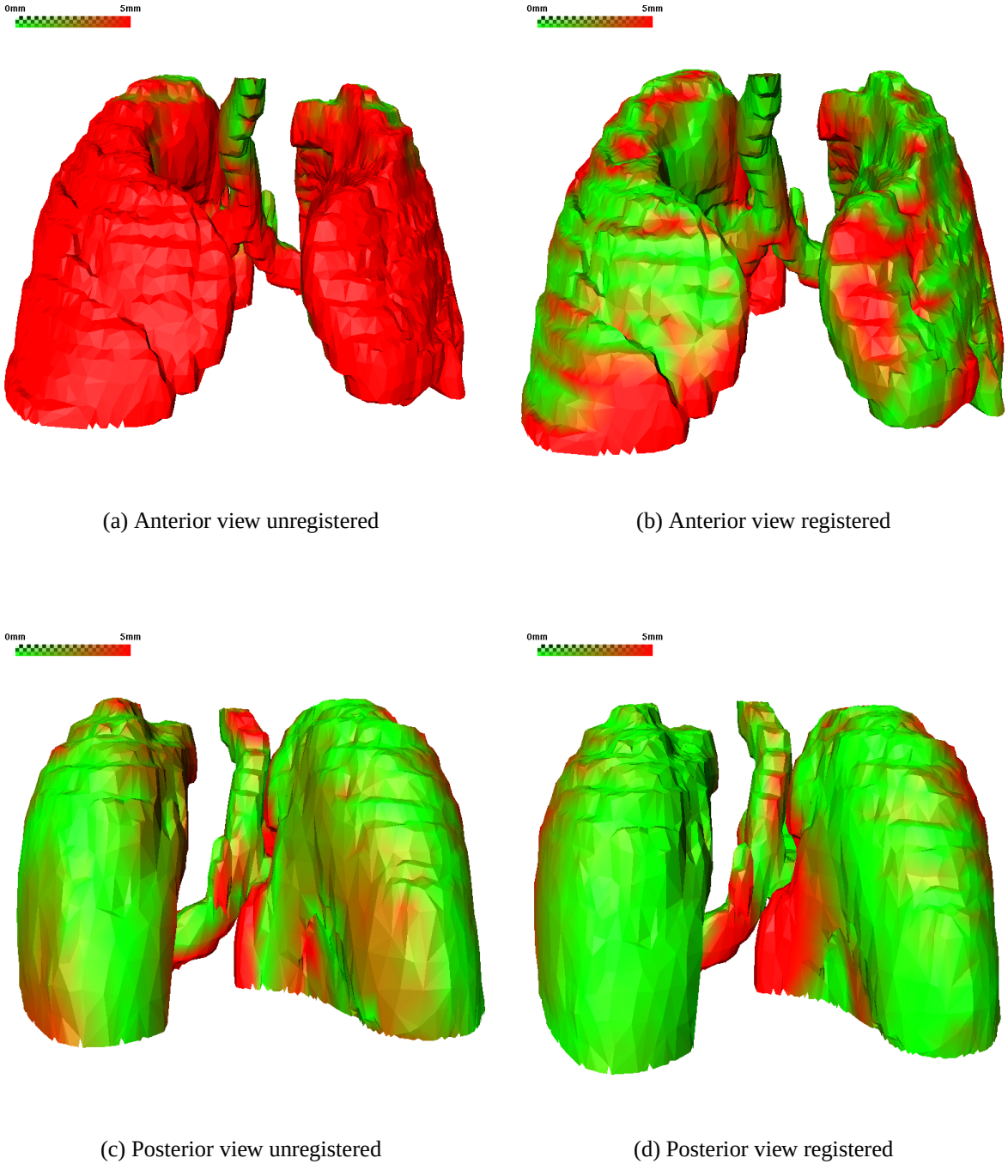

(a) Anterior view unregistered

(b) Anterior view registered

(c) Posterior view unregistered

(d) Posterior view registered

Figure 6.25: The inhaled lung is colored depending on the underlying distance to the exhaled lung (unregistered) and to the inhaled lung (registered) of the 4D model. The 4D patient model was computed using thin-plate splines.

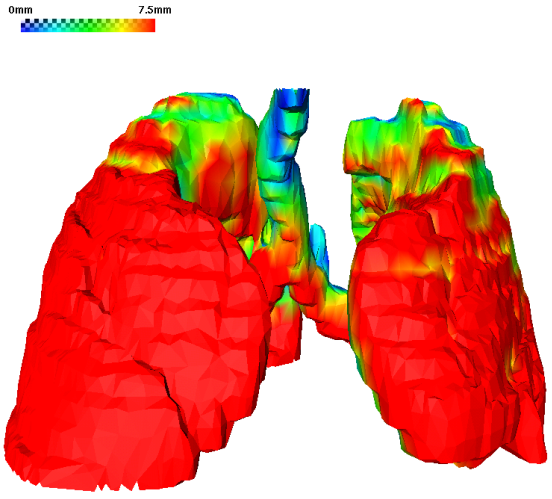

(a) Anterior view unregistered

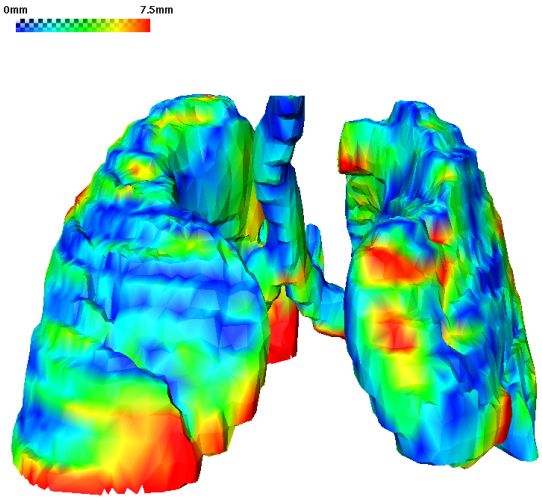

(b) Anterior view registered

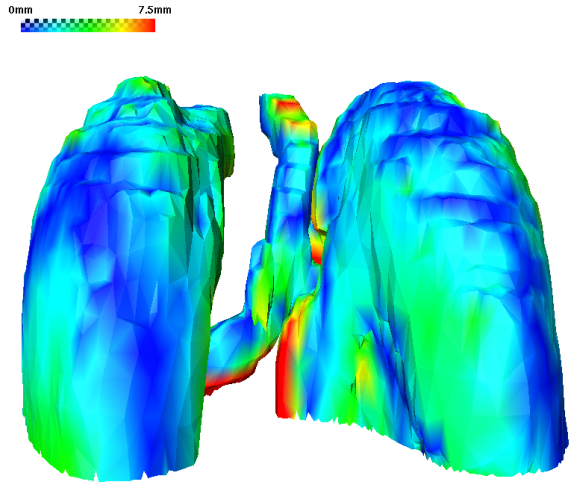

(c) Posterior view unregistered

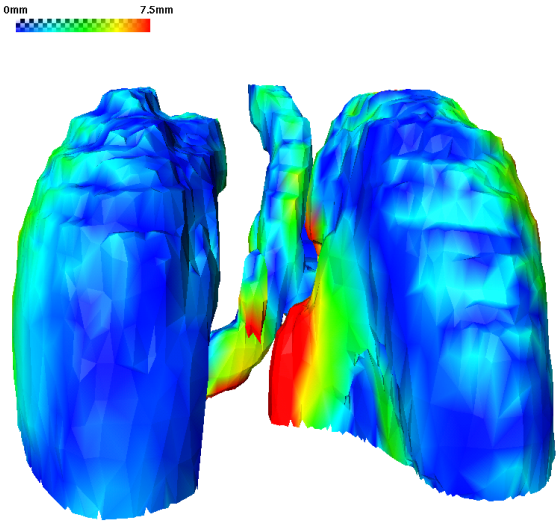

(d) Posterior view registered

Figure 6.26: The more detailed visualization, to point out registration outliers. With this patient, also a remarkable reduction of surface deviation in the dorsal part of the lung was to be observed.

[mm]	Mean dist.,	stand.dev.	rms	max	> 5 mm	> 7.5 mm	> 10 mm
Unregistered	5.712	4.553	7.304	19.992	46.674%	31.174%	20.0%
Registered bc	2.673	2.409	3.598	21.61	15.041%	4.883%	1.212%
Registered tps	2.342	2.177	3.198	16.140	11.933%	3.069%	0.612%

Table 6.13: The deformation by thin-plate spline interpolation yielded the best result with a mean distance of 2.342 mm.

6.3.4.4 Evaluation on the Complete Image Information

The graph in Figure 6.27 shows the correlation coefficients for each slice location before and after registration. Figure 6.28 emphasizes the very good registration result by visualizing checkerboards of one specific slice location.

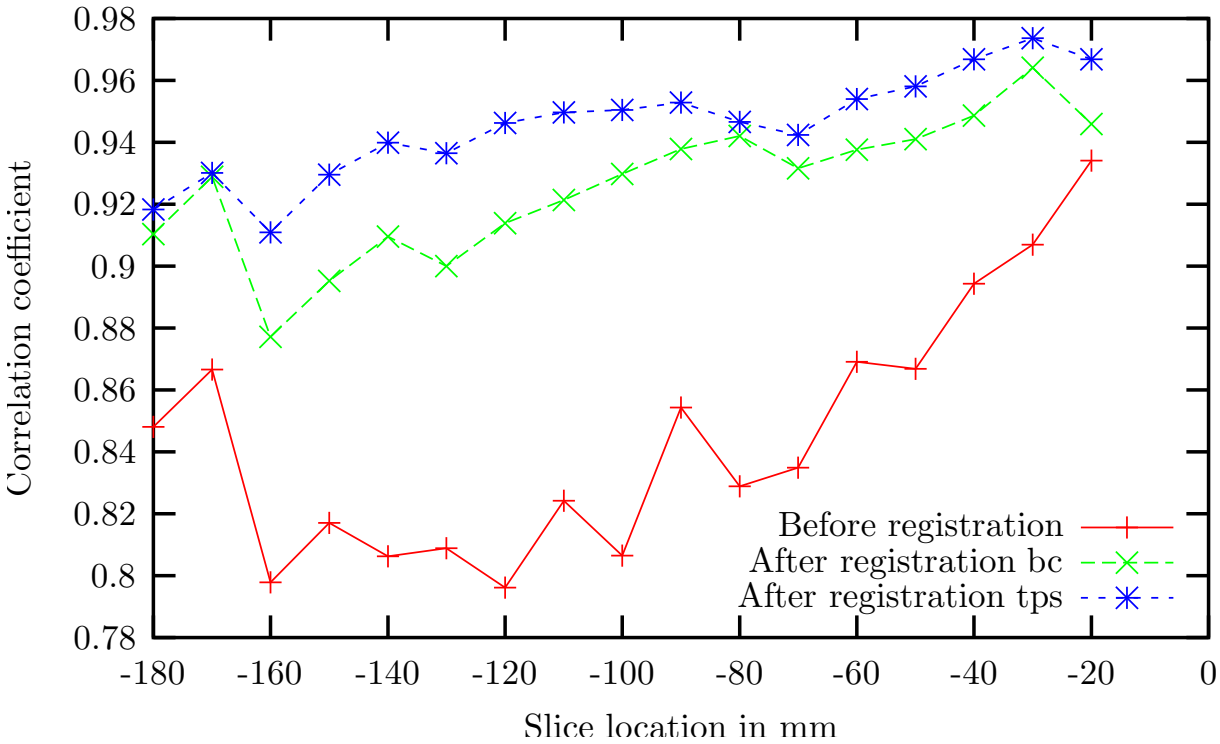

Figure 6.27: This graph emphasizes the large increase in correlation coefficient with respect to this elastic registration. Especially using thin-plate splines for deformation, very good measurement values could be obtained.

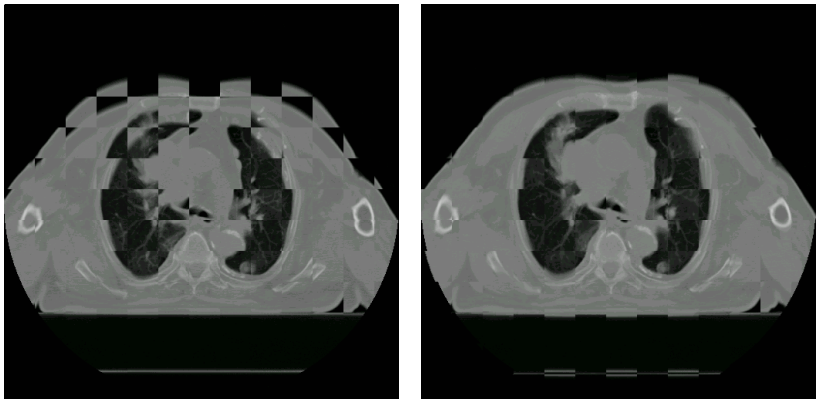

(a) Unregistered 2048/4096 (b) Registered 2048/4096

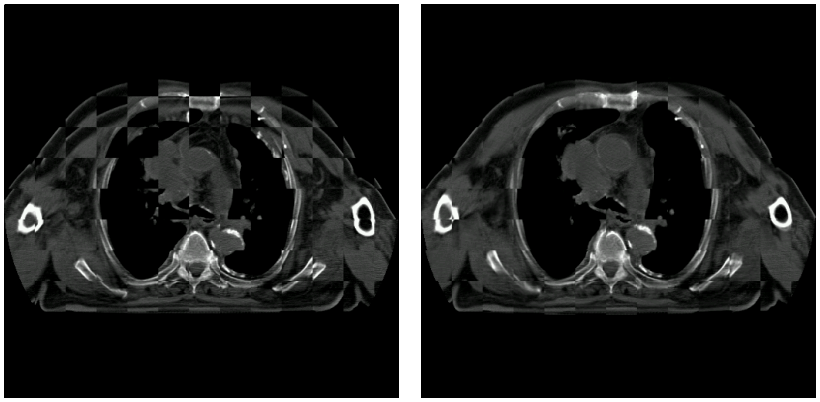

(c) Unregistered 1200/600 (d) Registered 1200/600

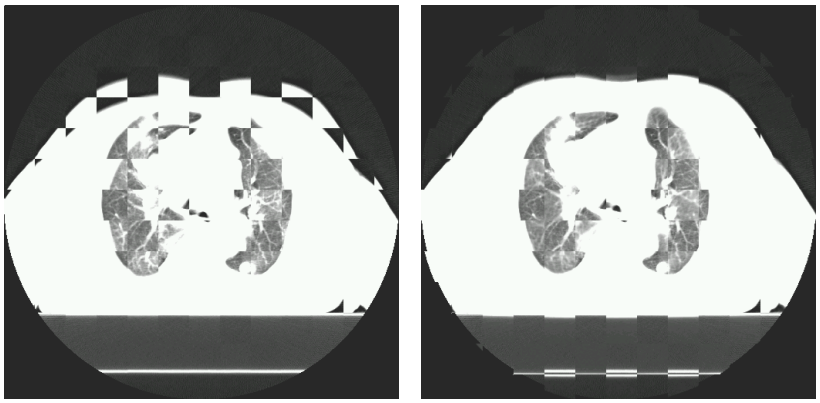

(e) Unregistered 200/600 (f) Registered 200/600

Figure 6.28: The examined slice is located at position -100. See the graph in Figure 6.27 emphasizing the increase in correlation coefficient at this specific location.

6.3.4.5 Summary

Again, for creating the volumetric deformation model of this patient data the full automatic landmark detection method in combination with thin-plate splines yielded the best results. Only a few manual corrections had to be made after visual inspection of the automatically detected corresponding landmarks. A mean surface distance of 2.342 mm means a very good result compared to a mean distance of 5.712 mm before registration (Table 6.13). In Figures 6.25 and 6.26 the results of the surface distance computations are visualized. The graph in Figure 6.27 as well as the checkerboards of Figure 6.28 emphasize the very good match of the performed elastic registration.

6.3.5 Patient 5

This data set also belongs to a lung cancer patient. In Table 6.14 further information about the image data is listed. The parameters used for the fully automatic corresponding landmark detection are specified in Table 6.15.

6.3.5.1 Input Data

Target organ	Lung
Modality	CT
Dimension (x, y, z)	512 x 512 x 18
Pixelspacing im mm (x, y, z)	0.938 x 0.938 x 10
Intermediate images	Intermediate images with known respiratory state (5.1.2).

Table 6.14: Information about the image data of patient 5.

6.3.5.2 Detection of Corresponding Anatomical Landmarks

	Boney structure	Soft tissue
Hounsfield window config. (center/width)	1400/600	200/600
Landmarking method	Full automatic detection (6.1.3.2)	
Cube size landmark detection (x, y, z)	20 x 20 x 5	10 x 10 x 5
Number of regions	8	
Number of candidates	400	287*
Cube size moving image (x, y, z)	54 x 54 x 5	
Cube size fixed image (x, y, z)	108 x 108 x 10	118 x 118 x 12
Considered voxels required	20%	15%
Number of detected control point pairs	40	11
Number of points manually removed	1	0
Number of points manually added	6	5

Table 6.15: 113 candidates ($\star$) were removed before refinement, because the detected landmarks were located on the treatment table and therefore had to be discarded.

6.3.5.3 Surface Distance Measurements

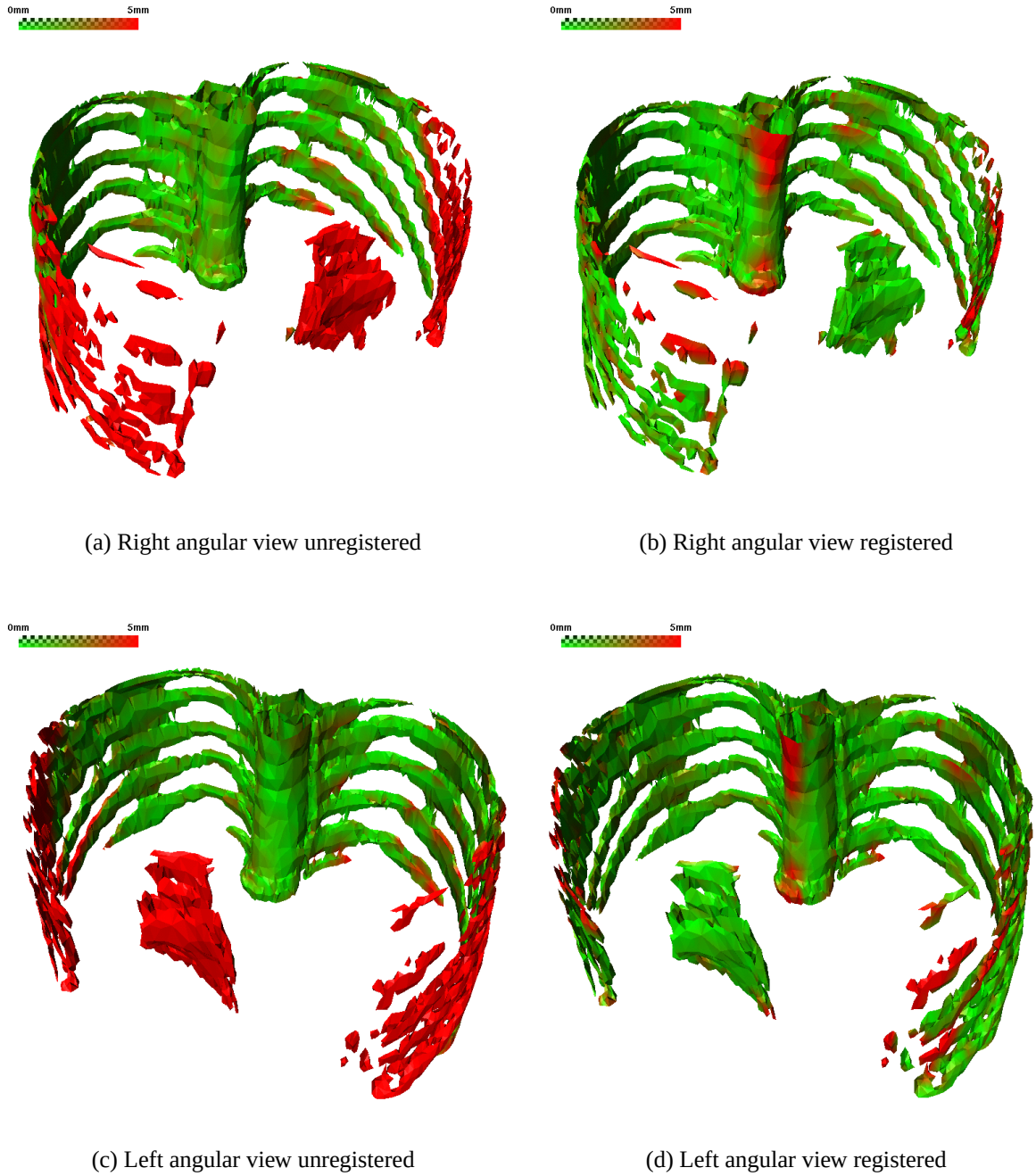

(a) Right angular view unregistered

(b) Right angular view registered

(c) Left angular view unregistered

(d) Left angular view registered

Figure 6.29: For evaluating the 4D model of this patient data, the segmented thorax was taken for comparison. The state of the ribcage is an important indicator for the current state of respiration. Only few deviations occur between the real ribcage and the synthetic ribcage at state of inspiration.

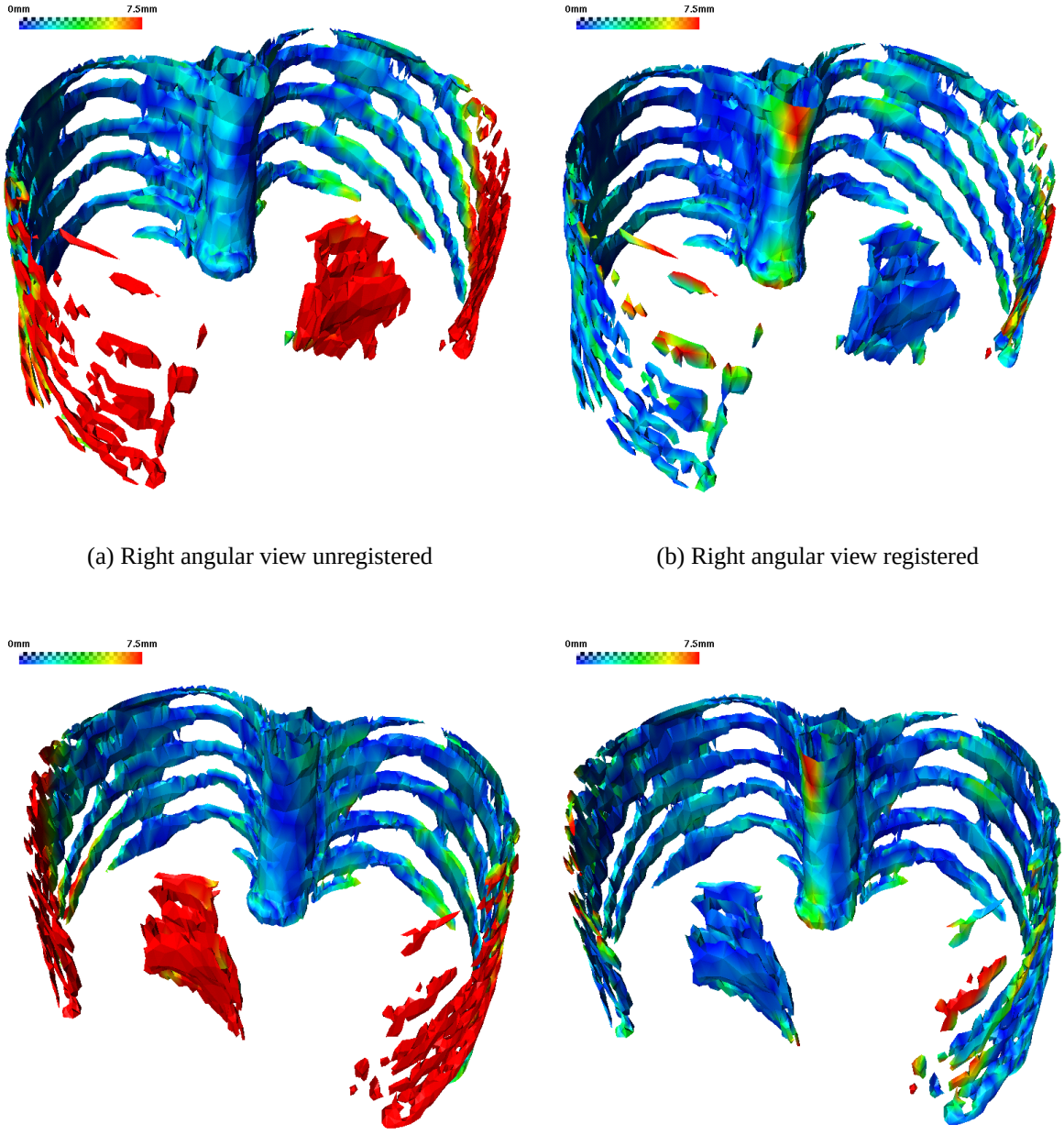

(a) Right angular view unregistered

(b) Right angular view registered

(c) Left angular view unregistered

(d) Left angular view registered

Figure 6.30: The more detailed view of the deviations shows a very accurate match of the real inhaled ribcage and the simulated one. Remarkable is the very good matching sternum, which is meaningful for classifying the breathing phase.

[mm]	Mean dist.,	stand.dev.	rms	max	> 5 mm	> 7.5 mm	> 10 mm
Unregistered	4.563	5.718	7.316	31.264	28.133%	23.724%	18.935%
Registered bc	2.889	2.858	4.064	20.932	18.617%	7.925%	3.138%
Registered tps	1.386	1.467	2.018	12.714	2.979%	1.194%	0.328%

Table 6.16: The deviations concerning the thorax of the model amounted to only 1.386 mm, with respect to the deformation when using thin-plate splines.

6.3.5.4 Evaluation on the Complete Image Information

In the graph of Figure 6.31 the corresponding slices of the exhalation and the inhalation scan are compared to each other (unregistered) as well as the slices of the synthetic inhalation scan (last slice of the 4D model) and the real inhalation scan (registered). Figure 6.32 illustrates the registration result at one slice location.

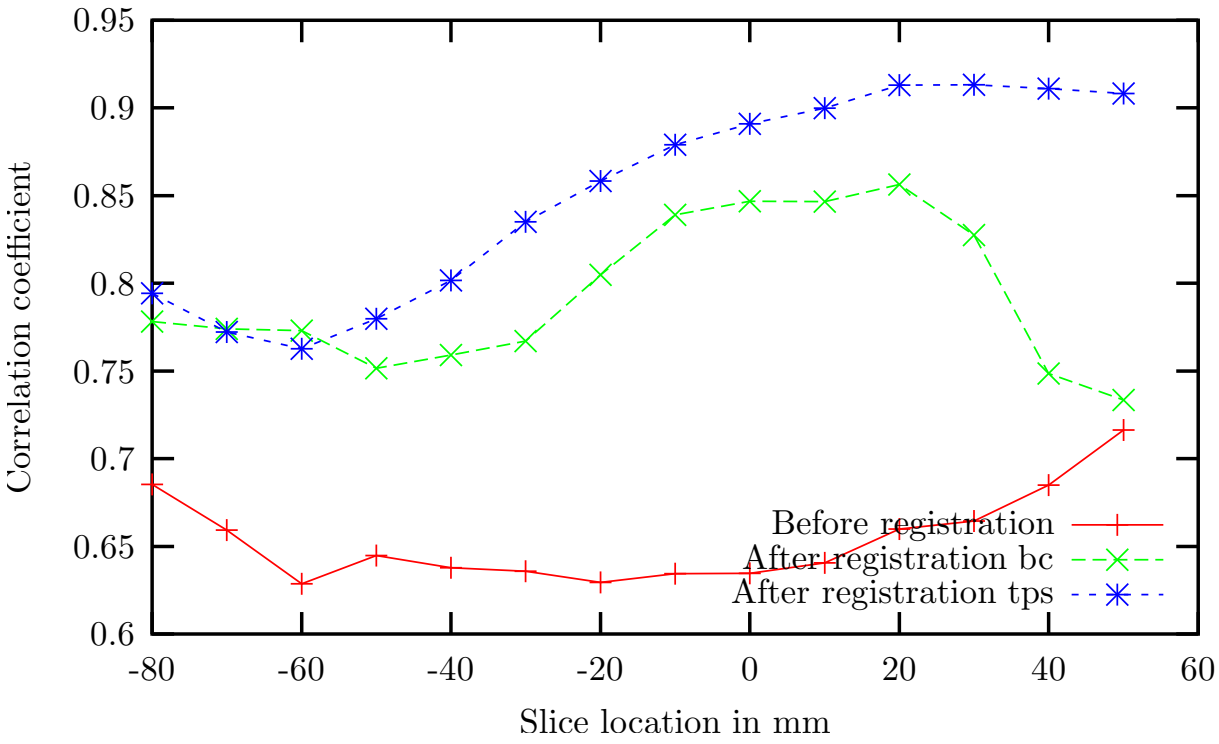

Figure 6.31: The correlation coefficients values are lower with this patient data, because the upper part of the images containing the information about the needle position was masked out.

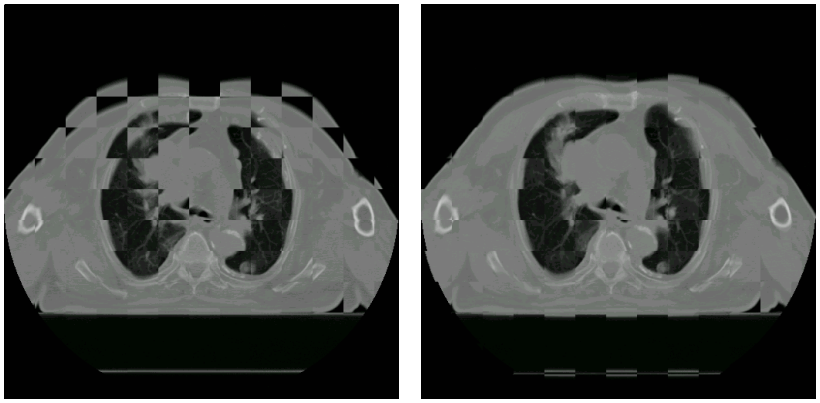

(a) Unregistered 2048/4096 (b) Registered 2048/4096

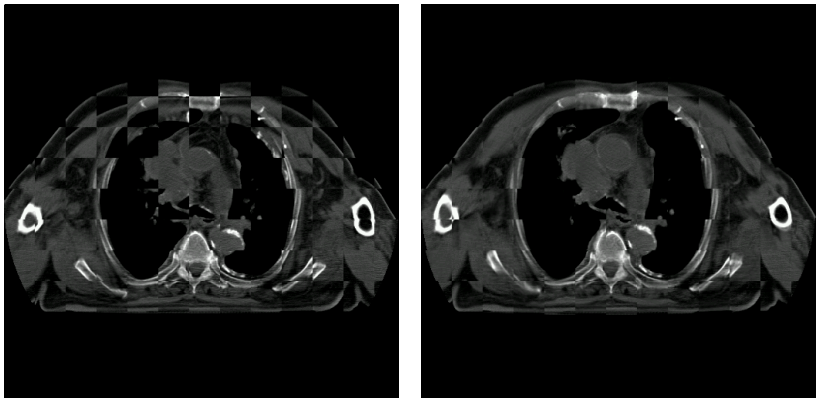

(c) Unregistered 1200/600 (d) Registered 1200/600

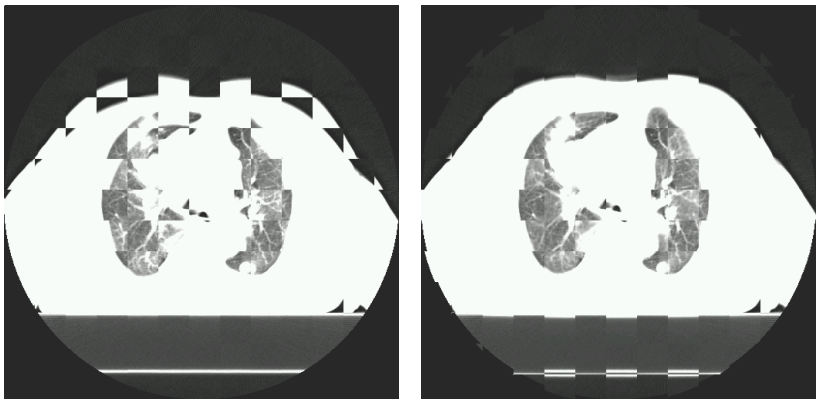

(e) Unregistered 200/600 (f) Registered 200/600

Figure 6.32: The examined slice is located at slice location 20. See the graph in Figure 6.31, displaying the increase in similarity for every slice location.

6.3.5.5 Summary

With this dataset, not enough corresponding anatomical landmarks could be detected for simulating the deformation of soft tissue, neither automatically nor manually. Probably the reason is that the patient could not hold his breath for the complete scanning time in case of exhalation (as demonstrated by the needle data in Figure 6.33), resulting in movement of the diaphragm.

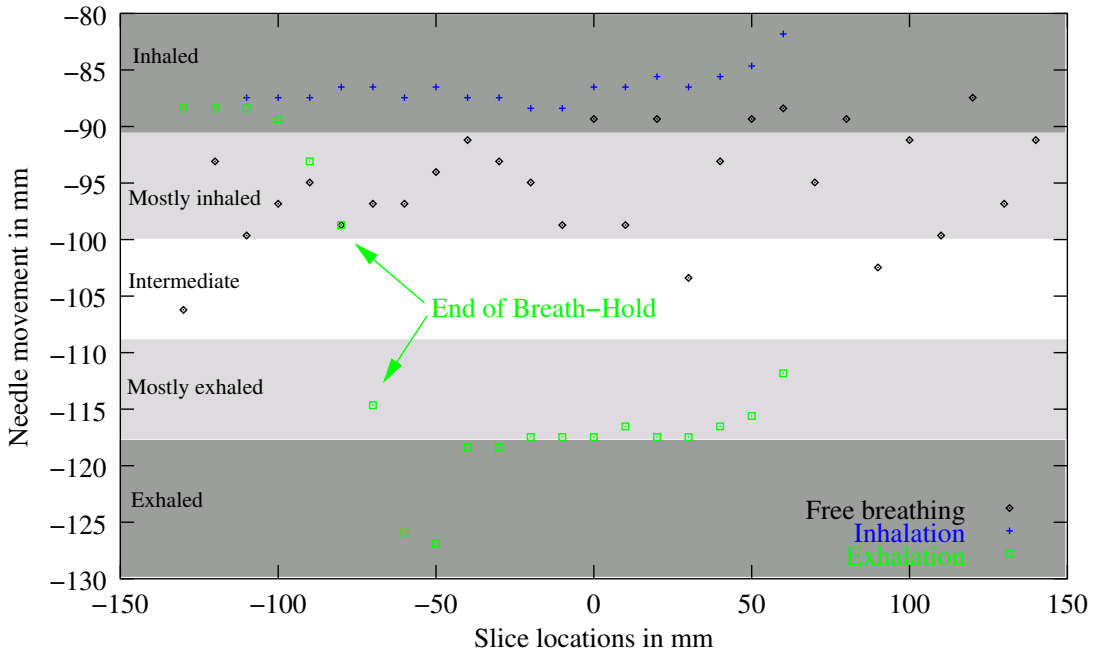

Figure 6.33: The respiratory curve of the scan taken during free breathing ranges near to that of the scan performed during inhaled breath-hold. The reason is that in case of the inhaled breath-hold the needle got in contact with the patient. It can be noticed that, in case of exhalation, the patient could not hold his breath for all the time (time runs from right to left).

Therefore, the ribcage and the spine were segmented to evaluate the deformation results (Figures 6.29, 6.30). Observing the movement of the different vertebrae to the sternum gives information about the current state of respiration. The vertebrae do not move and the sternum moves cranial-ventrally with inhalation. As demonstrated in Figure 6.29, the positions of the sternum and the vertebrae in the real and the synthetic inhalation scan match very accurately, very important for the 2D-4D registration process to be performed later for determining the respiratory state. Unfortunately, the intermediate CT images with assigned respiratory states were not usable for evaluation, because the needle got in contact with the patient during inhalation. Further experiments have to be performed to find the optimal position for the placement of the apparatus on the patient's chest.

6.3.6 Patient 6

In this case, the target organ to be modeled is the liver, which was taken by magnetic resonance imaging. As remarked in Table 6.17, this patient data also contains an intermediate scan, located approximately in the middle of the respiratory cycle. This volume scan was taken during breath-hold, as described in section 5.2.1. Therefore, the volumetric deformation models were evaluated by comparison to the reference scan, in this case the scan taken during exhalation, and to the intermediate scan. All three scans were available in two versions, one showing the complete image information and the other one showing only the segmented liver. The control point pairs were marked on the data of the segmented liver. For this patient data, the deformation was performed from the inhalation to the exhalation scan[4].

6.3.6.1 Input Data

Target organ	Liver
Modality	MR
Dimension (x, y, z)	512 x 384 x 64
Pixelspacing im mm (x, y, z)	0.68359375 x 0.68359375 x 2.5
Intermediate images	Intermediate scan (5.2.1)

Table 6.17: Information about the image data of patient 6.

6.3.6.2 Detection of Corresponding Anatomical Landmarks

For creating volumetric deformation models of this patient, the corresponding anatomical landmarks were detected one time manually and one time automatically. The manually selected point pairs were also refined using the method described in section 6.1.3.1. Manually selected corresponding anatomical landmarks, which could not be refined were not thrown away in contrast to using the automatic generation of the candidates. The reason for this is that the manually selected points are not only approximately corresponding candidates.

The resulting 4D patient models, obtained through manual detection, refined manually detection and fully automatic detection of corresponding anatomical landmarks, were compared to each

[4]The reason for this is that the volumetric deformation model was created in the method's first iteration.

other. In Tables 6.18 and 6.19 the parameters for the fully automatic detection and the refinement of the manual selection are specified.

	No tissue distinction
Window config. (center/width)	40/80
Landmarking method	Full automatic detection (6.1.3.2)
Cube size landmark detection (x, y, z)	10 x 10 x 5
Number of regions	8
Number of candidates	300
Cube size moving image (x, y, z)	54 x 54 x 5
Cube size fixed image (x, y, z)	108 x 108 x 10
Considered voxels required	20%
Number of detected control point pairs	81
Number of points manually removed	0
Number of points manually added	0

Table 6.18: The parameters for the full automatic landmark detection. Please note that this detection was performed on the segmented liver, not on the whole image information.

	No tissue distinction
Window config. (center/width)	40/80
Landmarking method	Refinement of manually selected point pairs (6.1.3.1)
Cube size landmark detection (x, y, z)	-
Number of regions	1
Number of candidates	86
Cube size moving image (x, y, z)	54 x 54 x 5
Cube size fixed image (x, y, z)	70 x 70 x 7
Considered voxels required	20%
Number of detected control point pairs	86
Number of points manually removed	0
Number of points manually added	0

Table 6.19: The parameters for the refinement of the corresponding anatomical landmarks, selected manually by an expert.

6.3.6.3 Comparison to Reference Scan

Surface Distance Measurements

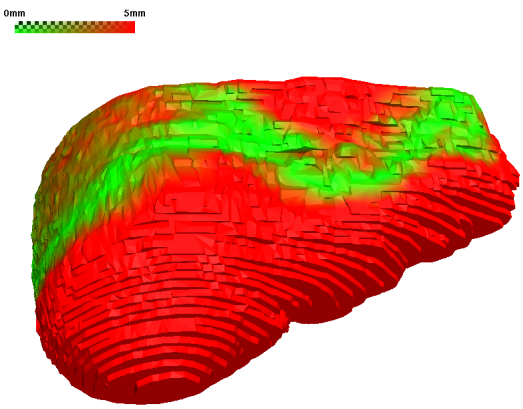

(a) Anterior angular view unregistered

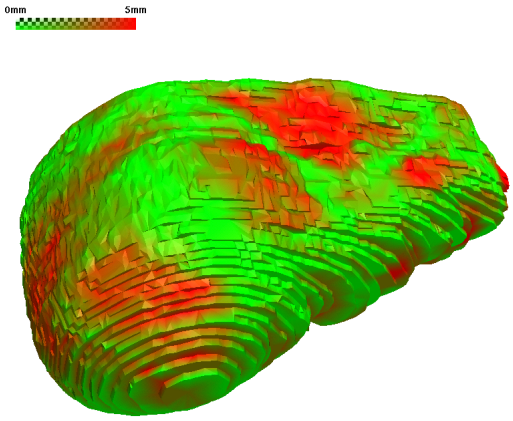

(b) Anterior angular view registered

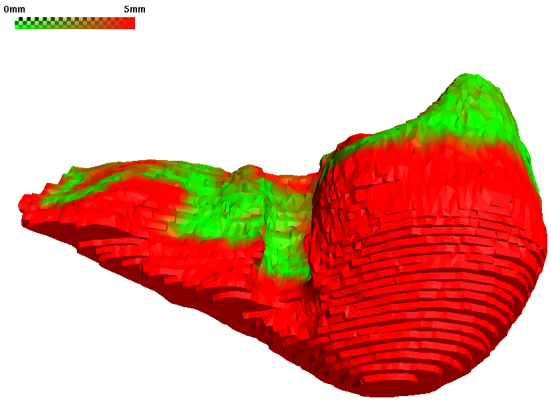

(c) Posterior angular view unregistered

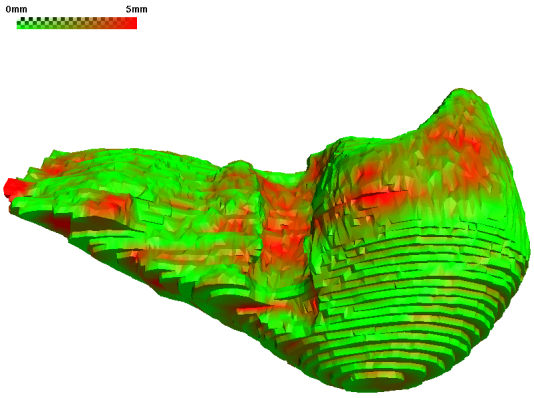

(d) Posterior angular view registered

Figure 6.34: On the left, the 'unregistered' liver demonstrates the deformation due to respiration. On the right, the visualized surface distances between the segmented liver of the real and the simulated expiration scan emphasize the very good result.

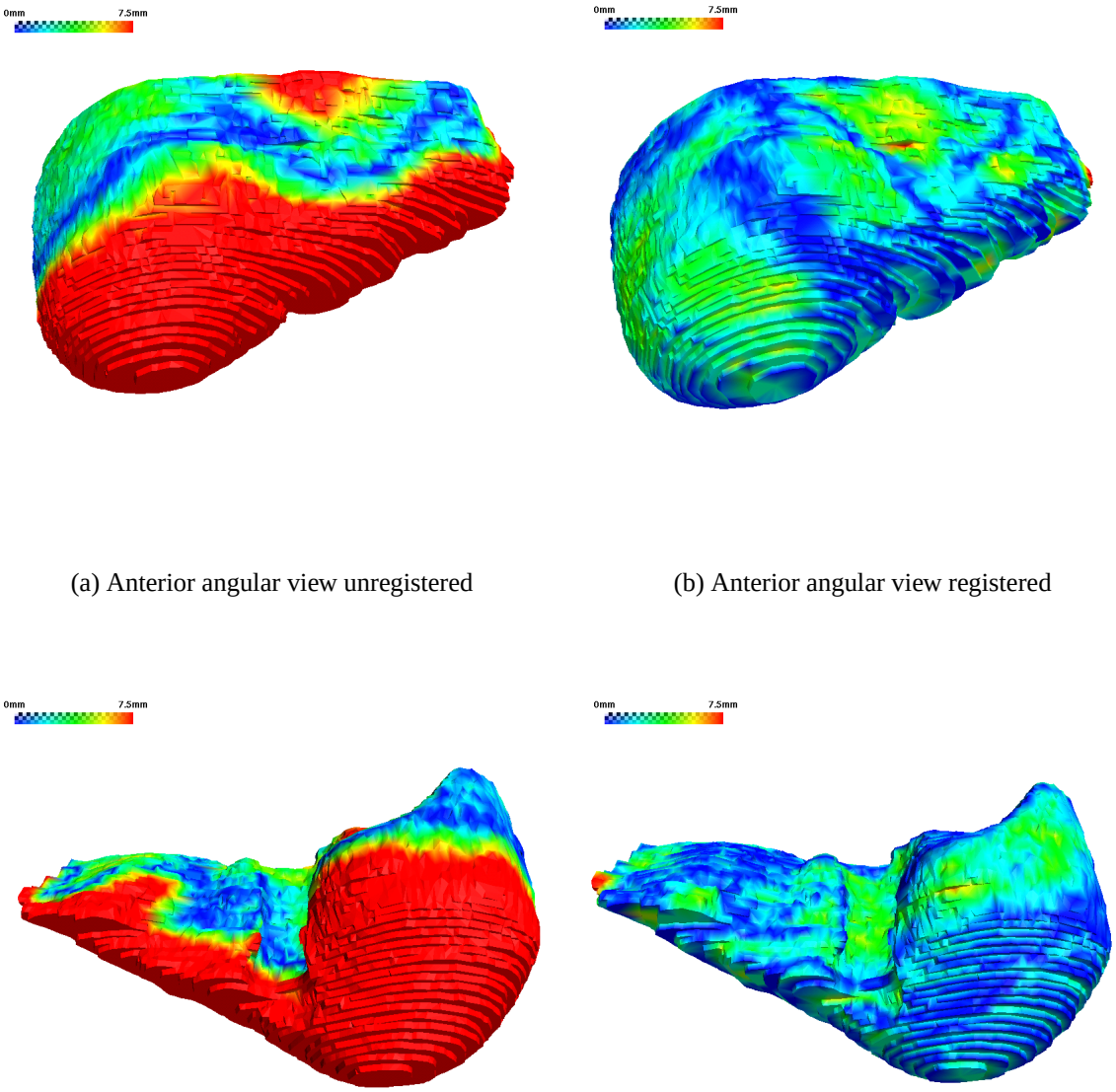

(a) Anterior angular view unregistered

(b) Anterior angular view registered

(c) Posterior angular view unregistered

(d) Posterior angular view registered

Figure 6.35: This more detailed visualization gives information about the location of the outliers. The model was computed using thin-plate splines. The corresponding measurements are listed in Table 6.20.

6.3.6.4 Comparison to Intermediate Scan

Surface Distance Measurements

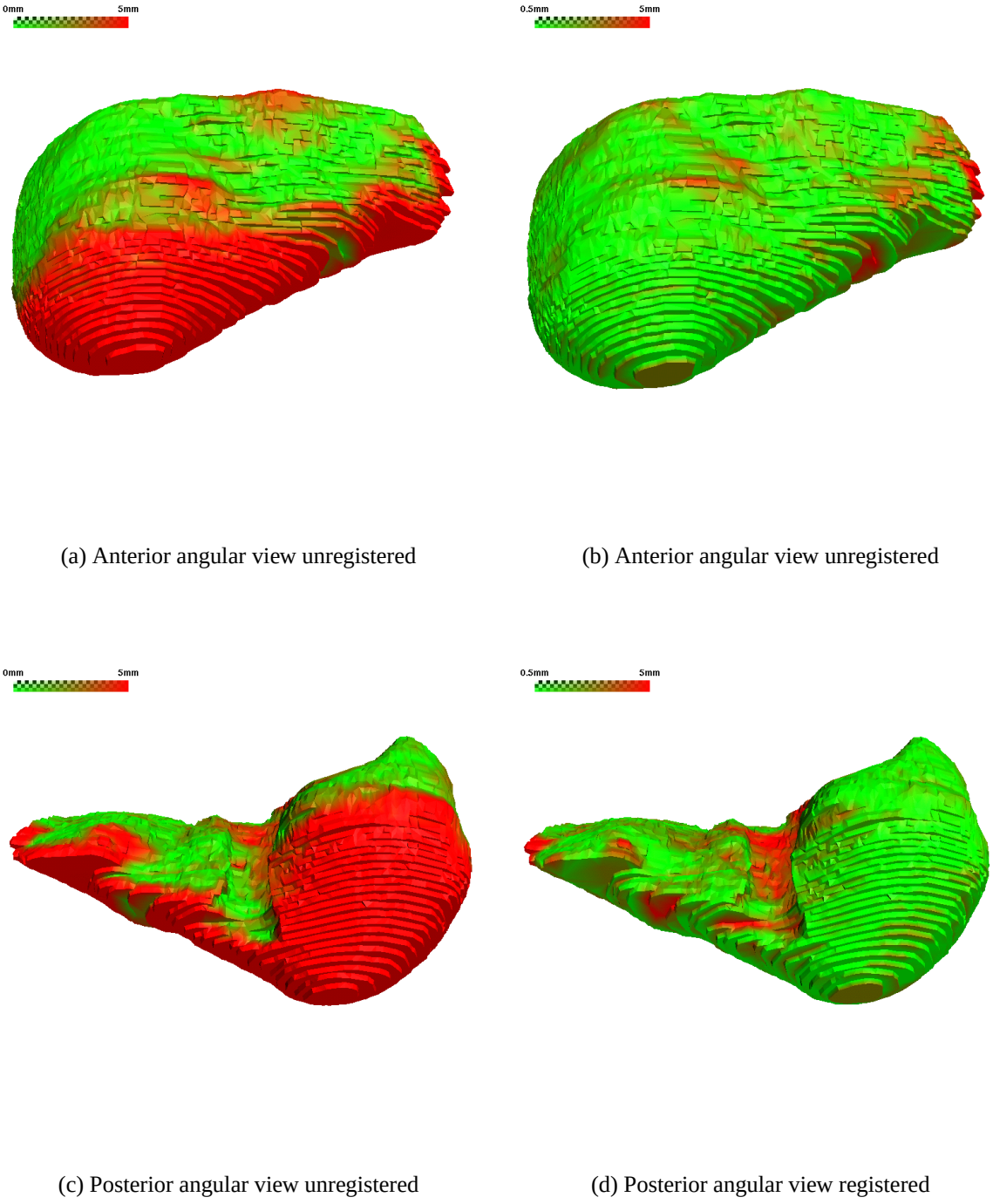

(a) Anterior angular view unregistered

(b) Anterior angular view unregistered

(c) Posterior angular view unregistered

(d) Posterior angular view registered

Figure 6.36: The visualization of the comparison of the intermediate scan and the 4D model, which was computed using thin-plate splines and the fully automatically detected corresponding anatomical landmarks.

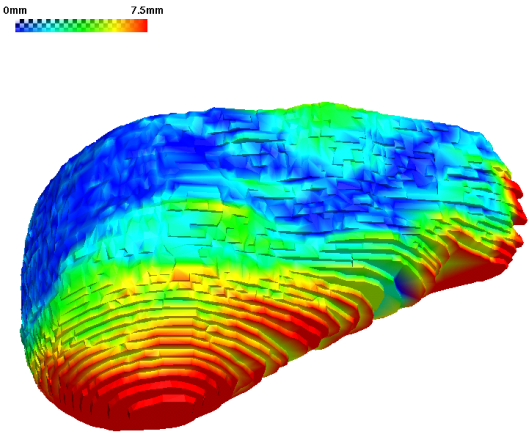

(a) Anterior angular view

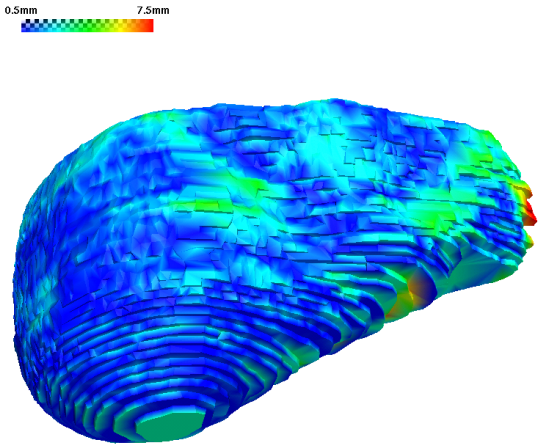

(b) Anterior angular view

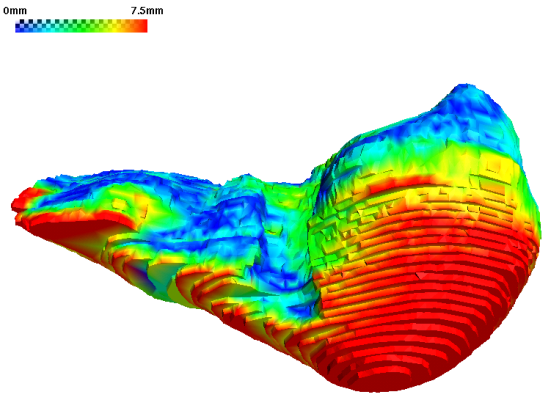

(c) Posterior angular view

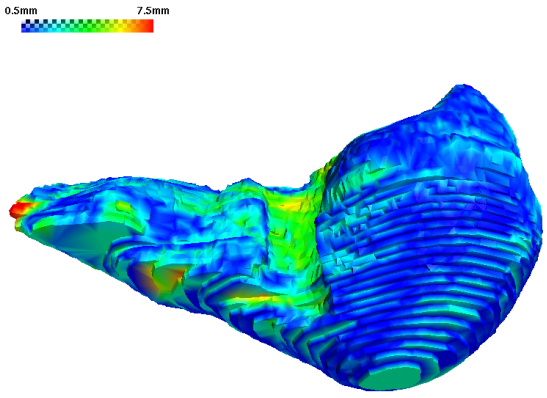

(d) Posterior angular view

Figure 6.37: This more detailed view shows the registration outliers. The corresponding distance measurements are listed in Table 6.21.

Table 6.20 contains the data of the computed surface distances corresponding to Figures 6.34 and 6.35. The surface of the segmented liver of the reference scan (the inhalation scan in this case) was compared to that of the particular 4D models computed using the different methods.

[mm]	Mean dist.,	stand.dev.	rms	max	> 5 mm	> 7.5 mm	> 10 mm
Unregistered	8.373	6.876	10.834	25.350	54.927%	46.453%	38.216%
Registered bc	2.048	1.830	2.747	17.051	6.588%	1.279%	0.426%
Registered tps	2.049	1.778	2.713	18.177	5.174%	1.100%	0.550%
Reg. bc refined	2.151	2.086	2.996	14.973	11.077%	2.660%	0.426%
Reg. tps refined	1.722	1.511	2.291	15.103	2.918%	0.752%	0.303%
Reg. bc auto	2.278	1.688	2.835	11.510	7.295%	0.651%	0.045%
Reg. tps auto	1.732	1.347	2.183	10.866	1.055%	0.135%	0.045%

Table 6.20: This table compares the computed surface distances of the reference scan to the models, calculated by using one of the two interpolation methods in combination with one of the three techniques for detection of corresponding control points.

Table 6.21 contains the data of the computed surface distances corresponding to Figures 6.36 and 6.37. The graph in Figure 6.39 shows that the intermediate scan matches best, as expected, approximately in the middle of the respiratory cycle. The surfaces of the segmented liver of the particular 4D model's synthetic scans yielding these best matches, were compared to the segmented liver of the intermediate scan.

[mm]	Mean dist.,	stand.dev.	rms	max	> 5 mm	> 7.5 mm	> 10 mm
Unregistered	3.624	2.856	4.614	14.320	31.326%	12.044%	2.712%
Registered bc	1.467	1.509	2.104	15.947	2.627%	0.746%	0.287%
Registered tps	1.368	1.473	2.010	15.826	2.145%	0.677%	0.298%
Reg. bc refined	1.585	1.577	2.236	14.538	3.762%	0.872%	0.275%
Reg. tps refined	1.364	1.435	1.980	14.702	2.019%	0.711%	0.275%
Reg. bc auto	1.786	1.611	2.405	13.512	4.336%	0.677%	0.138%
Reg. tps auto	1.312	1.300	1.847	12.764	1.721%	0.252%	0.138%

Table 6.21: The segmented organ of the intermediate scan was compared to that of the different 4D models. In every case, it was compared to the synthetic scan of the 4D model, which yielded the highest correlation coefficient (Figure 6.39).

6.3.6.5 Evaluation on the Complete Image Information

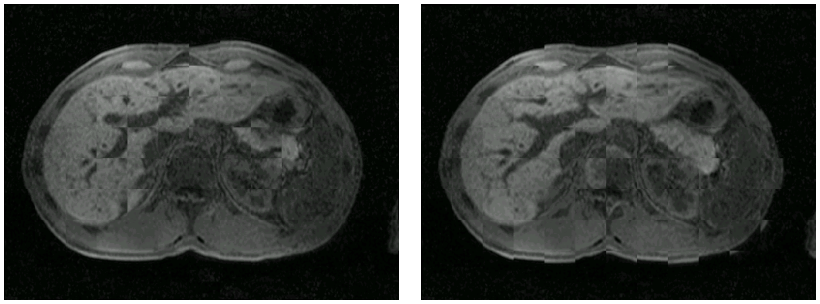

(a) Unregistered transversal view (b) Registered transversal view

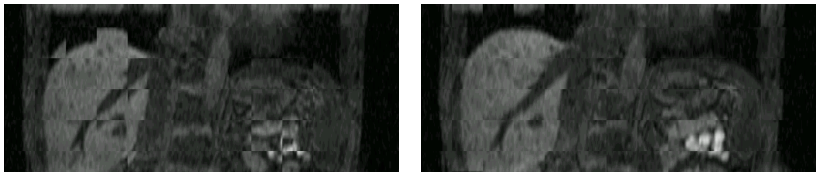

(c) Unregistered frontal view (d) Registered frontal view

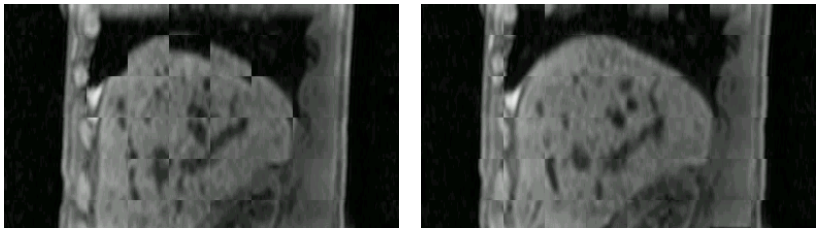

(e) Unregistered sagittal view (f) Registered sagittal view

Figure 6.38: This figure demonstrates the very good match of the intermediate scan to the 4D model by checkerboards of corresponding slices in the transversal, the frontal and the sagittal plane. Interesting to see is that liver moves mainly in cranial-caudal direction. Again the 4D model computed using thin-plate splines and the full automatic landmark detection was used for evaluation.

6.3.6.6 Summary

This data was very useful for evaluation, because of the availability of a complete set of corresponding anatomical landmarks selected by an expert, which allowed for benchmarking the quality of the automatically detected landmarks. In both cases, that is the comparison of the

intermediate scan as well as the comparison of the reference scan to the 4D model, the fully automatic landmark detection yielded the best results (Tables 6.20, 6.21). Furthermore, the results of the computed surface distances of the segmented liver were very good, with 1.312 mm mean distance (SD 1.3 mm) in case of the intermediate scan, and 1.732 mm (SD 1.347 mm) in case of the reference scan, accordingly. The graph in Figure 6.39 emphasizes that the intermediate scan matches best, as expected, approximately in the middle of the respiratory cycle. Figure 6.38 demonstrates very good matches in the transversal, frontal and sagittal plane.

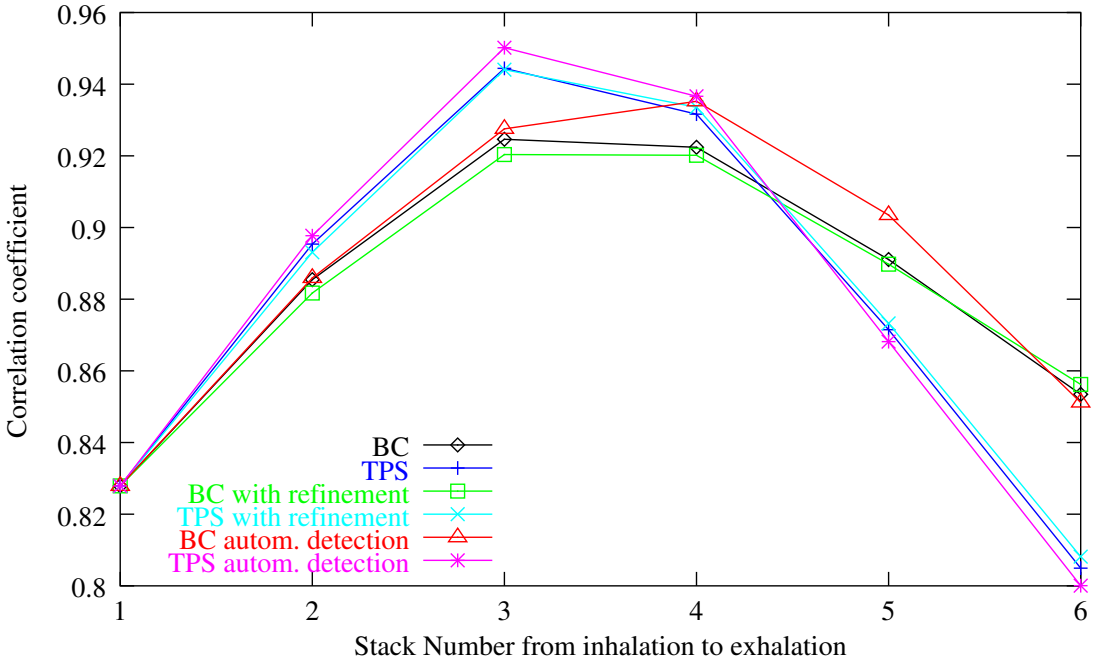

Figure 6.39: The intermediate scan was compared to the six synthetic scans forming the 4D models, computed using the six different methods. As expected, the best matches were located in the middle of the respiratory cycle. Again the images of the segmented liver were used for comparison. (’BC’ stands for barycentric coordinates and ’TPS’ for thin-plate splines.)

Besides these very good results, another evaluation with respect to the creation processes of the 4D models was performed using this data set. As described in section 6.1.2, a linear movement of the particular landmarks was assumed, when computing the thin-plate spline function for every single respiratory phase. This assumption was checked by additionally determining the same landmarks in the intermediate scan as the manually detected in the exhalation and inhalation scan. The distances of the landmarks of the intermediate scan to the lines, defined by the corresponding control point pairs, were calculated. The resulting mean deviation was 2.451 mm with a standard deviation of 1.277 mm for the 86 points. By using these additionally

selected landmarks, the inhalation scan was registered to the intermediate scan, to demonstrate the advantage of more accurate control points. In Table 6.22 the resulting surface distances of the deformation by the interpolated landmark and the real landmark positions are compared to each other. Though, as expected, the mean surface distance was smaller for the real landmark positions, the difference was not that high.

[mm]	Mean dist.,	stand.dev.	rms	max	> 5 mm	> 7.5 mm	> 10 mm
Reg. tps int. lms	1.368	1.473	2.010	15.826	2.145%	0.677%	0.298%
Reg. tps real lms	1.340	1.292	1.861	14.572	1.686%	0.321%	0.195%

Table 6.22: The result obtained by using the interpolated landmarks is nearly as good as that achieved by the real landmarks.

Thus, it was confirmed that the movement of the landmarks is approximately linear, but more evaluation data has to be investigated for further exploration.

6.4 Résumé

This section summarizes the suggested methods and comments the corresponding related work for modeling the occurring movements due to respiration in volume data sets.

When using finite element analysis for creating a 4D model of the liver, as Brock et al. (see section 6.2.2) did, there is the problem of obtaining the different material properties, which also differ from patient to patient. Rohlfing et al. [Rohlfing 01] expressed the same doubt in his paper, and also trusted in an intensity-based non-rigid registration approach, but instead of using thin-plate spline interpolation, they used B-spline interpolation between uniformly placed control points for transformation (section 6.2.5). By use of the Nelder-Mead simplex algorithm, Coselmon et al. tried to optimize the positions of the homologous points, according to the match of the two data sets measured by mutual information, as described in section 6.2.3.

Applying this method to our goal of performing an elastic registration not only on the right lobe of a segmented lung, but on the complete image information, simply seems unrealistic. To optimize the positions of more than 100 control points, would surely mean too many degrees of freedom for the algorithm. To form a point distribution model (PDM) out of corresponding surface landmarks determined by non-rigid registration, as Blackall et al. did (see section 6.2.1), yields very accurate models of the liver, but in the approach of this thesis the focus is set on modeling the movements due to respiration of all structures visible in the image data. The

Demons algorithm used by Wang et al., as described in 6.2.4, surely also represents a method well suited for elastic registration, but not necessarily for computing a 4D model.

The method, suggested in this work, for fully automatic detection of corresponding anatomical landmarks in volume scans of different respiratory state, yielded very accurate 4D models by using thin-plate spline interpolation. Using thin-plate splines for deformation, higher accuracies were obtained than by using barycentric coordinates.

The idea of tessellating the volume to be deformed into cubes and taking the centers of mass of the cubes with the highest entropies as control point candidates for the subsequent refinement by local rigid registration, showed great robustness. Only 2.04% of the automatically detected control point pairs of the whole evaluation data had to be sorted out by visual inspection and only 5.05% had to be added manually. The accuracy of the computed 4D models was very high in almost every dataset. The mean surface distances of the segmented organs varied from 1.312 to 2.894 mm, when using thin-plate spline interpolation. Whereas the organs, except the liver, were segmented by thresholds, yielding many outliers, which obviously negatively influence the results.

Concerning the CT volumes, slice distances lower than 10 mm certainly would be better suited for automatically detecting corresponding anatomical landmarks. Many control point candidates were discarded, because the information relevant for refinement was not visible in the reference scan.

With respect to the determination of the breathing phase by the 2D-4D registration procedure, it has to be emphasized that in the periodically taken X-ray images, required in this case, mainly bony structures are visible. Therefore, it is important to take into account the ribcage, which rises due to respiration. The vertebral bodies don’t move, but the sternum moves cranial-ventrally. The evaluations performed, showed very accurate matches with respect to the described deformation of the ribcage. This is demonstrated by the comparisons between corresponding slices of real and synthetic scans, as can be seen for example in Figure 6.14. Moreover, the segmented ribcage in state of inhalation of the volumetric deformation model computed for patient 5, matches very accurately the segmented ribcage of the real inhalation scan (see Figure 6.30). In all test cases, the full automatic detection of the corresponding anatomical landmarks, yielded a high number of control points located in spine and sternum, which characterize this movement.

Recapitulating, it has to be emphasized that within this approach the 4D model is needed for determining the respiratory state by matching 2D radiographs to the model, as demonstrated in the next chapter.

7 2D - 4D Registration Process

This chapter explains the 2D-4D registration procedure in detail. Furthermore, its feasibility is demonstrated by evaluations performed on five computed tomography data sets. Premise for this registration procedure is a computed volumetric deformation model, as described in chapter 6, consisting of a number of synthetic scans.

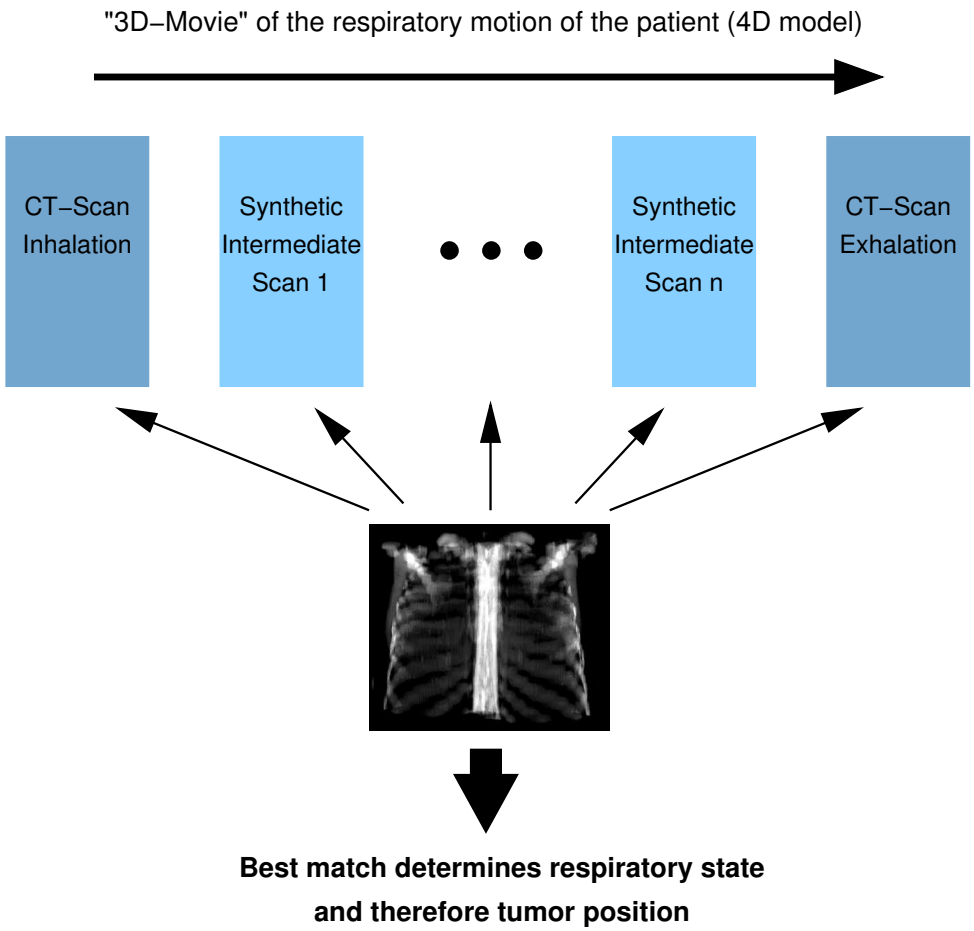

Figure 7.1: The two mutually orthogonal X-ray images are compared to all the synthetic scans of the model to infer the respiratory state and therefore the position of the target.

To determine the respiratory state within the novel system of tracking tumors introduced in this work, two simultaneously taken, mutually orthogonal radiographs are matched to the computed

4D model. Two mutually orthogonal X-ray images are required to achieve robust and good matching results. The 2D-4D registration consists of several independent 2D-3D registration processes, as visualized in Figure 7.1.

Both X-ray images are successively matched to all the synthetic scans included in the 4D model, and the best match yields the respiratory state. The tumor is not visible in the radiographs, but its position in the 4D model has been marked before by an expert. Thus, the best match of the procedure does not only yield the respiratory state, but also the position of the tumor. The 2D-3D matching is realized by the method of Roth et al. [Roth 04]. It represents an intensity-based rigid registration algorithm, which uses Hooke-Jeeves Pattern-Search for optimization and usually correlation coefficient or mutual information as similarity measure. As hardware-accelerated volume rendering based on texture mapping is used for DRR generation, one single 2D-3D registration takes only about 10 seconds. Therefore, the algorithm certainly is very well suited for building up the correlation model from external to internal motion, as described in chapter 4.

Figure 7.2: The detectors of the stereo X-ray imaging of the Cyberknife® Radiosurgical System.

7.1 Results

As we unfortunately did not have available any X-ray images in combination with corresponding volume scans taken during inhalation and exhalation, evaluations were performed using digitally reconstructed radiographs created from the 4D patient models specified in section 6.3.

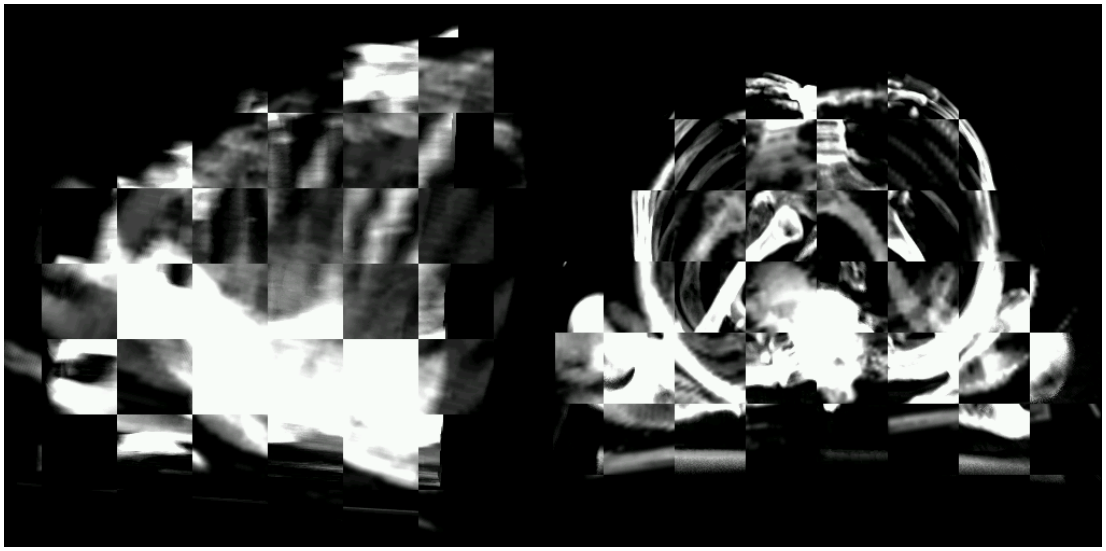

(a) Unregistered

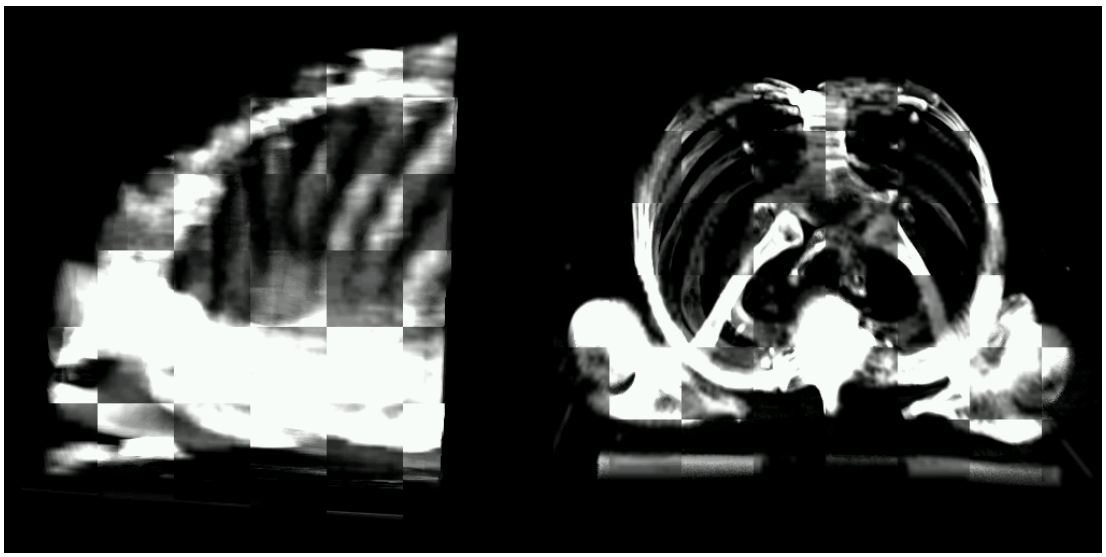

(b) Registered

Figure 7.3: Every single 2D-3D registration was started with the same initial pose (unregistered). These checkerboards show the X-ray images (in this case DRRs) unregistered and registered to the volume they were generated from. As can be seen, the X-ray images are mutually orthogonal to each other. Mutual information was used as similarity measure.

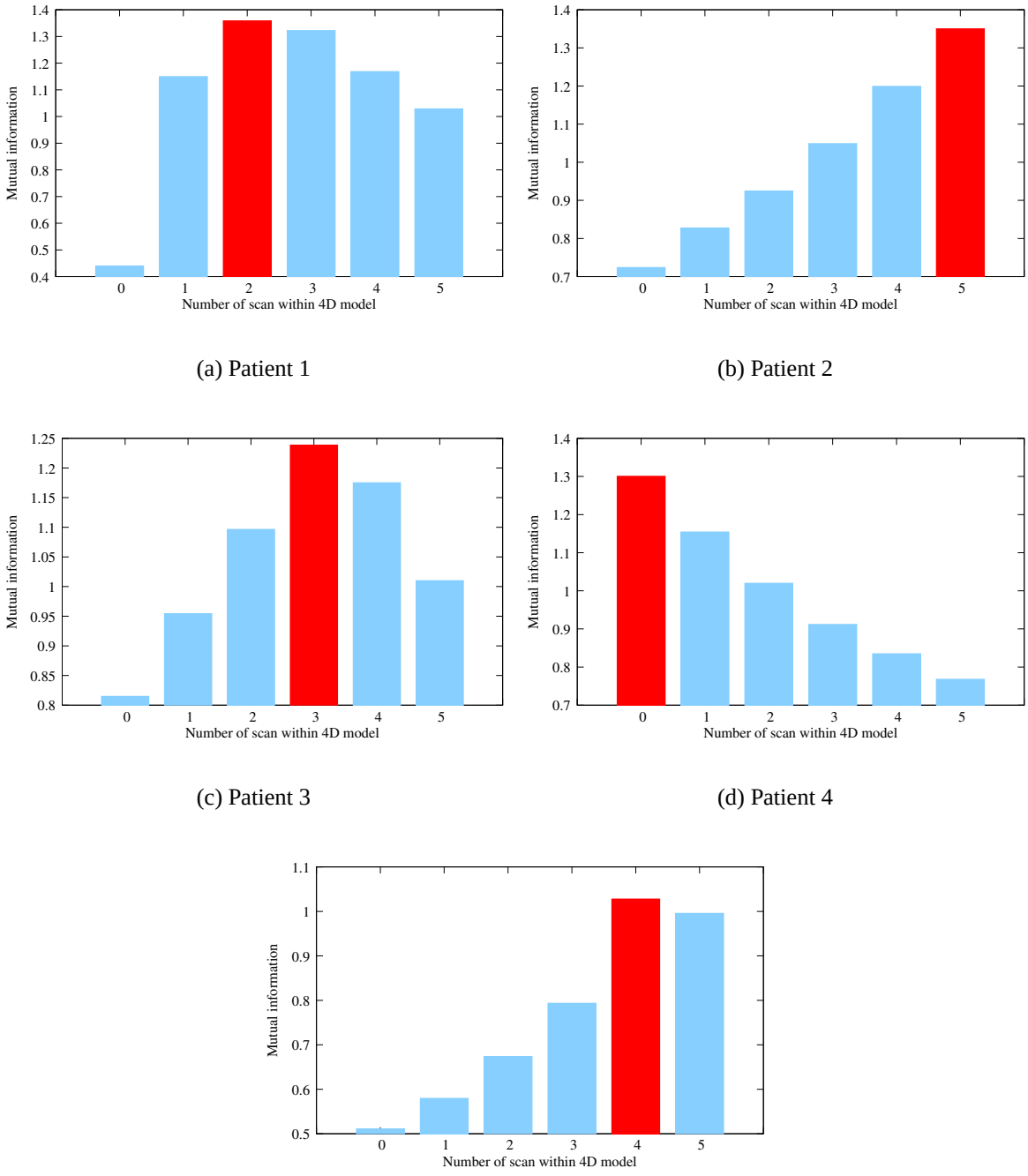

(a) Patient 1

(b) Patient 2

(c) Patient 3

(d) Patient 4

(e) Patient 5

Figure 7.4: These graphs show the results of the 2D-4D registration process of the CT test data, discussed in chapter 6. The red boxes mark the scan from which the DRRs were generated. In every case this scan of course was the one that matched best with the DRRs, but the neighboring scans yielded the next best results.

For every test data from one arbitrary chosen synthetic scan, two mutually orthogonal DRRs were computed, which were matched afterwards to the generated 4D patient model. Every single 2D-3D registration procedure was initialized with the same pose. In Figure 7.3 the initial misalignment is demonstrated. The best match naturally was the stack originating the created DRRs, but the neighboring stacks led to the next best results. The greater the difference between the respiratory states, the worse the result of the used metric, as can be seen in Figure 7.4. This emphasizes the robustness of the proposed 2D-4D registration procedure. With respect to the data of patient 1 in Figure 7.4(a), the mutual information measure yielded a value for the best match, which was only marginally higher than that of the second best. But even if another stack had yielded the best match, it definitely would have been a neighboring stack and therefore a neighboring respiratory state. Thus, the prediction of the target position would still be accurate and result in a significant reduction of the safety margin. Especially with regards to tests with real X-ray images, this fact will be very important, as these images will generally be noisier and of lower quality than the digitally reconstructed images.

7.2 Résumé

In this chapter, the determination of the respiratory state by matching two mutually orthogonal X-ray images to the corresponding computed 4D patient model was described. By calculated volumetric deformation models of five computed tomography patient data sets and corresponding digitally reconstructed radiographs, the 2D-4D registration procedure was evaluated. The DRRs were generated from one particular synthetic scan of the deformation model and were afterwards matched to every single scan of the model. Roth et al.'s [Roth 04] intensity-based rigid 2D-3D registration algorithm forms the basis of the procedure. The obtained registration results were very satisfying. Not only that in each case the scan the DRRs originated from yielded the best match, but also that the neighboring scans yielded the next best registrations results, as visualized in Figure 7.4.

8 Conclusion

This thesis proposes a new concept to compensate breathing motion in extracranial radiosurgery without using fiducial markers.

A computed volumetric deformation model forms the basis of this method, enabling a prediction of the position of the tumor at a certain time. This model consists of a number of synthetic scans, each representing one particular respiratory state. By matching periodically taken X-ray images to this model, the breathing phase, and therefore the position of the target can be determined. As this registration cannot be performed in real-time, infrared emitters are attached to the patient's chest and abdomen to report information on the current state of respiration. The sensor readings are correlated to the target locations obtained from the comparisons between the particular X-ray images and the model. Thus, a complete correlation model between external and internal motion is acquired without using any implanted fiducials. This enables the position of the tumor to be accurately determined at any given time. Furthermore, the patient and the medical staff are spared the encumbering operation of implanting the fiducials. To actually treat the moving tumor, the therapeutic beam has to follow the target, for example by using the Cyberknife® Radiosurgical System.

The main focus of this thesis was the process of creating the volumetric deformation model, needed for inferring the respiratory state. This 4D patient model is computed by deforming a volume scan taken during exhaled breath-hold with respect to landmark correspondences to a corresponding scan taken during inhaled breath-hold. Therefore, a novel method for fully automatic detection of corresponding anatomical landmarks in these two volumes was proposed.

Using this method, corresponding landmarks were automatically detected in five computed tomography and one magnetic resonance imaging data sets of the lung and the liver. These control points were used to model the occurring motion through a thin-plate spline based deformation of the exhalation scan. For evaluation, particular organs and structures of the image data were segmented to compute the surface distances between synthetic and real states of intermediate as well as reference scans, yielding mean deviations smaller than 2 mm. Visual inspections demonstrated the high accuracy of the performed elastic registrations. Furthermore, by using digitally

reconstructed radiographs, the feasibility of determining the respiratory state by comparison of an X-ray image to the volumetric deformation model was successfully demonstrated.

Moreover, a new technique for labeling computed tomography images with respiratory states was described, which was used to evaluate the model. A needle is attached to the patient's chest or abdomen and moves along with respiratory motion. The needle is aligned with the direction of the gantry, and breathing motion makes the needle move up and down. Thus, the information about the position of the needle is encoded in each computed tomography image. This enables every single slice to be assigned a specific respiratory state.

This thesis successfully demonstrated the feasibility of *fiducial-less* compensation of respiratory motion in extracranial radiosurgery. As a consequence, safety margins can be significantly reduced, allowing the tumor to be treated with higher doses.

Bibliography

[Baier 05a] K. Baier & J. Meyer. *Fast Image Acquisition and Processing on a TV Camera-Based Portal Imaging System*. Zeitschrift für Medizinische Physik, vol. 15, pages 122–125, 2005.

[Baier 05b] K. Baier, J. Meyer, A. Richter & J. Wilbert. *Real Time Tracking of Moving Structures by Means of Megavoltage Imaging*. In 14th International Conference of Medical Physics, Nuremberg, Germany, September 2005.

[Berlinger 04a] K. Berlinger, M. Roth, M. Dötter, O. Sauer, L. Vences, J. Fisseler & A. Schweikard. *Determination of the Tumor Position by an Intensity-Based 4D Registration Procedure*. In 3. Jahrestagung der Deutschen Gesellschaft für Computer- und Roboterassistierte Chirurgie (CURAC 2004), October 2004.

[Berlinger 04b] K. Berlinger, M. Roth, J. Fisseler, O. Sauer, A. Schweikard & L. Vences. *Volumetric Deformation Model for Motion Compensation in Radiotherapy*. In Medical Image Computing and Computer-Assisted Intervention – MICCAI 2004, Saint Malo, France, ISBN: 3-540-22977-9, pages 925 – 932, 2004.

[Berlinger 05a] K. Berlinger, M. Roth, O. Sauer, L. Vences & A. Schweikard. *Motion Compensation in Radiotherapy Using Advanced Volumetric Deformation Models*. In 4. Jahrestagung der Deutschen Gesellschaft für Computer- und Roboterassistierte Chirurgie (CURAC 2005), September 2005.

[Berlinger 05b] K. Berlinger, O. A. Sauer, L. Vences, M. Roth, M. Dötter & A. Schweikard. *Computed 4D Patient Models for Motion Compensation in Radiotherapy*. Medical Physics, vol. 32, page 1922, June 2005.

[Blackall 01] J.M. Blackall, A.P. King, G.P. Penney, A. Adam & D.J. Hawkes. *A Statistical Model of Respiratory Motion and Deformation of the Liver*. In Medi-

cal Image Computing and Computer-Assisted Intervention – MICCAI 2001, Utrecht, The Netherlands, ISSN: 0302-9743, page 1338, 2001.

[Blackall 02] J. M. Blackall. *Respiratory Motion in Image-Guided Interventions of the Liver*. Dissertation, King's and St. Thomas' School of Medicine King's College London, 2002.

[Bookstein 89] F. L. Bookstein. *Principal warps: Thin-Plate Splines and the Decomposition of Deformations*. IEEE Transactions on Pattern Analysis an Machine Intelligence, vol. 11, pages 567–85, 1989.

[Bookstein 91] F.L. Bookstein. *Morphometric Tools for Landmark Data*. Cambridge University Press, Cambridge, UK, 1991.

[Brock 02] K. K. Brock, S. J. Hollister, L. A. Dawson & J. M. Balter. *Creating a Four-Dimensional Model of the Liver Using Finite Element Analysis*. Medical Physics, vol. 29, pages 1403 – 1405, July 2002.

[Cleary 02] K. R. Cleary, F. Banovac M.D., E. Levy M.D. & D. Tanaka. *Development of a Liver Respiratory Motion Simulator to Investigate Magnetic Tracking for Abdominal Interventions*. In SPIE Medical Imaging 2002: Visualization, Image-Guided Procedures, and Display, volume 4681, pages 25 – 29, May 2002.

[Cootes 95] T.F. Cootes, C.J. Taylor, D.H. Cooper & J. Graham. *Active Shape Models – Their Training and Application*. Computer Vision and Image Understanding, vol. 61, pages 38–59, January 1995.

[Coselmon 04] M. M. Coselmon, J. M. Balter, D. L. McShan & M. L. Kessler. *Mutual Information Based CT Registration of the Lung at Exhale an Inhale Breathing States Using Thin-Plate Splines*. Medical Physics, vol. 31, pages 2942–2948, November 2004.

[Duchon 76] J. Duchon. *Interpolation des fonctions de deux variables suivant le principe de la flexion des plaques minces*. RAIRO Analyse Numérique, vol. 10, pages 5–12, 1976.

[Frangi 01] A. F. Frangi, D. Rueckert, J. A. Schnabel & W. J. Niessen. *Automatic 3D ASM Construction via Atlas-Based Landmarking and Volumetric Elastic Registration*. In Information Processing in Medical Imaging, volume 2082, pages 78–91, 2001.

[Goitein 04] M. Goitein. *Organ and Tumor Motion: An Overview*. Seminars in Radiation Oncology, vol. 14, pages 2–9, 2004.

[Hilbig 03] M. Hilbig. *Inverse Bestrahlungsplanung für intensitätsmodulierte Strahlenfelder mit Linearer Programmierung als Optimierungsmethode*. Dissertation, Fakultät für Informatik, Technische Universität München, 2003.

[Ibáñez 03] L. Ibáñez, W. Schroeder, L. Ng & J. Cates. *The ITK Software Guide*. http://www.itk.org, August 2003.

[Johnson 98] L. S. Johnson, S. W. Hadley & C. A. Pelizzari. *A Video-Based Technique to Gate Radiotherapy Treatments for Respiration*. International Journal of Radiation Oncology Biology Physics, vol. 42(Suppl. 1), page 139, 1998.

[Kubo 96] H. D. Kubo & B. C. Hill. *Respiration Gated Radiotherapy Treatment: a Technical Study*. Phys. Med. Biol., vol. 41, pages 83 – 91, 1996.

[Low 03] D. A. Low, M. Nystrom, E. Kalinin, P. Parikh, J. F. Dempsey, J. D. Bradley, S. Mutic, S. H. Wahab, T. Islam, G. Christensen, D. G. Politte & Bruce R. Whiting. *A Method for the Reconstruction of Four-Dimensional Synchronized CT Scans Acquired During Free Breathing*. Medical Physics, vol. 30, pages 1254 – 1263, June 2003.

[Maintz 98] J.B.A. Maintz & M. A. Viergever. *A Survey of Medical Image Registration*. Medical Image Analysis, vol. 2, pages 1–37, 1998.

[Matsopoulos 04] G. K. Matsopoulos, P. A. Asvestas, K. K. Delibasis, V. Kouloulias, N. Uzunoglu, P. Karaiskos & P. Sandilos. *Registration of Electronic Portal Images for Patient Set-Up Verification*. Physics in Medicine and Biology, vol. 49, pages 3279–3289, 2004.

[Meyer 03] C. Meyer, H. Park, J.M. Balter & P.H. Bland. *Method for Quantifying Volumetric Lesion Change in Interval Liver CT Examinations*. IEEE Transactions on Medical Imaging, vol. 22, pages 776–781, June 2003.

[Meyer 05] J. Meyer, K. Baier, A. Richter, J. Wilbert & M. Flentje. *Analysis of Different Agorithms for Tracking Moving Organs by Means of Megavoltage Imaging*. In 8th Biennial ESTRO Meeting on Physics and Radiation Technology for Clinical Radiotherapy, Lisboa, Portugal, September 2005.

[Onishi 03] H. Onishi, K. Kuriyama, T. Komiyama, S. Tanaka, J. Ueki, N. Sano, T. Araki, S. Ikenaga, Y. Tateda & Y. Aikawa. *CT Evaluation of Patient Deep Inspi-*

ration Self-Breath-Holding: How Precisely Can Patients Reproduce the Tumor Position in the Absence of Respiratory Monitoring Devices? Medical Physics, vol. 30, pages 1183 – 1187, June 2003.

[O'Rourke 94] J. O'Rourke. *Computational Geometry in C.* Cambridge University Press, Cambridge, UK, 1994.

[Pan 04] T. Pan, T.-Y. Lee, E. Rietzel & G. T. Y. Chen. *4D-CT Imaging of a Volume Influenced by Respiratory Motion on Multi-Slice CT.* Medical Physics, vol. 31, No. 2, pages 333 – 340, February 2004.

[Platzer 91] W. Platzer. *Taschenatlas der Anatomie Band 1: Bewegungsapparat*. Georg Thieme Verlag, Stuttgart, Germany, 1991.

[Pluim 03] J.P.W. Pluim, J.B.A. Maintz & M.A. Viergever. *Mutual-Information-Based Registration of Medical Images: A Survey*. IEEE Transactions on Medical Imaging, vol. 22, pages 986–1004, August 2003.

[Press 92] W.H. Press, S.A. Teukolsky, W.T. Vetterling & B.P. Flannery. *Numerical Recipes in C.* Cambridge University Press, Cambridge, UK, 1992.

[Richter 98] J. Richter & M. Flentje. *Strahlenphysik für die die Radioonkologie*. Georg Thieme Verlag, Stuttgart, Germany, 1998.

[Riesner 03] Stefan Riesner. *Korrelations- und Prädiktionsverfahren zur Lageverfolgung in der perkutanen Radioonkologie*. Dissertation, Fakultät für Informatik, Technische Universität München, 2003.

[Rohlfing 01] T. Rohlfing, C. R. Maurer Jr., W. G. O'Dell & J. Zhong. *Modeling of Liver Motion an Deformation During the Respiratory Cycle Using Intensity-Based Free-Form Registration of Gated MR Images.* In SPIE Medical Imaging 2001: Visualization, Image-Guided Procedures, and Display, volume 4319, pages 337–148, February 2001.

[Rohr 96] K. Rohr, H. S. Stiehl, R. Sprengel, W. Beil, T. M. Buzug, J. Weese & M. H. Kuhn. *Point-Based Elastic Registration of Medical Image Daata Using Approximating Thin-Plate Splines.* In Visualization of Biomedical Computing, pages 297–306, September 1996.

[Rosenzweig 00] K. E. Rosenzweig, J. Hanley, D. Mah, G. Mageras, M. Hunt, S. Toner, C. Burman, C. C. Ling, B. Mychalczak, Z. Fuks & S. A. Leibel. *The Deep Inspiration Breath-Hold Technique in the Treatment of Inoperable Non-Small-*

Cell Lung Cancer. International Journal of Radiation Oncology Biology Physics, vol. 48, pages 81 – 87, August 2000.

[Roth 04] M. Roth, M. Dötter, R. Burgkart & A. Schweikard. *Fast Intensity-Based Fluoroscopy-To-CT Registration Using Pattern Search Optimization*. In 18th Int. Congress Computer Assisted Radiology and Surgery (CARS 2004), 2004.

[Rueckert 98] D. Rueckert, C. Hayes, C. Studholme, P. Summers, M. Leach & D. J. Hawkes. *Non-rigid Registration of Breast MR Images Using Mutual Information*. In Medical Image Computing and Computer-Assisted Intervention – MICCAI 1998, Cambridge, USA, ISSN: 0302-9743, page 1144, 1998.

[Sauer 98] R. Sauer. *Strahlentherapie und Onkologie für MTA-R*. Urban & Schwarzenberg, München, Germany, 1998.

[Sauer 04] O. Sauer, K. Berlinger, M. Roth, L. Vences & A. Schweikard. *Production of Test Data for 4D Patient Models*. In 3. Jahrestagung der Deutschen Gesellschaft für Computer- und Roboterassistierte Chirurgie (CURAC 2004), Munich, Germany, 2004.

[Schweikard 00] A. Schweikard, G. Glosser, M. Bodduluri, M. Murphy & J. R. Adler. *Robotic Motion Compensation for Respiratory Motion during Radiosurgery*. Computer Aided Surgery, 2000.

[Schweikard 02] A. Schweikard, H. Shiomi, M. Dötter, M. Roth, K. Berlinger & J. Adler. *Fiducial-Less Compensation of Breathing Motion in Lung Cancer Radiosurgery*. Technical Report A-02-23, Informatik, Universität Lübeck, 23538 Lübeck, Germany, 2002.

[Schweikard 04a] A. Schweikard, H. Shiomi & J. Adler. *Respiration Tracking in Radiosurgery*. American Association of Physicists in Medicine, vol. 31, pages 2738 – 2741, October 2004.

[Schweikard 04b] A. Schweikard, H. Shiomi, J. Fisseler, M. Dötter, K. Berlinger, H. B. Gehl & J. Adler. *Fiducial-Less Respiration Tracking in Radiosurgery*. In Medical Image Computing and Computer-Assisted Intervention – MICCAI 2004, Saint Malo, France, ISBN: 3-540-22977-9, pages 992 – 999, 2004.

[Shannon 48] C. E. Shannon. *A Mathematical Theory of Communication*. The Bell System Technical Journal, vol. 27, pages 379–423 and 623–656, July and Oct 1948.

[Shirato 04] H. Shirato, Y. Seppenwolde, K. Kitamura, R. Onimura & S. Shimizu. *Intrafractional Tumor Motion: Lung and Liver*. Seminars in Radiation Oncology, vol. 14, pages 10–18, 2004.

[Sontag 98] M.R. Sontag, T.E. Merchant, B. Burnham, A.B. Shaw & L.E. Kun. *Clinical Experience with a System for Pediatric Respiratory Gated Radiotherapy*. International Journal of Radiation Oncology Biology Physics, vol. 42(Suppl. 1), page 140, 1998.

[Suramo 84] I. Suramo, M. Paivansalo & V. Myllyla. *Cranio-Caudal Movements of the Liver, Pancreas and Kidneys in Respiration*. Acta Radiologica Diagnosis, vol. 25, pages 129–131, 1984.

[Tang 04] J. Tang, S. Dieterich & K. R. Cleary. *Respiratory Motion Tracking of Skin and Liver in Swine for Cyberknife Motion Compensation*. In SPIE Medical Imaging 2004: Visualization, Image-Guided Procedures, and Display, volume 5367, pages 729 – 734, May 2004.

[Thirion 98] J.P. Thirion. *Image Matching as a Diffusion Process: An Analogy with Maxwell's Demons*. Medical Image Analysis, vol. 2, pages 243–260, 1998.

[Wang 05] H. Wang, L. Dong, M.F. Lii, A.L. Lee, R. De Crevoisier, R. Mohan, J.D. Cox, D.A. Kuban & R. Cheung. *Implementation and Validation of a Three-Dimensional Deformable Registration Algorithm for Targeted Prostate Cancer Radiotherapy*. International Journal of Radiation Oncology Biology Physics, vol. 61, pages 725–735, 2005.

[Wegener 96] O.H. Wegener. *Grundkurs Computertomographie*. Blackwell Wissenschaftsverlag, Berlin, Germany, 1996.

[Wein 03] W. Wein. *Intensity Based Rigid 2D-3D Registration Algorithms for Radiation Therapy*. Diplomarbeit, Fakultät für Informatik, Technische Universität München, 2003.

[Weisstein 99] E. W. Weisstein. *CRC Concise Encyclopedia of Mathematics*. Chapman & Hall/CRC, Boca Raton, US, 1999.

[Wong 99] J. W. Wong, M. B. Sharpe, D. A. Jaffray, V. R. Kini, J. M. Robertson, J. S. Stromberg & A. A. Martinez. *The Use of Active Breathing Control (ABC) to reduce Margin for Breathing Motion*. International Journal of Radiation Oncology Biology Physics, vol. 44, pages 911 – 919, July 1999.

[Wulf 05] J. Wulf. *Präzision und Technik der stereotaktischen Strahlentherapie im Bereich des Körperstammes*. 10 Jahre Stereotaktische Strahlentherapie und Radiochirurgie am Klinikum rechts der Isar der TU München, 2005.